

043  
NUR  
6543  
✓

S T U D I E S   I N   E Q U A T O R I A L   A E R O N O M Y

"MORPHOLOGY OF THE ELECTROJET"

Thesis

Presented by

P. MURALIKRISHNA

to the

GUJARAT UNIVERSITY, AHMEDABAD

for the degree of

DOCTOR OF PHILOSOPHY

March 1975

Physical Research Laboratory  
Ahmedabad 380 009  
India

043



B6543

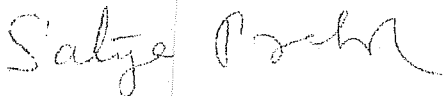
C E R T I F I C A T E

I hereby declare that the work presented in this thesis is original and has not formed the basis for the award of any degree or diploma by any University or Institution.



P. MURALIKRISHNA  
(Author)

Certified,



SATYA PRAKASH  
(Professor-in-charge)

March 7, 1975.




## STATEMENT

This thesis is based on the results of experiments conducted at an equatorial station Thumba, India, using a Back-scatter-radar, operating at 54.95 MHz. and Rocket-borne studies with Langmuir probe and magnetometer. The back-scatter-radar at Thumba was made operational in the year 1970 by Satya Prakash, Jain, C.L. and Co-workers. The author has been closely associated with the design and development of some of the radar units including the analog and digital data processing units. Working under the guidance of Prof. Satya Prakash at the Physical Research Laboratory, the author was responsible for analysing the data and interpreting the experimental results.

The main objectives of the present studies have been to understand the nature of distribution of currents in the equatorial ionosphere, to investigate the space and time variation of the electric fields responsible for these currents, and to trace the relationship between the equatorial electrojet and the world-wide Sq current system.

This thesis has been divided into seven chapters. The first two chapters deal with the history of the subject, the basic theory involved, the existing problems in the field and the experimental set-up used for the observations

and data recording. The experimental results are presented in the next four chapters. The concluding chapter deals with the important conclusions that have come out of the present studies.



P. MURALIKRISHNA  
(Author)



Prof. Satya Prakash,  
Physical Research Laboratory,  
Navrangpura,  
Ahmedabad - 380 009,  
INDIA.

March 7, 1975.

### ACKNOWLEDGEMENT

The author is indebted deeply to Prof. Satya Prakash for his guidance, supervision and encouragement he gave throughout the period of the work. Sincere thanks are due to Prof. Subbaraya for his valuable advice during the course of the present studies and to Messrs. T.R. Rao, H.S.S. Sinha and Y.B. Acharya for going through the manuscript of the thesis and suggesting many improvements.

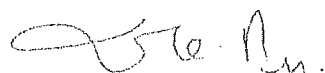
The author expresses his sincere gratitude to Mr. C.L. Jain, Physics and Applied Mathematics Division, SSTC, Trivandrum and his colleagues Messrs. K.V. Janardhanan, P.C. Joseph, K.S.V. Shenoy, C.D. Prasad, K.P. Kamath, D. Ramakrishna Rao and George Thomas, who, under the guidance of Prof. Satya Prakash, developed the facilities for back-scatter studies at Thumba, Trivandrum, India. Sincere thanks are also due to Dr. C.A. Reddy, Head, Physics and Applied Mathematics Division, SSTC and Dr. S. Ramnath, Head, Back-Scatter Project, SSTC, for the keen interest they have shown in the present studies and the facilities provided by them in taking the radar observations. The author wishes to thank Dr. S.P. Gupta and Mr. K.K. Goswami for developing and testing the payload circuitry, and Prof. T.S.G. Sastry for providing the current density profiles used during the present studies.

Acknowledgements are also due to NASA, USA, for supplying the Nike Apache rockets and to Mr. H.G.S.Murthy, Ex-Director, Thumba Equatorial Rocket Launching Station, and his colleagues for their enthusiastic cooperation in making the rocket launchings successful.

The author wishes to acknowledge with gratitude, his indebtedness to Dr. B.B. Balsley and Dr. R.A. Greenwald, NOAA, Boulder, Colorado (USA) for their efforts in setting up the dipole antenna array used during some of the observations, reported in this thesis.

The author is extremely thankful to Prof. Bhargava, Director, Indian Institute of Geomagnetism, Colaba, for providing the magnetograms used in the present studies.

It is a pleasure to thank Messrs, S. Muralidharan Nair, R.I. Patel and K.S. Patel for the help rendered by them in the reduction and analysis of the data, and Mr. G.A. Panchal for his excellent draftsmanship. Thanks are also due to Dr. P.D. Angreji and his colleagues in the photographic section for their kind cooperation during the course of this work. Finally, the author wishes to thank Messrs. M. Narayanan Kutty and G. Vilasa Chandran for the neat typing of this thesis.



(P. MURALIKRISHNA)

## TABLE OF CONTENTS

### CHAPTER I

#### Introduction

		<u>Page No.</u>
1.1	Equatorial electrojet	
1.1.1	History of the subject	1
1.1.2	General nature of the current system	4
1.1.3	Methods of electrojet studies	9
1.2	Study of electrojet by VHF scatter Radar	
1.2.1	History of radar studies	12
1.2.2	Coherent and Incoherent scatter	14
1.2.3	General theory of coherent scattering	17
	(a) Distribution of signal amplitudes and phase	22
	(b) Signal frequency spectrum	23
1.3	Irregularities in the electrojet	
1.3.1	Nature and generation of irregularities	27
	(1) Streaming instabilities and the type I irregularities	28
	(2) Cross field instability and the type II irregularities	29
1.3.2	Radar studies of the electrojet irregularities	34
1.4	Scope of the present studies	40

## CHAPTER II

### Instrumentation and data reduction

2.1	Instrumentation	
2.1.1	System in general	43
2.1.2	Programmer unit	44
2.1.3	Transmitter	46
2.1.4	Receiving system	47
	(a) Receiver for amplitude studies (Receiver I)	47
	(b) Receiver for spectral studies (Receiver II)	49
2.1.5	Spectrum analyser unit	50
2.1.6	Recording units	
	(a) Amplitude recording system	52
	(b) Spectral display and recording	53
2.1.7	Antenna systems	53
	(a) Yagi array	53
	(b) Dipole array	54
2.1.8	Calibration of the amplitude receiver	55
2.2	In-situ measurements of $J$ and $n_e$	
2.2.1	Measurement of $J$	56
2.2.2	Measurement of $n_e$	57
2.3	Data reduction	
2.3.1	Correction of spectra for filter characteristics	58
2.3.2	Doppler spectrum and the velocity spectrum	59
2.4	Digital data processing	60

## CHAPTER III

### Electrostatic field and electrical conductivities within the Equatorial electrojet

3.1	Introduction	
3.1.1	Importance of the electric field studies	62
3.1.2	Estimation of electric field	64
3.2	Observations and analysis	
3.2.1	In-situ measurements of current density	65
3.2.2	Rocket measurements of electron density	66
3.2.3	Computation of conductivity parameters	66
3.2.4	Estimation of electric field profiles	68
3.3	Results	
3.3.1	Flight details	69
3.3.2	Summary of results	70
3.4	Discussion of results	
3.4.1	Region of streaming irregularities	72
3.4.2	Nature of cawling conductivity	73
3.4.3	Electrostatic fields within the electrojet	74
3.5	Conclusions	78

## CHAPTER IV

### Electric fields in the E-region during morning and evening hours

4.1	Introduction	
4.1.1	Objectives of present study	80
4.1.2	Electric fields from drift velocities	81
4.1.3	Height variation of the electric field	82
4.2	Observations and results	
4.2.1	Morning hours	83
4.2.2	Evening hours	86
4.3	Discussion of results	
4.3.1	Morning and evening electric fields	88
4.3.2	Vertical drift in the region of electric fields	90

## CHAPTER V

### Ionisation Irregularities in the counter electrojet

5.1	Introduction	
5.1.1	Counter electrojet	94
5.1.2	Present studies	96
5.2	Observations and results	
5.2.1	Radar echoes during counter electrojet periods	97
5.2.2	Occurrence periods of counter electrojet	101
5.2.3	Summary of results	102



5.3	Discussion of results	
5.3.1	Existence of currents above the electrojet region	103
5.3.2	Generation mechanisms of irregularities in the counter electrojet	104

## CHAPTER VI

### Morphology of electrojet currents over Indian zone

6.1	Radar echo and the geomagnetic field variations	108
6.2	Reduction of magnetograms and analysis of data	109
6.3	Results and discussions	
6.3.1	Results	113
6.3.2	S as a measure of $\Delta H_{ET}$	115
6.3.3	Currents above the electrojet region	117
6.3.4	Electrostatic fields in the E and F regions	121
6.4	Conclusion	121

## CHAPTER VII

### Summary and conclusions

7.1	Vertical gradient in the primary electric field	127
7.2	Fields confined to higher altitudes during the reversal period	128
7.3	Higher fields during pre-reversal periods	129
7.4	Currents above the electrojet region	129
7.5	Uncorrelated reversal of currents in and above the electrojet region	130

References

## I N T R O D U C T I O N

### 1.1 Equatorial electrojet

#### 1.1.1 History of the subject

Daily variation in the geomagnetic field was first observed in the year 1722 by Graham (1724). From the year 1834 onward, Gauss and his successors studied the general nature of these variations on a global scale. The results of these studies led Stewart (1882) to infer that these variations have their origin in electric currents in the upper atmosphere. The solar component of these variations in the geomagnetic field on a quiet day were termed as Sq variations. Schuster (1889) applied the method of spherical harmonic analysis to Sq and confirmed Stewarts' inference that Sq arises due to currents mainly above the earth's surface but found a smaller part of internal origin. This he ascribed to electric currents induced in the earth by the primary external currents. The existence of such an electrically conductive atmospheric layer was later confirmed by the exploration of the ionosphere during the second decade of this century. Bottom side radio sounding of the ionosphere was then developed by Breit and Tuve (1925, 1926) and Appleton and Barnett (1925) for the study of ionospheric structure up to the level ( $F_2$  peak) of maximum electron density. This, then, was followed by top side sounding using satellites such as Alouette and Ariel, which extended

exploration above the  $F_2$  peak. The height distribution of electron density suggested that the Sq currents flow mainly in the E layer at a height of the order of 100-125 kms.

In the year 1908 Schuster developed a quantitative theory to explain the observed geomagnetic field variations. In general, the Stewart-Schuster theory is the application of the dynamo principle to conditions existing in the ionosphere. The conducting region in the ionosphere is treated as a thin spherical conducting layer in the earth's magnetic field. The force exerted on the charged particles, because of the motions of the neutral atmosphere, is at right angles to both the magnetic field and the neutral particle velocity. The circulation of the neutral atmosphere is primarily horizontal at these heights. Under these conditions, the vertical component of the geomagnetic field produces appreciable drifts of the charged particles.

In the year 1922, a new feature of the variations of the earth's magnetic field was brought to light at Huancayo in Peru; near the dip equator. Whereas the daily ranges of declination  $D$  and the vertical component  $Z$  of the geomagnetic field were comparable to those of the stations in similar geographic latitudes, the diurnal range in the horizontal component  $H$  was abnormally large, being often more than double the value expected. Egadel (1947, 1948) reported that the diurnal range of  $H$  at six other stations near the dip equator also showed such enhancements. He suggested the

existence of a varying electric current of about 300 kms. in width flowing in a very narrow zone near the dip equator. The enhancement of the diurnal range of H was attributed to these overhead currents.

Early calculations of the ionospheric conductivity yielded values that fell far short of the ones needed to account for these enhanced magnetic field variations. Later investigations initiated by Taylor in 1936 and Pekeris in 1937 showed that atmospheric tidal oscillations could be expected to be greater at ionospheric heights than those observed at ground levels. With the inclusion of this effect in the dynamo theory, the theoretical conductivity profile was brought into a more reasonable agreement with the observations. This enhancement of conductivity in the region near the magnetic equator was demonstrated by a series of theoretical investigations by Cowling (1932), Martyn (1947) and Cowling and Borger (1948). Cowling showed that the horizontal conductivity would be enhanced if it was postulated that the vertical Hall currents were inhibited. Martyn suggested that this phenomenon might account for the additional increase in conductivity needed to bring the general theory into complete accord with observations. Cowling and Borger showed that although Martyn's suggestion could not be upheld in general, it was certainly valid in the region of magnetic equator. Analysis by Martin of Egedals' and other similar data showed that they were

consistent with the idea of a belt of high current density in the equatorial E-region. This high concentration of electric currents flowing from west to east in a narrow belt flanking the dip equator, on the sunward hemisphere was named, the equatorial electrojet by Chapman (1951).

#### 1.1.2 General nature of the current system

When the dynamo theory was first formulated mathematically little was known about the conductivity or the movements of the earth's atmosphere. The dynamo theory was successively revised as more data on ionospheric electron densities became available from ionosonde records. The revisions take the anisotropic nature of the ionospheric conductivity into account and show that the observed upper atmospheric wind velocities, electron densities and magnetic variations are at least approximately consistent with each other in terms of the dynamo theory. The tidal motion of the earth's atmosphere, in conjunction with the geomagnetic field generates electric fields (the dynamo fields) in the ionosphere (Hirano 1952, Baker and Martin 1953, Fejer, 1953). These horizontal currents generally flow at altitudes of the order of 90 kms. to perhaps 140 kms. At lower heights the conductivity of the ionosphere is low because of the high collision frequency. At greater heights, the horizontal conductivity is also low in this case because of the earth's magnetic field. When the collision frequencies of both electrons and ions are small compared to the respective

gyrofrequencies, crossed electric and magnetic fields cause the ions and electrons to drift together with the velocity  $\vec{E} \times \vec{B} / B^2$  and thus there is no net current. In the conductive region, the ratio of the collision frequency to the gyrofrequency is generally less than 1 for the electrons, but greater than 1 for the ions. The cause of the equatorial electrojet, lies in a special equatorial feature of the electrical conductivity of the upper atmosphere. Here, the applied horizontal electric field causes a vertical polarisation field to build up which enhances the horizontal flow considerably. The electrojet flows in a narrow height range of about 10 to 15 kms. which is centered at an altitude of about 105 km. and it appears only in areas within two to three degrees of latitude of the magnetic dip equator.

### Electrical conductivities

The ionosphere may be considered as an infinite lightly ionised gas in which there are  $n_r$  charged particles of the  $r^{\text{th}}$  type per  $\text{cm}^3$ . Let a particle of  $r^{\text{th}}$  type has a charge  $e_r$ , mass  $m_r$ , collision frequency  $\nu_r$  and gyrofrequency  $\omega_r$  given by:  $(e_r B) / m_r$  where  $B$  is the intensity of the ambient magnetic field.

The longitudinal conductivity  $\sigma_0$  which governs the conduction of charged particles along the field lines in the presence of an electric field component in that direction is given by:

$$\sigma_0 = \sum_r \frac{n_r e_r^2}{m_r \nu_r} \quad \text{---(1.1)}$$

The motion of the charged particles at right angles to  $B$ , caused by an electric field component in that direction is defined by the Pedersen conductivity  $\sigma_1$

$$\sigma_1 = \sum_r \frac{n_r e_r^2 \nu_r}{m_r (\omega_r^2 + \nu_r^2)} \quad - (1.2)$$

The current flow in  $(\vec{E} \times \vec{B})$  direction is determined by the Hall conductivity.

$$\sigma_2 = - \sum_r \frac{n_r e_r^2 \omega_r}{m_r (\omega_r^2 + \nu_r^2)} \quad - (1.3)$$

The negative sign shows that the current is taken to be positive in  $-(\vec{E} \times \vec{B})$  direction. In this relation the sign of  $\omega_r$  is to be taken into consideration (Positive for positive ions and negative for electrons and negative ions).

A simplified form of these relations can be obtained for a neutral plasma, containing only electrons and singly ionised positive ions. The expressions for  $\sigma_0$ ,  $\sigma_1$  and  $\sigma_2$  can then be rewritten as:

$$\sigma_0 = n_e e^2 \left[ \frac{1}{m_e \nu_e} + \frac{1}{m_i \nu_i} \right] \quad - (1.4)$$

$$\sigma_1 = n_e e^2 \left[ \frac{\nu_e}{m_e (\omega_e^2 + \nu_e^2)} + \frac{\nu_i}{m_i (\omega_i^2 + \nu_i^2)} \right] \quad - (1.5)$$

$$\sigma_2 = n_e e^2 \left[ \frac{\omega_e}{m_e (\omega_e^2 + \nu_e^2)} - \frac{\omega_i}{m_i (\omega_i^2 + \nu_i^2)} \right] \quad - (1.6)$$

where -

$$\omega_e = \left| \frac{e B}{m_e} \right| \quad \text{and}$$

$$\omega_i = \left| \frac{e B}{m_i} \right|$$

The effective electrical conductivities and their variation with latitude at the electrojet region can be obtained following the procedure adopted by Baker and Martyn (1953). The ionosphere is considered to be a plane conducting sheet. Oxyz is a rectangular co-ordinate system, of which the x and y axes coincide with the geomagnetic south and east respectively. The z axis is upwards. I is the magnetic dip, at any given point in the electrojet region, and is taken to be positive in the Northern hemisphere and negative in the Southern hemisphere. Assuming that the vertical currents are inhibited in the electrojet region, one can get an expression for the polarisation field  $E_z$  generated by the primary dynamo electric field ( $E_y$ ) which is assumed to be in the y-direction;

$$E_z = \sigma_2 E_y \cos I / (\sigma_0 \sin^2 I + \sigma_1 \cos^2 I) \quad - (1.7)$$

For the equatorial region, where  $I = 0$ , this equation reduces to the form,

$$E_z = \frac{\sigma_2}{\sigma_1} \cdot E_y \quad - (1.8)$$

Substituting the value of  $E_z$  as given by equation 1.7 one can get the conductivity parameters.

$$\sigma_{xx} = \sigma_0 \sigma_1 / (\sigma_0 \sin^2 I + \sigma_1 \cos^2 I) \quad - (1.9)$$

$$\sigma_{xy} = \sigma_0 \sigma_2 / (\sigma_0 \sin^2 I + \sigma_1 \cos^2 I) \quad - (1.10)$$

$$\text{and } \sigma_{yy} = \frac{\sigma_0 \sigma_1 \sin^2 I + (\sigma_1^2 + \sigma_2^2) \cos^2 I}{\sigma_0 \sin^2 I + \sigma_1 \cos^2 I} \quad - (1.11)$$



where  $\sigma_{xx}$  is the conductivity in the x direction caused by an electric field component  $E_x$  in the x direction.  $\sigma_{xy}$  is the conductivity in the x direction caused by an electric field component  $E_y$  in the y direction.  $\sigma_{yy}$  is the total conductivity in the y direction, due to an electric field component  $E_y$  in the y direction. The variation of these conductivities with latitude is shown by the dependence of these parameters on  $I$ , the dip angle. At the magnetic equator, since  $I = 0$

$$\sigma_{xx} = \sigma_0 \quad \text{--- (1.12)}$$

$$\sigma_{xy} = 0 \quad \text{--- (1.13)}$$

$$\sigma_{yy} = \sigma_1 + \frac{\sigma_2^2}{\sigma_1} \quad \text{--- (1.14)}$$

$\sigma_{yy}$  is the effective conductivity which at the magnetic equator, is represented by  $\sigma_3$

$$\sigma_3 = \sigma_1 + \frac{\sigma_2^2}{\sigma_1}$$

— and is known as the Cowling conductivity.

Based on this theory put forward by Baker and Martin, Suguira and Cain put forward an electrojet model (Suguira and Cain 1966). The assumptions of inhibition of vertical currents and the absence of a component of the electric field in the north-south direction lead to a self inconsistency in this model. As shown later by Untiedt (1967) these assumptions lead to strongly divergent currents in the north-south direction that cannot exist in the ionosphere within a system like the equatorial electrojet that slowly varies with time. A modification of this model, taking into consideration the existence of meridional currents,

also was put forward by Untiedt (1967) which was later extended for the case of realistic world wide distribution of magnetic fields by Suguira and Poros (1969). The current densities computed from these models were seen to be much higher than the experimentally observed values by a factor as high as 7. Possibly this is due to the higher electric field values assumed in these models (Subbaraya et al 1972). Taking into consideration the effect of neutral winds Richmond (1973) put forward a numerical model of the equatorial electrojet. Though this model brought the predictions and observations closer, still the knowledge of the current system, seems to be far from complete.

### 1.1.3 Methods of electrojet studies

The techniques used for the study of the electrojet parameters can be broadly classified into two:

- (i) Ground based measurement techniques
- (ii) Rocket measurement techniques

Depending on whether the technique employed is for the measurement of parameters of the neutral atmosphere, or of the ionised medium, they can again be classified into two. A few of the important and widely used ground based measurement techniques are the following:

- (i) Ionosonde: R.F. signals with frequency swept from one value to another are transmitted and from an analysis of the ionogram traces produced by the reflected signals

informations are obtained of the electron density distribution up to a height of the F2 peak.

(ii) Magnetometers: By a spherical harmonic analysis of the observed variations in the geomagnetic field parameters at the ground level, the current system causing these variations are estimated. Ground based magnetometers thus enable the study of the average properties of the currents at the electrojet region. This method has been extended for in-situ measurements using rocket-borne magnetometers.

(iii) Spaced-receivers: This is one of the most widely employed methods to measure the drifts of electron density irregularities. The basic technique is to record the amplitude pattern of the reflected signal simultaneously at three closely or widely separated points on the ground (Mitra, 1949). These amplitude variations are associated with the movement of ionisation irregularities. The time delays between similar fades at the receivers are used for obtaining the speed and direction of drift of the irregularities.

(iv) Doppler shift technique: Motions of irregularities have been estimated from the doppler shifts in the radar echoes from them using very high frequencies. Irregularities in the equatorial and auroral E regions have been detected by this method; and later has been extended for the study of spread F irregularities.

(v) Meteor trail method: Long enduring meteor trails are photographed and informations regarding the vertical scale of the irregular winds in the height region of 80-110 kms. is obtained from these photographs. This technique is used for the study of motions in the neutral atmosphere.

Experiments conducted using rocket-borne payloads have been widely used for the study of the electrojet. Some of the important techniques used are listed below:

(vi) Rocket borne magnetometers: The special contribution of rocket measurements to the study of electrojet is the determination of its altitude and thickness. The variation in the total magnetic field as the rocket crosses the electrojet region is measured by a magnetometer and is converted into the electrojet current density profile. Proton precision magnetometers and rubidium vapour magnetometers are normally used for these measurements.

(vii) Rocket-borne Langmuir probes: Langmuir probes are flown in rockets mainly for the measurement of electron density and the structure of the electron density irregularities in the electrojet region. The variation in the probe currents are converted into varying voltages and telemetered to a ground station, where the probe current data is converted into electron density data.

(viii) Cloud releases: Chemicals are released at the ionospheric heights and the change in the structure of these clouds are photographed at different points on the ground. This method is mainly used for the study of the structure of the neutral wind system between about 80 and 180 kms.

## 1.2 Study of Electrojet by VHF scatter Radar

### 1.2.1 History of radar studies

The theory of scattering by a turbulent medium was first applied to scattering of radio waves in the troposphere as early as 1950 by Booker and Gordon (1950). Based on this theory a new kind of radio propagation at very high frequencies observable over long distances was reported by Bailey et al (1952). The initial experiments at a frequency of 49.8 MHz revealed the uninterrupted presence of observable signal over a test path of 1245 km. irrespective of season, time of day, or geomagnetic disturbance, though showing dependence in intensity on these factors and possibly on meteor activity as well. They suggested that the mechanism of propagation might be scattering caused by the ever present irregularities in the E-region and an approximate transmission equation was derived in terms of parameters describing inhomogeneities in the E-region. This marks the beginning of the use of coherent scatter (Section 1.2.2) technique for the investigation of ionospheric irregularities.

All charged particles are capable of scattering electromagnetic waves (J.J. Thomson, 1906) the scattering cross-section being inversely proportional to the square of the mass and proportional to the fourth power of the charge of the particle. It follows that the scattering cross-section for an electron is  $10^9$  times larger than that of an atomic oxygen ion. Though ionisation irregularities in the E-region were observed by this scatter technique, as early as 1952, the possibility of observing Thomson scattering by free electrons (incoherent scatter, Section 1.2.2) in the earth's ionosphere was abandoned as being impractical till 1958. In the year 1958, Gordon predicted that a powerful radar whose components were within the reach of the art, could be used to detect signal scattered by free electrons in the ionosphere and above. According to Gordon, such a radar would be capable of measuring electron density and electron temperature as a function of the height and time at all levels in the earth's ionosphere.

Stimulated by Gordon's proposal Bowles (1958) attempted to observe Thomson scattering from the ionosphere using a newly completed transmitter at Long Branch Hill that was intended for meteor studies. He demonstrated that echoes were obtained which resembled Thomson scattered signals in every respect, except that their bandwidth was considerably less than that expected on the basis of Doppler broadening introduced by the random motion of the

electrons (Bowles 1959, 1961) correctly surmised that the role played by the ions in the plasma was to narrow the bandwidth of the reflected signals. The net result is that the energy per unit bandwidth is far higher than estimated by Gordon, so that radar systems considerably smaller than the one proposed by him are capable of detecting the scattering from heights where the electron density is large. Later works of Bowles in this direction resulted in the construction at Jicamarca in Peru, near the geomagnetic equator, of a vertically directed radar system.

A series of radar propagation experiments were conducted during the International Geophysical Year (1957/58) at various stations close to the equator (Bowles and Cohen, 1957). An intense mode of VHF propagation associated with the experimental sporadic E was found to occur and was demonstrated to be closely identifiable in time variation and height with the equatorial electrojet (Gates, 1959).

The characteristic features of the irregularities in the electrojet region as studied by later experimenters using the VHF scatter technique are discussed in detail in section 1.3.2 of this chapter.

#### 1.2.2 Coherent and Incoherent scatter

The scattering of electromagnetic waves by free electrons is generally known as incoherent scattering, while that by ionisation irregularities is known as

coherent scattering. There is no sharp distinction between the two, and in a way the definition depends on the frequency of the electromagnetic waves that are scattered.

The scattered flux at a point away from the scattering volume, containing a large number of scattering centres, is determined by the distribution of scattering centres in the volume and the scattering cross-section of the particles. Let the scattering volume contain  $n$  scattering centres. The electric field of the incident electromagnetic wave is represented by

$$E = E_0 \exp [j \Phi(t)] \quad - (1.15)$$

The electric field at the receiver due to scattering from the  $i^{\text{th}}$  scattering centre can be represented as

$$e_i = E_i \exp [j \phi_i(t)] \quad - (1.16)$$

where the subscript  $i$  refers to the  $i^{\text{th}}$  scattering centre.

The total field  $E_r$  at the receiver can be obtained by

summing up all the  $e_i$  values for all the scattering centres.

$$E_r = \sum_{i=1}^n e_i = \sum E_i \exp [j \phi_i(t)] \quad - (1.17)$$

$E_r \cdot E_r^*$  is proportional to the flux at the receiver and is given by

$$\begin{aligned} E_r \cdot E_r^* &= \left\{ \sum E_i \exp [j \phi_i(t)] \right\} \left\{ \sum E_k \exp [-j \phi_k(t)] \right\} \\ &= \sum_i E_i^2 + \left\{ \sum_i \sum_{\substack{k \\ k \neq i}} E_i E_k \exp [j \overline{\phi_i(t) - \phi_k(t)}] \right\} \quad - (1.18) \end{aligned}$$



The first term represents the sum of the flux scattered by the individual scattering centres, if they are completely independent of each other. The magnitude of the second term depends on the distribution of scattering centres in the volume. For a completely random distribution, the second term is zero and the maximum theoretical value of the second term is  $\sum_i \sum_{k \neq i} E_i E_k$  the fields being getting added in phase all the time.

Thus the minimum value of  $E_r \cdot E_r^*$  is  $\sum_i E_i^2$  and the maximum value is  $\sum_i E_i^2 + \sum_i \sum_{k \neq i} E_i E_k$  which is nothing but  $(\sum_i E_i)^2$ . In the first case, the scattering is said to be perfectly incoherent and in the second case to be perfectly coherent. These two extreme cases are only theoretical. The received flux for incoherent scatter is directly proportional to the number of scattering centres, while in the case of coherent scatter it is directly proportional to the square of the number of scattering centres.

The significance of the phase term in the above relations, shows the role of the frequency of e.m. wave scattered, in governing the phenomenon. It can be shown that the scattering becomes coherent for a given e.m. wave, if the  $\lambda$  of the wave is far greater than the mean free path of the scattering centres and becomes incoherent if  $\lambda$  is of the order of mean free path or less than that.

In other words, a given scattering volume can be studied both by coherent and incoherent scatter techniques by properly selecting the frequency of the e.m. waves.

### 1.2.3 General theory of coherent scattering

Let  $\Phi_0$  be the electromagnetic flux incident on a single electron with equivalent isotropic scattering cross-section  $\sigma_0$ . The scattered flux at a distance R is given by

$$\Phi_r = \Phi_0 \sigma_0 / (4\pi R^2) \quad - (1.19)$$

The electric field associated with this flux is

$$E_r = \Phi_r^{1/2} (\mu_0 / \epsilon_0)^{1/4} \quad - (1.20)$$

where  $\mu_0$  is the magnetic permeability of free space and  $\epsilon_0$  is the permittivity of free space.

$\sigma_0 = 0.99 \times 10^{-28} \text{ m}^2$  for a free electron at an angle of  $180^\circ$  with the incident direction.

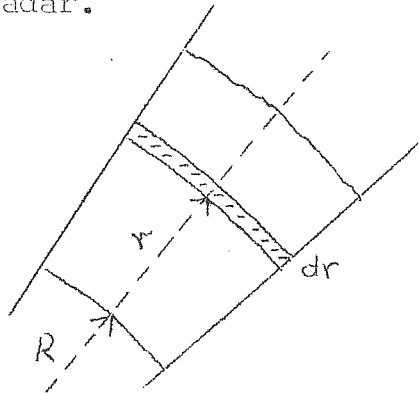
The varying electric field of the incident e.m. wave will contribute a phase factor to this; and equation (1.20) can be rewritten as

$$e_r = E_r \exp [j(\omega_0 t - 2R)] \quad - (1.21)$$

where  $R = 0$  corresponds to the transmitting and receiving points. (Monostatic Radar).  $\omega_0$  is the frequency of the incident e.m. wave,  $K = 2\pi/\lambda$  is the propagation constant,  $\lambda$  is the wavelength of the incident wave and  $E_r$  is the amplitude of the scattered wave at the receiver given by equation (1.20).

Equation (1.21) gives the field at the receiver due to scattering from a single electron. By summing up the scattered fields due to many such electrons in a scattering volume, this can be extended to a group of electrons.

Figure (1.1) shows the geometry of the scattering volume for a monostatic radar.

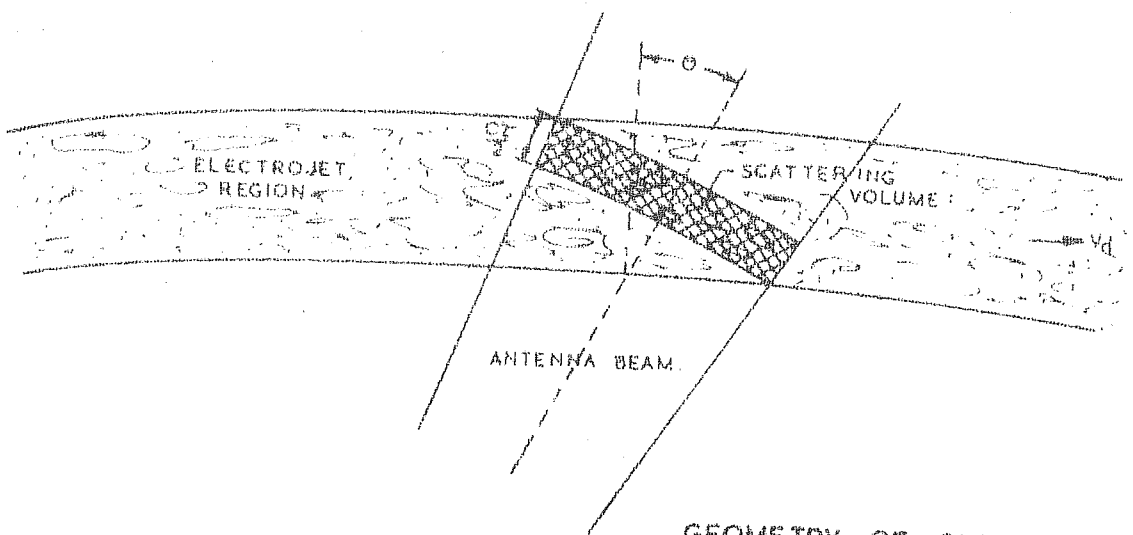


The incident wave front is at a distance  $R$  from the source of transmission (and reception). The scattered field at the receiver due to the  $i^{\text{th}}$  electron distant  $r_i$  from this wave front can be written as:

$$e_{ri} = E_r \exp \left[ j \left\{ \omega_0 t - 2k(R + r_i) \right\} \right] \quad - (1.22)$$

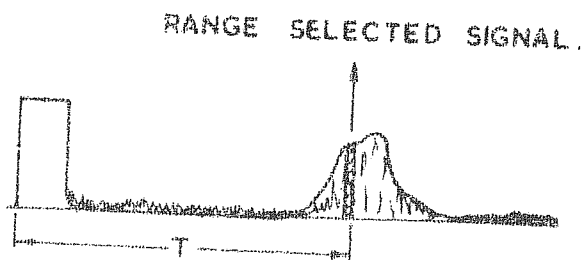
The total field at the receiver due to the  $N$  electrons in the scattering volume can be obtained by summing up the individual contributions

$$\begin{aligned} e_R &= \sum_{i=1}^N E_r \exp \left[ j \left\{ \omega_0 t - 2k(R + r_i) \right\} \right] \\ &= E_r \exp(j\omega_0 t) \sum_{i=1}^N \exp \left[ -j2k(R + r_i) \right] \quad - (1.23) \end{aligned}$$

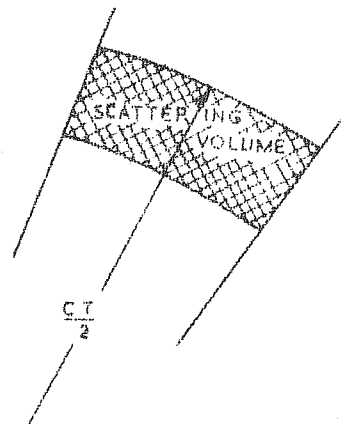


$\tau$  — PULSE WIDTH.  
 $\theta$  — ANGLE OF TRANSMISSION  
 $V_d$  — DRIFT VELOCITY OF ELECTRONS

GEOMETRY OF SCATTERING  
FOR A MONOSTATIC RADAR.



OSCILLOSCOPE DISPLAY.



HEIGHT SELECTION GATE AND THE  
CORRESPONDING SCATTERING VOLUME

FIG. 1.01: GEOMETRY OF SCATTERING VOLUME

The total flux at the receiver is given by

$$\begin{aligned}\phi_R &= (\epsilon_0/\mu_0)^{1/2} \mathcal{E}_R \mathcal{E}_R^* \\ &= \Phi_r \exp(j\omega_0 t) \exp(-j\omega_0 t) \cdot \sum_{i=1}^N \exp[-2jk(R+r_i)] \sum_{\ell=1}^N \exp[2jk(R+r_\ell)] \\ \text{where } \Phi_r &= (\epsilon_0/\mu_0)^{1/2} \cdot E_r^2 \\ &= \Phi_0 \sigma_0 / (4\pi R^2)\end{aligned} \quad \text{---(1.24)}$$

— as given by equation (1.19) is the peak flux at the receiver due to scattering by a single electron at a distance  $R$ , when a flux  $\Phi_0$  is incident on it.

$$\phi_R = \Phi_r \sum_i \sum_{\ell} \exp[-2jk(r_i - r_\ell)] \quad \text{---(1.25)}$$

Considering a slab of elemental thickness  $dr$  parallel to the incident wave front at a distance  $r$  from it (measured in the radial direction of wave propagation) all electrons in this slab can be assumed to have the same  $r$  value. Let  $N_r dr$  be the total number of electrons in this volume where

$$N_r = \int_A n_r dA \quad \text{---(1.26)}$$

where  $n_r$  is the average electron density in the slab, and  $A$  is the area of cross-section of the slab which can be assumed to be constant. The above summation can then be transformed into integration as

$$\phi_R = \Phi_r \int_0^{r_0} \int_0^{r_0} N_{r_1} N_{r_2} \exp[-2jk(r_1 - r_2)] dr_1 dr_2 \quad \text{---(1.27)}$$

where  $r_0$  is the maximum value of  $r_1$  which is determined by the dimension of the scattering volume in the direction of transmission. The above relation can be written in the volume integral form as

$$\phi_R = \Phi_r \int_V \int_V n_{r_1} n_{r_2} \exp[-2jk(r_1 - r_2)] dv_1 dv_2 \quad \text{---(1.28)}$$

where  $dv_1$  and  $dv_2$  refer to elementary volumes at distances  $r_1$  and  $r_2$  respectively from the incident wave front, in which the average electron densities are  $n_{r1}$  and  $n_{r2}$  respectively. Here one has to bring both time and space averages of this parameter. The average flux over a time interval  $T$  over which the electron density does not change drastically, is given by

$$\bar{\Phi}_R = \bar{\Phi}_r \iiint_V \left[ \frac{1}{T} \int_{t_0}^{t_0+T} n_{r1} n_{r2} dt \right] \exp[-2jk(r_1-r_2)] dv_1 dv_2 \quad (1.29)$$

Let  $n_r$  can be split into a constant part  $n_0$  invariant with time and space, over the time interval  $T$  considered and in the given space domain  $V$ ; and a time and space variant part  $\Delta n(r,t)$ . Then,

$$n_r = n_0 + \Delta n(r,t) \quad (1.30)$$

From this definition, it is implied that

$$\frac{1}{V} \int_V n_r dv = n_0 \quad \text{and} \quad (1.31a)$$

$$\frac{1}{T} \int_T n_r dt = n_0 \quad (1.31b)$$

$$\text{which in turn implies that } \overline{\Delta n(r,t)} = 0. \quad (1.32)$$

where the upper bar indicates the average over a given time interval.

Substituting the relation (1.30) in the equation (1.29) for the average flux, one gets

$$\bar{\Phi}_R = \bar{\Phi}_r \iiint_V \left[ \overline{\{n_0 + \Delta n(r_1)\} \{n_0 + \Delta n(r_2)\}} \right] \exp[-2jk(r_1-r_2)] dv_1 dv_2 \quad (1.33)$$

Since  $\exp[-2jk(r_1-r_2)]$  has an oscillating nature, over a sufficiently large scattering volume, the contribution due to  $\text{no}^2$  term vanishes (concept of the coherent scatter).

Also  $\overline{\Delta n(r_1)} = \overline{\Delta n(r_2)} = 0$  according to their definition. So one can write

$$\overline{\Phi_R} = \overline{\Phi_r} \int_V \overline{\Delta n(r_1) \Delta n(r_2) \exp[-2jk(r_1-r_2)]} dv_1 dv_2 \quad (1.34)$$

Using the vector notation and denoting the vector joining the points  $\vec{r}_1$  and  $\vec{r}_2$  as  $\vec{\Delta r}$  one can rewrite the above equation as

$$\overline{\Phi_R} = \overline{\Phi_r} \int_V \int_{\Delta \vec{r}} \Delta n(\vec{r}) \Delta n(\vec{r} + \vec{\Delta r}) \exp[-2j\vec{k} \cdot \vec{\Delta r}] d^3(\vec{\Delta r}) d^3(\vec{r}) \quad (1.35)$$

The normalised density auto correlation function  $C_v(\vec{\Delta r}, \vec{r})$  is defined as

$$C_v(\vec{\Delta r}, \vec{r}) = \overline{[\Delta n(\vec{r}) \Delta n(\vec{r} + \vec{\Delta r})]} / [\overline{\Delta n(\vec{r})}]^2 \quad (1.36)$$

Substituting this in the above relation, one gets

$$\overline{\Phi_R} = \overline{\Phi_r} \int_V \overline{\Delta n(\vec{r})}^2 \int_{\Delta \vec{r}} C_v(\vec{\Delta r}, \vec{r}) \exp[-2j\vec{k} \cdot \vec{\Delta r}] d^3(\vec{\Delta r}) d^3(\vec{r}) \quad (1.37)$$

The three dimensional spectrum of density fluctuations is defined as,

$$S_v(\vec{k}, \vec{r}) = \int_{\Delta \vec{r}} C_v(\vec{\Delta r}, \vec{r}) \exp[-j(\vec{k} \cdot \vec{\Delta r})] d^3(\vec{\Delta r}) \quad (1.38)$$

since Fourier transform of the auto covariance function gives the power spectrum. Using this relation, equation

(1.37) for the scattered flux can be written as,

$$\overline{\Phi_R} = \overline{\Phi_r} \int_V S_v(\vec{k}, \vec{r}) [\overline{\Delta n(\vec{r})}]^2 d^3(\vec{r}) \quad (1.39)$$

where  $\vec{x} = 2\vec{k}$

Taking into consideration the variation of  $\Phi_r$  with  $\vec{r}$  the expression for the flux can be rewritten as

$$\overline{\Phi_R(\vec{x})} = \int_V \Phi_r(\vec{r}) S_v(\vec{x}, \vec{r}) [\Delta n(\vec{r})]^2 d^3(\vec{r}) \quad (1.40)$$

This relation shows that the radio wave responds only to a narrow band of Fourier components of the fluctuation spectrum having wave numbers centred at  $\vec{x} = 2\vec{k}$ . Thus electron density fluctuations of scale size  $\lambda = \lambda_0/2$  where  $\lambda_0$  is the wavelength of the radio wave, are resolved by the radio wave and are responsible for the scattered flux at the receiver.

(a) Distribution of received signal amplitude and phase

The signal voltage  $S$  induced at the receiving antenna is proportional to the scattered field at the antenna. If one assumes that the receiving antenna has uniform amplitude and phase patterns within the solid angle subtended by the scattering volume, from equation (1.28), one can write

$$S \propto \sum_{i=1}^N \exp[-j r_i \cdot 2k]$$

or

$$S \propto \sum_{i=1}^N \exp[j \phi_i] \quad \text{where } \phi_i = -2k r_i$$

Let us assume that the particles do not interact mutually. Since the exponential in the above equation is an oscillating function, the phase can be considered modulo and hence uniformly distributed throughout the range 0 to  $2\pi$ .



Then,

$$p(\phi_i)d\phi_i = \frac{d\phi_i}{2\pi} \quad 0 \leq \phi_i \leq 2\pi$$

$$= 0 \text{ elsewhere.}$$

This expresses the probability  $p(\phi_i)d(\phi_i)$ , that the phase be encountered at any arbitrary instant within the range  $\phi_i$  to  $\phi_i + d\phi_i$ . The resultant antenna voltage  $V_r$  is then the resultant of a random variation. The solution to this problem first given by Rayleigh (1871), is that the phase of the resultant is uniformly distributed module  $2\pi$ , and the amplitude is distributed according to,

$$p(|V_r|)d|V_r| = \frac{2|V_r|}{\langle |V_r|^2 \rangle^{1/2}} \exp\left[\frac{-|V_r|^2}{\langle |V_r|^2 \rangle}\right] \quad (1.41)$$

A condition for the validity of this distribution is that

$$\frac{\overline{\phi_i \phi_l} - (\overline{\phi_i})^2}{\overline{\phi_i^2} - (\overline{\phi_i})^2} = \begin{cases} 0 & i \neq l \\ 1 & i = l \end{cases}$$

(b) Signal frequency spectrum

For physical studies of the medium one frequently requires complete knowledge of the frequency spectrum of the scattered radiation. If the existence and position of every scattering centre is independent of all other centres, then the spectrum takes on a particularly simple form. From the doppler relationship we have,

$$\begin{aligned} \omega_{iR} &= \omega_0 - 2v_{ir} k \\ &= \omega_0 - \vec{v}_{ir} \cdot \vec{k} \quad (\vec{k} = 2\vec{k}') \end{aligned}$$

where  $\omega_{iR}$  is the frequency of the wave received from the  $i^{\text{th}}$  scattering centre and  $v_{ir}$  is the component of the

velocity of the  $i^{\text{th}}$  centre in the direction of wave propagation. Then one finds that

$$\phi_R(\omega_R) d(\omega_R) \propto p(v_r) d(v_r)$$

where  $\phi_R(\omega_R) d(\omega_R)$  is the flux at the receiver due to scattered waves with frequencies between  $\omega_R$  and  $\omega_R + d\omega_R$  and  $p(v_r) d(v_r)$  is the probability of finding  $v_r$  between  $v_r$  and  $v_r + dv_r$ . In other words, the spectrum of the scattered signal has the same mathematical shape as the probability density function of velocities of the scattering centres.

In the general case applied to the ionosphere it is not possible to regard the individual free electrons as statistically independent scattering centres. While the irregularities of electron density can be thought of as independent centres, the amplitudes of their individual contributions are not constant. This modulation has an effect on the total received spectrum. Rewriting equation (1.23) for the scattered field strength at the receiving antenna

$$e_R = E_r \exp[j(\omega_0 t - 2kR)] \sum_{i=1}^N \exp[-2jk r_i]$$

which in the vector form can be simplified to,

$$e_R = E_r \exp[j(\omega_0 t - 2kR)] \int_V \Delta n(\vec{r}) \exp[-j(\vec{r} \cdot \vec{x})] d^3(\vec{r}) \quad (1.42)$$

The electron density fluctuations at the point  $\vec{r}$  is a function of time. The autocorrelation function of the received signal with respect to time, then, gives the Fourier transform of the frequency spectrum according to the Wiener Khinchine theorem. Thus

$$\overline{e_R^*(t) \cdot e_R(t+\tau)} = E_r \exp(j\omega_0\tau) \int_V \int_{\Delta\vec{r}} \overline{\Delta n(\vec{r}, t) \cdot \Delta n(\vec{r} + \Delta\vec{r}, t + \tau) \cdot \exp\{j(\Delta\vec{r} \cdot \vec{k})\}} d^3\vec{r} \quad (1.43)$$

Let  $\rho_E(\tau)$  be the normalised autocorrelation function of the received field

$$\rho_E(\tau) = \overline{e_R^*(t) \cdot e_R(t+\tau)} / |e_R|^2 \quad (1.44)$$

Then by the Wiener-Khinchine theorem, the frequency power spectrum is obtained by

$$W_R = \int_{-\infty}^{+\infty} \rho_E(\tau) \cdot \exp(-j\omega\tau) d\tau \quad (1.45)$$

As pointed out earlier the scattered signal can be regarded as arising from a series of plane wave-like irregularities with wave number  $\vec{K} = 2\vec{k}$  in the direction of propagation. The ensemble averaging over many realizations to obtain the mean scattered power amounted to sampling many such fixed plane waves having variable amplitude and phase. One can decompose each of the plane wave components with wave number  $\vec{K}$  into a

spectrum of plane waves  $S_v(\vec{x}, v_{\vec{x}})$  with the same wave number but travelling at different velocities  $v_{\vec{x}}$  in the  $\vec{x}$  direction. Then as pointed out earlier the frequency spectrum of the received signal would be proportional to the spectrum of velocities and of the same form. In some cases the normalised spectra of all the elementary waves might be the same. Then the received frequency spectrum would be the convolution of the first spectrum derived from velocities, with the second spectrum derived from the time variations. This convolution is the Fourier transform of the product of the autocorrelation functions corresponding to the two spectra.

The signal voltage induced at the antenna as mentioned earlier, is a measure of the scattered electric field at the receiving antenna.

If  $\phi(t)$  is the resultant phase of the received signal, then

$$V_r(t) = V_r \exp[j\{\omega_0 t + \phi(t)\}] \quad \text{--- (1.46)}$$

represents the received signal at time  $t$ . The expression for the frequency power spectrum can be obtained by taking the Fourier transform of the normalised auto correlation function of  $V_r(t)$ . By using synchronous detection the complex voltage  $V_r(t)$  can be separated into real and imaginary parts obtained at separate terminals and later used for the power spectral computations. A synchronous detector performs the operation:

$$V_r \exp\{j[\omega_0 t + \phi(t)]\} \times \exp(-j\omega_0 t) = V_r \cos \phi(t) + j V_r \sin \phi(t)$$

$V_r \cos \phi(t)$ , the real part and  $V_r \sin \phi(t)$ , the imaginary part are obtained separately.

### 1.3 Irregularities in the electrojet

#### 1.3.1 Nature and Generation of irregularities

Phenomena, such as Es-q, spread-F, radio star scintillations, H.F. and V.H.F. scatter, are familiar manifestations of the ionisation irregularities existing in the earth's ionosphere. A close connection between Es-q and the equatorial electrojet was shown by Matsushita in 1951., who pointed out that in the equatorial region, the intensity variations with latitude of the horizontal component of the magnetic field correlates extremely well with corresponding variations in the Es-q intensity. These results were confirmed later by Bowles and Cohen (1957/58) in a series of radio-star scintillation experiments at various stations close to the magnetic equator. Cohen and Bowles, (1963) using their VHF forward scatter radar, over a trans-equatorial path, showed that the irregularities are generated in the height region 95 to 110 km. a range that agreed well with the limits of the electrojet current system determined by Singer, Maple and Bowen (1951). The field aligned nature of these ionisation irregularities were shown by the radar studies at Jicamarca. The studies of the vertical structure of the irregularities and their motion using the VHF scatter radar at Jicamarca, have given very interesting results.

But the processes through which these irregularities are generated and the local conditions responsible for their generation cannot be clearly understood with ground based techniques alone. With the advent of rockets and satellites for research investigations a new dimension was added to the scope of these results and the irregularities could be studied directly using in-situ probes.

These observations have shown the existence of several types of irregularities. While the presently known theories can explain very qualitatively some of the observations, there exist many observations for which suitable theories are yet to be developed. The important known types of irregularities observed in the electrojet region and which are of interest in the present studies are briefly discussed here along with the probable mechanisms responsible for their generation.

1. Streaming instabilities and the type I irregularities

These irregularities are associated with the streaming of electrons in the electrojet region and were first observed with back scatter radar at Jicamarca. The detailed properties of these irregularities, as observed with back scatter radar is discussed in section (1.3.2). These irregularities have been classified as type I by Balsley (1969). Farley (1963) and Buneman (1963) independently developed the theory of two stream instability mechanism to explain the generation

of the irregularities due to streaming of electrons. This mechanism operates when the streaming velocity of electrons exceeds the ion acoustic velocity in the medium.

The rocket observations at Thumba have also given very useful information about these irregularities (Prakash et al; 1971a,b, 1973, 1974). The rocket observations showed that these irregularities have scale sizes in the range of 1 to 15 meters and are observed in the region around 105 km where the streaming velocity of electrons is largest. These irregularities occur more or less continuously in this region and have a flat spectrum with spectral index zero. The flatness of this spectrum showed that they are not generated through the decay of irregularities of large scale sizes.

Kaw (1972) has put forward the theory of electromagnetic instability which can give rise to enhanced streaming of electrons. If these irregularities are present, the streaming instabilities will be observed even when the average streaming of electrons is less than the ion acoustic velocity.

## 2. Cross field instability and the type II irregularities

Rocket observations at Thumba showed the existence of irregularities in the scale size range of about 1-300 meters at regions where the back ground electron density profile exhibited a gradient. From radar observations, these are classified as type II irregularities. The generation of these irregularities is attributed to

crossfield instability mechanism. Depending on the nature of generation, these can be grouped into two: (i) Irregularities with scale sizes in the range 30-300 meters observed in the height region of about 90 to 130 kms and (ii) irregularities in the scale size range of 1 to 15 meters which occur in the same height region as the 30-300 meter scale size irregularities but have much smaller amplitudes.

Rocket observations (Prakash et al, 1971) show that the irregularities in the scale size range of 30-300 meters have amplitudes varying right from a few percent to about 30 percent. During day light hours and evening twilight hours the irregularities are found to occur in regions of upward electron density gradients, whereas during night time they occur in regions of downward electron density gradients. During day time the irregularities have large amplitude (more than 20%) around 85 kms. The amplitudes decrease with increasing height, and reach a value of about 5% around 95 kms. Above 95 kms. the amplitudes show a rapid decrease. During night time also, irregularities with amplitudes as large as 30% were observed but were confined to an extended height region from 90 to 130 kms. During evening hours these irregularities were observed both in 85 to 100 km and 140 km region, though the amplitudes in the upper region were smaller. The amplitude and size of the irregularities were found to decrease with increase in electron density.



The irregularities were found to have a definite shape in the medium. They exhibited a saw tooth structure with a steeper rise in the electron density, than the fall during the ascent of the rocket, and a steeper fall in it than the rise, during descent of the rocket. On an average as one moves along the directions of the positive electron density gradients the increase in electron density is sharper than the decrease. The shape of the irregularities, possibly are related to their growth and decay processes.

Linear theories of cross field instabilities (Simon, 1963; Hoh, 1963; Maeda et al, 1963; Tsuda et al, 1966; White head, 1967; Reid, 1968; Rogister and D'Angelo, 1970) are qualitative and do not explain the observed features such as the shape of the irregularities and relationship with electron density. Linear analysis fails to tell the ultimate fate of an initial perturbation.

Non linear theories of the cross field instability have been developed by Kim and Simon (1969) and Hooper (1970) in the quasi linear regime, and Sato (1971) in both quasilinear and mode coupling regimes. Numerical analysis by Sato and Tsuda (1967), Tsuda and Sato (1968) and Sato et al. (1968) shows that the crossfield instability develops into a complete and rather stationary turbulent state through mode coupling. Relative amplitude of density fluctuations amounted to 30-50% under the saturation condition and a

phase mixing of each mode occurred, resulting in a prominent deformation of the initial fluctuation. Numerical studies of Ogawa (1972) and the theoretical studies of Ronglien (1974) on the cross field instability in the non linear regime show that the wave form becomes saw tooth or soliton like under saturation conditions. Ogawa found that the power spectrum of the density wave is approximately  $K^{-3}$  or softer. Rogister (1972) developed a non-linear theory which explains the energy transfer from large wave length to small wave lengths by mode coupling. The theory predicts a supra thermal fluctuation level in an appreciable range of wave lengths corresponding to linear stability. The order of magnitude of density fluctuations for the modes with maximum growth is 25% of the back ground density.

While the amplitudes of the irregularities in the scale size range 30-300 meters observed with the rocket observations at Thumba can be as high as 30%, irregularities in the scale size range 1 to 15 meters, have an amplitude of only a few per cent. Using a power law of the type  $E(K) = CK^n$  the spectral index  $n$  of this type of irregularities during evening hours, was found to be of the order of -4 for heights below 100 kms and -3 in the 110 and 140 km regions. During day time the spectral index was found to lie between -2 and -4 around 90 kms. and during night time it had a value of -4 at 95 kms and -3 around 120 kms. These values show a large scatter in the spectral indices. If one accepts

that large scale irregularities decay into small scale irregularities those with flatter spectrum are probably older in time. As these irregularities are confined to the same height regions as those with scale sizes in the range 30-300 meters, the two types seem to be somehow related. Balsley and Farley (1971), from a study of the electrojet irregularities at three frequencies 16 MHz, 50 MHz and 146 MHz which correspond to scale sizes of about 9, 3 and 1 metre respectively, reported that type I irregularities were observed right upto 146 MHz, while type II dominated around 16 MHz. This indicates that type I irregularities have a flatter spectrum than type II. A steep spectrum for the type of irregularities discussed above indicate that they are similar to the type II irregularities identified from radar studies. The occurrence of type II irregularities on most of the rocket flights give additional support to the hypothesis that they are same.

Linear theories of crossfield instability do not even qualitatively explain the 1-15 meter scale size irregularities. Rogister and D'Angelo (1972) have suggested a non linear excitation of the crossfield instability in the equatorial electrojet. For the height region where  $\frac{\nu_e \nu_i}{\omega_e \omega_i} \ll 1$  they have calculated the largest wave number of which the fluctuations can be excited non-linearly and have found  $\lambda_{min} \approx 4m$ . in the non linear regime. Sudan (1973) proposed the generation of small scale irregularities from

horizontally propagating large scale irregularities with wave lengths of 50 to 100 meters or more. These irregularities produce horizontal gradients much larger than the original vertical gradients and vertical drifts as large as the original horizontal drifts. These in turn lead to the generation of vertically propagating irregularities. Typical wave lengths of about 6 to 7 metres are accounted for by this theory.

### 1.3.2. Radar studies of the electrojet irregularities

A close relationship between Esq and the equatorial electrojet was first demonstrated by Matsushita in the year 1951 (Matsushita, 1951). He showed that the variation with latitude in currents in the electrojet region as shown by variations in the horizontal component of the geomagnetic field correlated extremely well with corresponding variations in the Sq intensity. This point was given further evidence, when Cohen and Bowles (1963), showed from radar studies that time variations in the radar echo intensity correlated quite well with variations in the horizontal component of the geomagnetic field. In an experiment reported by Egan (1960) during the International Geophysical Year (1957/58) it was indicated that the E-region irregularities seen by an oblique looking radar at Huancayo, Peru (dip latitude  $0^{\circ} 30'N$ ) were strongly field aligned confirming an earlier prediction by Bowles and Cohen (1957). By field aligned, it is meant that the dimensions, or correlation distances of the

irregularities are much greater in the direction parallel to the magnetic field than in a transverse direction. An aspect sensitivity was, hence, observed in the radar echoes. Radar echoes were obtained only when the beam was oriented in a direction nearly perpendicular to the magnetic field.

Another experiment performed at Huancayo (Bowles et al. 1960) established that the predominant echoing centres in the day time electrojet as seen by the VHF radar, were plane wave electron density irregularities. These plane waves travelled more or less towards the west in the direction of the electron flow. These observations were consistent with a modified theory of the two-stream plasma instability later developed by Farley (1963). An increase in the apparent radar echo cross section with antenna elevation angle reported by Bowles et al. (1963) was a supporting evidence for the two stream theory as propounded by Farley. These irregularities were observed only when the electrojet current exceeded a critical value (Bowles et al. 1963) and this threshold effect was higher for echoes observed at 148 MHz than those at 50 MHz.

The two-stream instability theory failed to account for the VHF radar spectra with frequency shifts less than the threshold predicted by the theory. At times such spectra dominated over the spectra produced by two-stream instabilities, particularly when the radar antenna was directed vertically (Cohen et al, 1963). The normal

mid day echoes were observed (Balsley, 1965) to come from the entire vertical extent of the region; but a marked splitting of the region occurred at periods well separated from mid day. This observation could not be predicted from the two-stream theory. The large scale irregularities with dimensions of the order of a few kms. which were observed drifting in the general direction of the electron flow, also could not be explained by the two-stream theory.

The general picture which emerges from all these observations indicates that there are at least two separate irregularity producing mechanisms in the electrojet. Irregularities produced by the two-stream instability mechanism, classified as type I from spectral characteristics, predominates during periods of high current density, producing plane wave irregularities which travel at the ion-acoustic velocity. The slower moving irregularities are classified as type II, from their spectral characteristics as discussed in the next section. The generation of these irregularities is by the cross field instability mechanism as clearly shown by the rocket observations at Thumba (Prakash et al. 1971a,b, 1972).

#### Spectral characteristics of type I and type II echoes

A typical example of the two stream or type I spectra (Balsley, 1967) is shown in figure (1.2a). It can be seen that most of the returned power is displaced from the transmitted frequency by about 120 Hz. which corresponds to

a velocity of the echoing centres, near to the ion acoustic velocity. The observed Doppler shift for this type of irregularity is essentially independent of the antenna elevation angle. During day time, a westward antenna beam, gives rise to negative doppler shift, which shows that the irregularities are moving in a generally westward direction.

Figure (1.2b) shows a spectrum obtained when both type I and type II echoes are present. There is a well defined peak displaced from the transmitted frequency by about 120 Hz. An appreciable portion of the received power has been returned from irregularities which are moving at velocities less than the ion acoustic velocity. Assuming a symmetry in the type I spectrum about its peak, one can split the spectral curve into two curves, one representing the power scattered by type I irregularities and another by type II irregularities. This method of spectral decomposition technique has been used by Cohen (1973) in analysing the radar spectra. He suggests that there are frequently two or more strata containing type II irregularities.

Figure (1.2c) represents a typical type II spectrum. This in general is broader than the type I spectrum. The drift velocity of type II irregularities is related to the doppler shift of the received echo by the relation.

$$\delta f = \frac{2v_d f \sin \theta}{c}$$

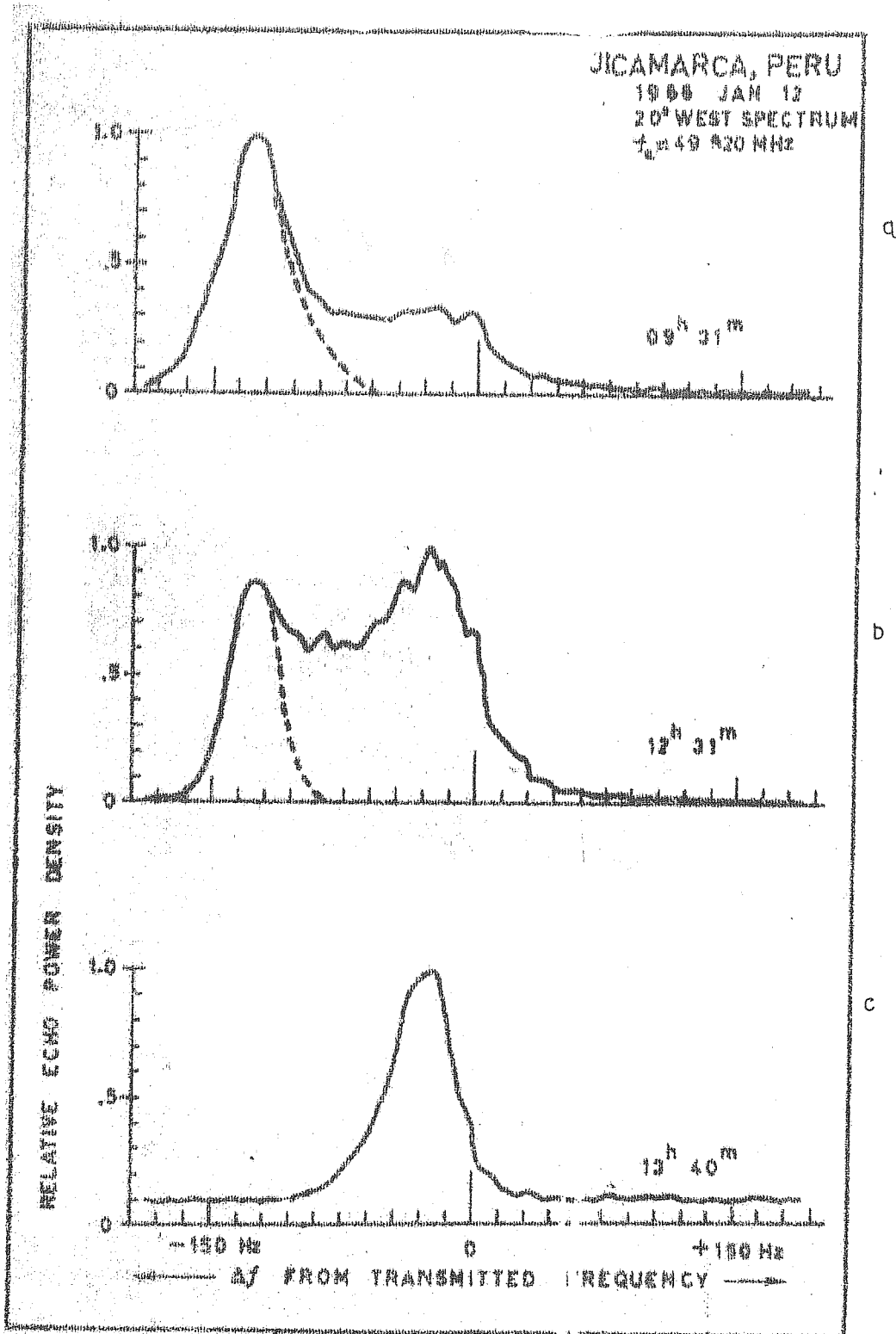


FIG. 1.02



### Relative power of type I and type II echoes

To obtain information on the relative power between type I and type II echoes when both are apparent in a spectrum an obvious assumption is that type I irregularity will produce a symmetrical spectrum about the ion acoustic velocity (Balsley 1967). Total area under a spectral curve may be equated to the total returned echo power. The area under the spectral curve assumed to represent the type I echo, gives the power contained in the type I echo. The difference between these two power estimates then gives the power contained in the type II echo. In general, the type II echo power shows a decrease with increase in the type I echo power.

A quantitative relationship between the type II echo power and the drift velocity of electrons as reported by Balsley (1967) is shown in figure (1.3). The data points corresponding to drift velocities between about 50 m/sec and 300 m/sec are well grouped about a straight line and it is an indication of the power law relationship between the variables. As noted in the figure, the relation is given by

$$P_r = C_0 v_d^2$$

where  $P_r$  is the relative average received power and  $C_0$  is an arbitrary constant. The amplitude of the radar echo is proportional to  $P_r^{1/2}$  and hence is proportional to the drift velocity  $v_d$  of the type II irregularities. Since

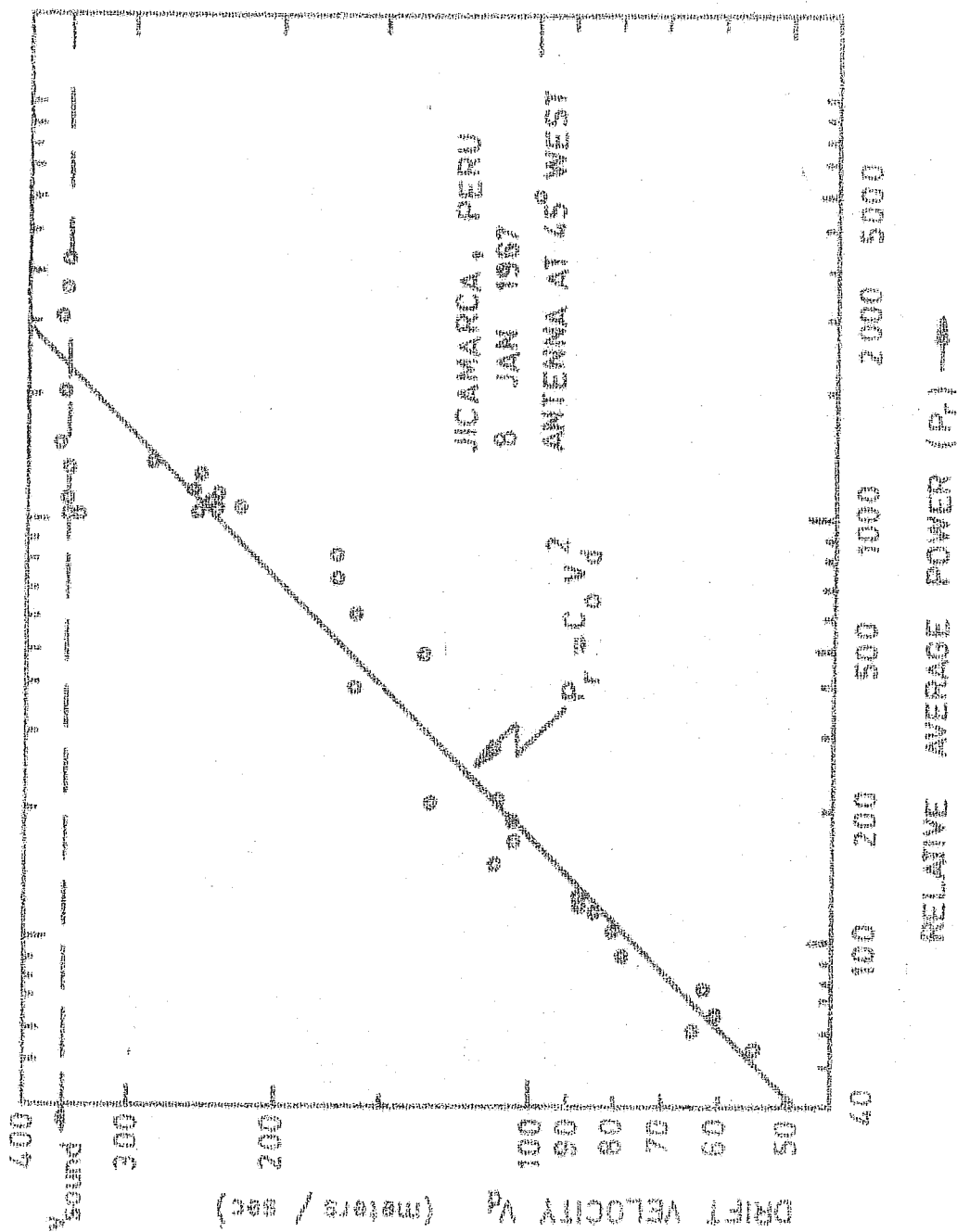


FIG - 103

the variation in the electron density is much less when compared with the variation in  $V_d$  the above relation is an indication of a linear relationship between the amplitude of the radar echo and the strength of the electrojet currents. The significance of these results in the estimation of currents above the electrojet region are discussed in section (6.3.2)

#### 1.4 Scope of the present studies

Ground based and rocket borne measurements have been used to study the average picture of the electrojet current system and its variation with time. Even with the vast amount of information available on electrojet many of the important features of the current system are not yet understood. For example, how the world wide Sq current system is connected with the equatorial electrojet is yet to be clearly known. The dynamo electric field being the primary force driving the electrojet as well as the Sq currents, requires a special study, as regards to its time variations and the location of its sources in order to establish the nature of relationship, if any, existing between the current systems. Though the direct measurement of these electric fields will solve the problem, the technical difficulties involved in these measurements and the accuracy of the results that can be obtained from such measurements, diverts one towards indirect estimates of the nature of these fields. This has been one of the main objectives of the present studies.

Study of the nature of variation of the electric fields with altitude is of significant importance in understanding the location of the sources of these fields. In-situ measurements of the electron density and current density profiles were used for the indirect estimation of the variation with altitude of the electric fields driving these currents.

Morning and evening hours being periods associated with the reversal of the electrojet currents, an understanding of the variation of the electric fields during these periods seems to be indispensable in locating the sources of these fields. This aspect of the problem has been studied using a VHF back scatter radar installed at Thumba, an equatorial station.

Day time reversals (counter electrojet) in the normal direction of flow of currents in the electrojet region is one of the most important sources of information in the study of the nature of the electrojet currents. Though this still continues to be an important problem of present day studies little seems to be understood so far. The back scatter radar at Thumba was used to study a few aspects of this problem and the significance of the results obtained are discussed.

The time variation in the H component of the geomagnetic field at an equatorial station is closely related to the variations in the ionospheric currents. The radar echo is associated with the irregularities in the electrojet region. A comparative study of these two parameters hence is expected to give the nature of the distribution of currents in the ionospheric region. In turn, such an understanding of the distribution of currents, is essential in the investigation of the morphology of the three dimensional current system. This and associated problems were studied using the back-scatter radar at Thumba.

## C H A P T E R - II

### Instrumentation and Data reduction

#### 2.1.1 System in general

VHF signals are transmitted in the form of pulses. The scattered signal from the irregularities is analysed through high gain receivers. The amplitude and spectral variations in the radar echo are recorded and analysed. The whole system used for this is shown schematically in figure (2.1).

54.95 MHz continuous waveform generated in the programmer unit is modulated by pulses of variable width and variable repetition rate. The pulsed VHF signal thus obtained is amplified through a number of stages to the required power level and transmitted using an antenna array vertically or obliquely as required. The transmitted electromagnetic waves are scattered by the ionisation irregularities in the upper atmosphere. An identical antenna array receives the radar returns, and sends the signal into two receivers, through a two way power divider. One of the receivers after a series of intermediate frequency conversion and amplification stages, sends the average variations in the amplitude of the signal, to a strip chart recorder. The other receiver, taps the informations regarding the doppler shift in frequency of the signal; and generates the complex voltage signal representing the doppler

#

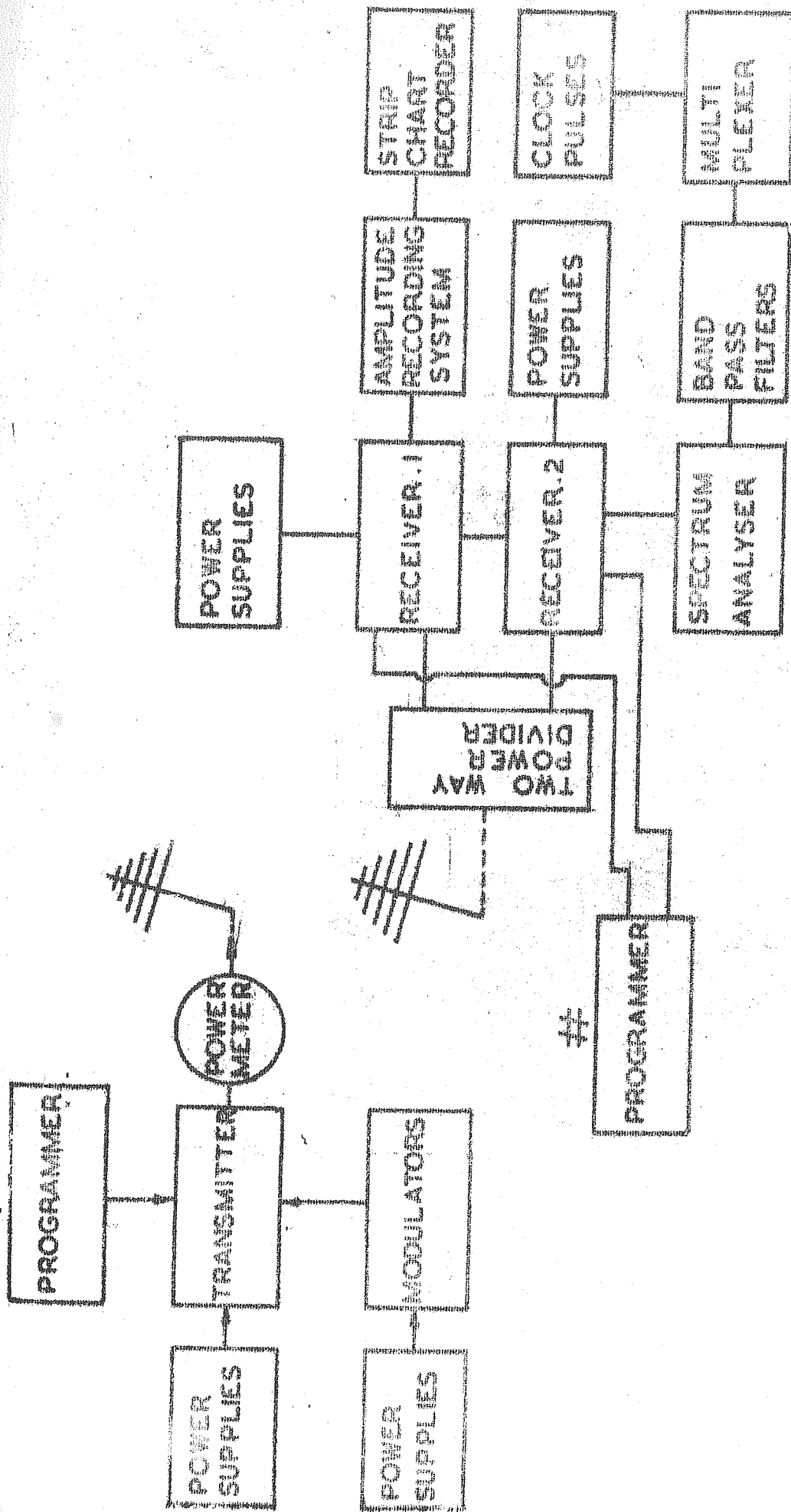


FIG.- 2.01

BLOCK DIAGRAM OF THE BACK SCATTER  
RADAR SYSTEM.

frequency variations, in the form of two outputs. These two outputs are then fed to a spectrum analyser unit, where the relative amplitudes of the different frequency components are extracted using a set of band pass filters. The filter outputs are displayed on the scope, and photographs of the doppler spectra are taken. These recorded signal parameters are sampled and analysed later. The various sub units used in the signal recording, and the methods used for the data reduction are briefly explained in this chapter.

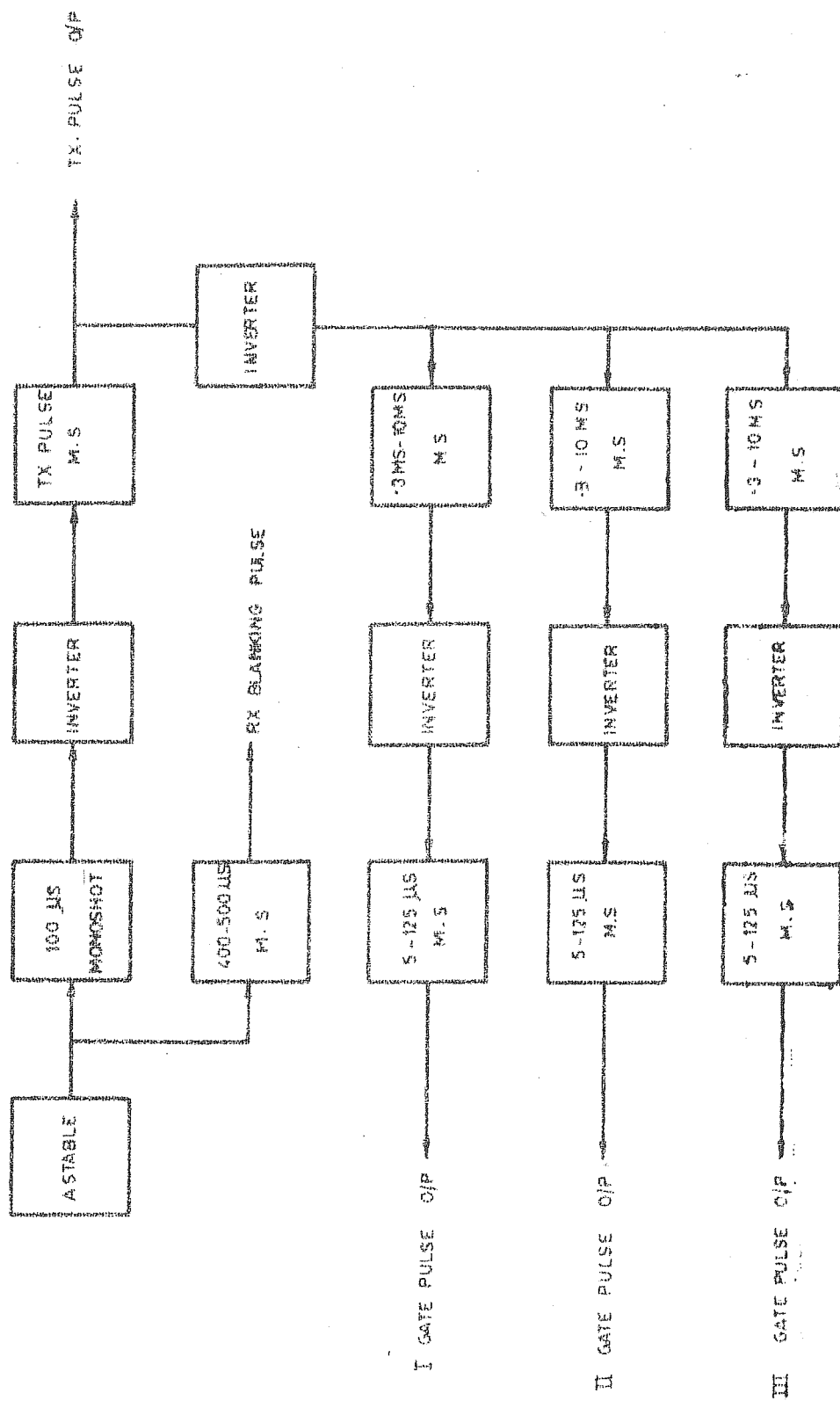
### 2.1.2 Programmer unit

The block diagram of the programmer unit is shown in figure (2.02). The astable multivibrator generates pulses, from which all the pulses used in the later stages are derived. The repetition rate of these pulses can be continuously varied in four ranges, the adjacent ranges being overlapping. The four ranges are shown below:

- i. 40 - 100 pps
- ii. 80 - 200 pps
- iii. 160 - 400 pps
- iv. 320 - 800 pps

The pulses from a  $100\ \mu\text{s}$  monoshot triggered by the pulses from the astable multivibrator are inverted and fed to the transmitter pulse monoshot. The astable multivibrator output, triggers a  $400\text{-}500\ \mu\text{s}$  monoshot which generates the receiver blanking pulses. The receiver blanking pulse is





51° 20' N 103° 05' W

generated, about 100  $\mu$ s before the Tx. pulse is generated.

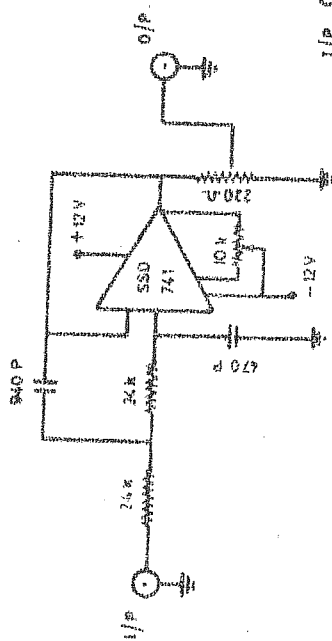
The width of the transmitter pulse is continuously variable from about 50  $\mu$ s to about 500  $\mu$ s in four overlapping discrete ranges.

The gate pulses, used for the height selection are derived from the transmitter pulse. The output from the first collector (inverted) is used to trigger three monoshots, which generate pulses of width continuously variable from 0.3 ms to 10 ms in three discrete overlapping ranges. Three height selection pulses of width variable from 5 to 125  $\mu$ s continuously in two discrete overlapping ranges are generated in three separate monoshots triggered by the three pulses from the above monoshots. The delays of these three height selection gates from the transmitted pulse are dependent on the widths of the monoshot outputs, and are independently variable.

The repetition rate and the width of the transmitted pulse are displayed digitally using nixie tubes, and hence can be continuously monitored.

The transmitter pulses of variable repetition rate and variable width, are used to modulate 54.95 MHz CW output from a crystal oscillator and is amplified to a power level of about 60 mw (fig 2.03) and fed to the exciter unit of the transmitter. The other pulses required for the different stages of amplification before transmission are also derived from the transmitter pulse.

# LOW PASS FILTER ( $F_c = 10\text{KHZ}$ )



## R.F. AMPLIFIER (POWER)

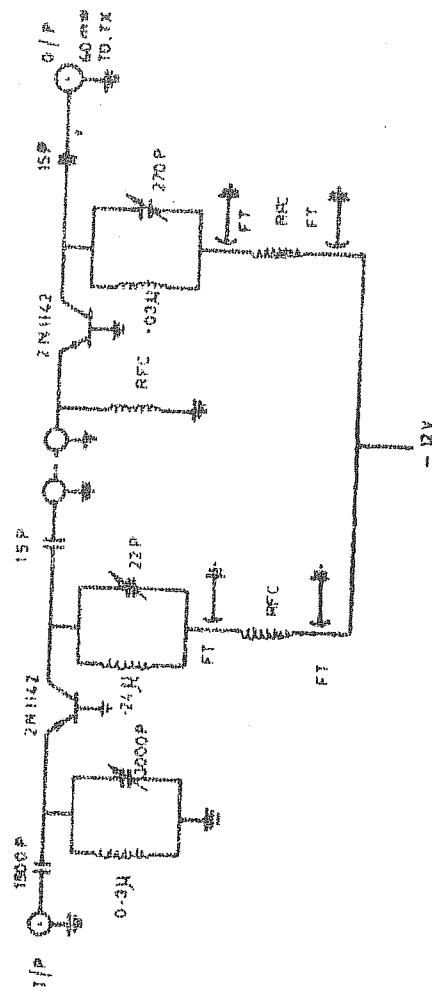


FIG. 2.03: LOW-PASS FILTER (CUT OFF FREQUENCY = 10KHZ.)  
AND 60MM R.F. POWER AMPLIFIER

### 2.1.3 Transmitter

The different stages of the transmitter unit, are shown schematically in figure (2.04). The 60 mw output from the programmer unit is fed to a three stage exciter unit (figure 2.05). The first stage raises the power level to about 2 watts and drives the second stage through a transformer coupling unit. This has an output of about 8 watts and is used to drive the third and final stage of the exciter. The exciter raises the power of the transmitter pulse to about 80 watts. This stage is terminated in a  $\Pi$  type matching network, which has an output impedance of  $52 \Omega$ .

The exciter output is used to drive the second stage namely the Driver amplifier stage (figure 2.06) of the transmitter, through a transformer coupling unit. The driver stage also has a  $\Pi$  type matching network at the output. The exciter output of 80W is much above the drive level (20 watts) of the driver amplifier. The driver output has a power level of about 1 KW and is sufficiently above the drive power required by the next power amplifier stage which is about 40W.

The power amplification in the third stage (figure 2.07) is done in two parallel steps using a BEL 400 tube in each stage. These two amplifier stages raise the peak power of the transmitter pulse to about 12 KW. The  $\Pi$  type matching network at the output of this stage, gives an output impedance of  $52 \Omega$ .

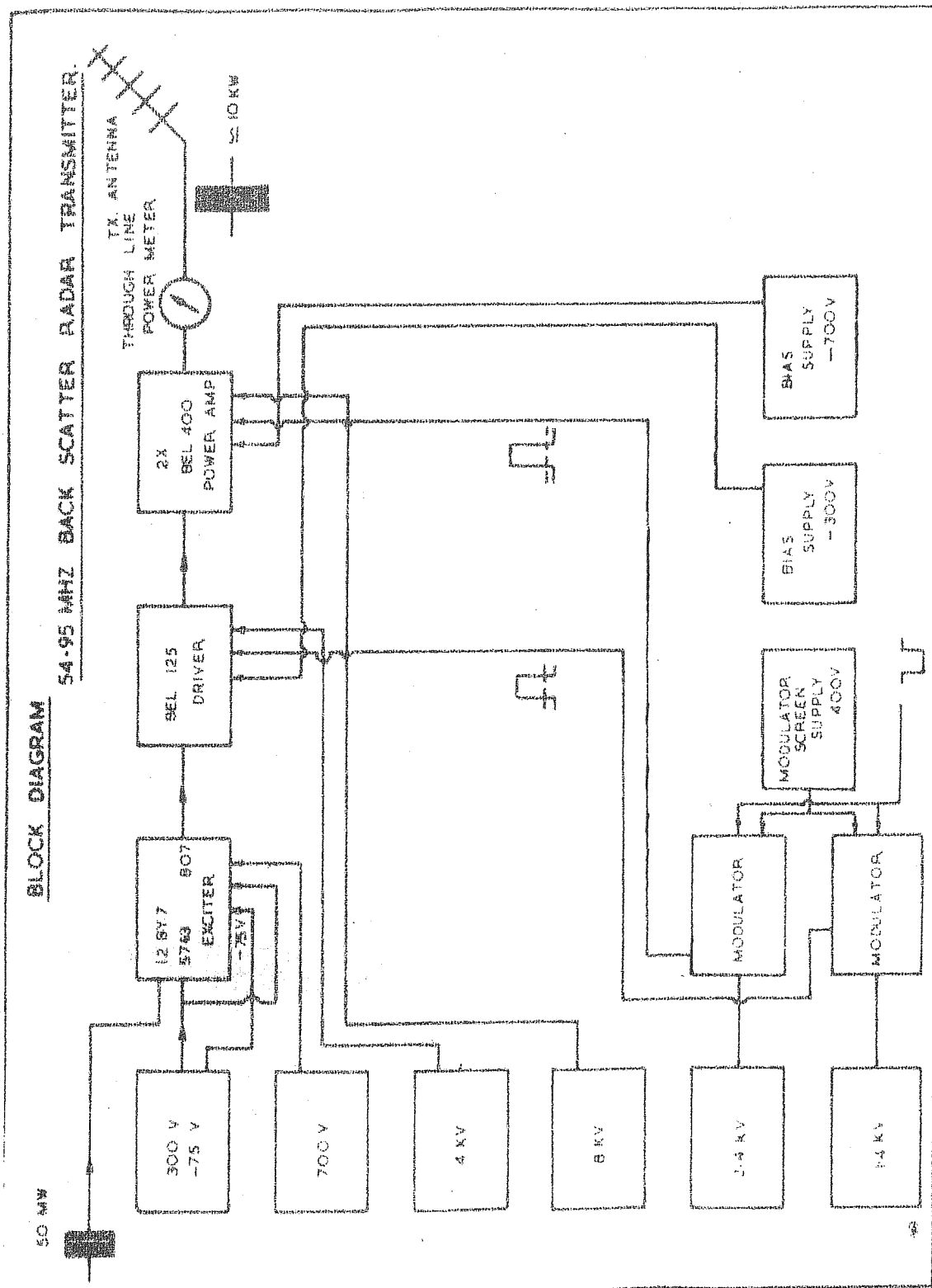
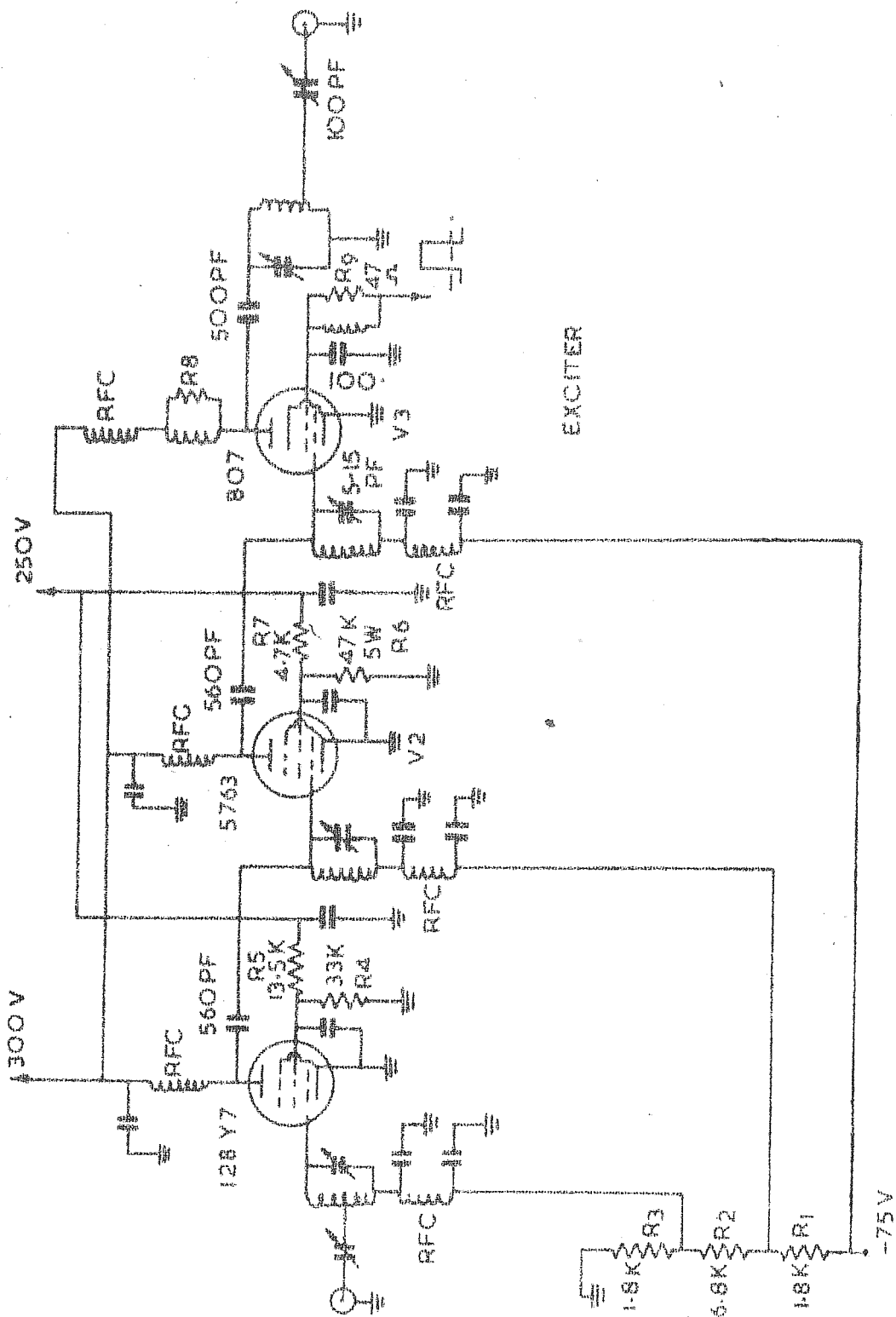


FIG. 7.04: BLOCK DIAGRAM OF 54.95MHz. TRANSMITTER UNIT



EXCITER

FIG. 2.05: EXCITER UNIT

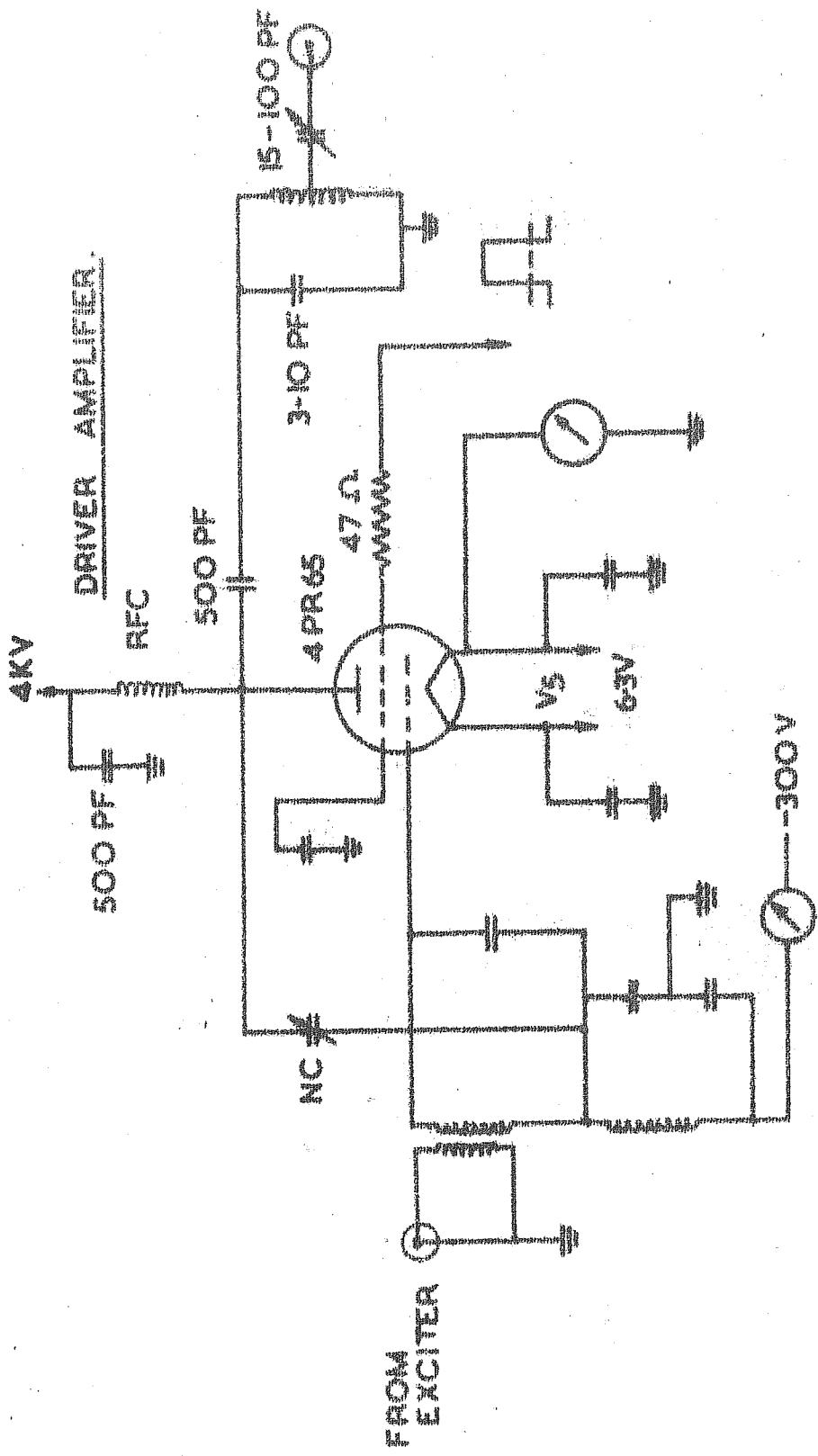


FIG. 2.06 DRIVER AMPLIFIER

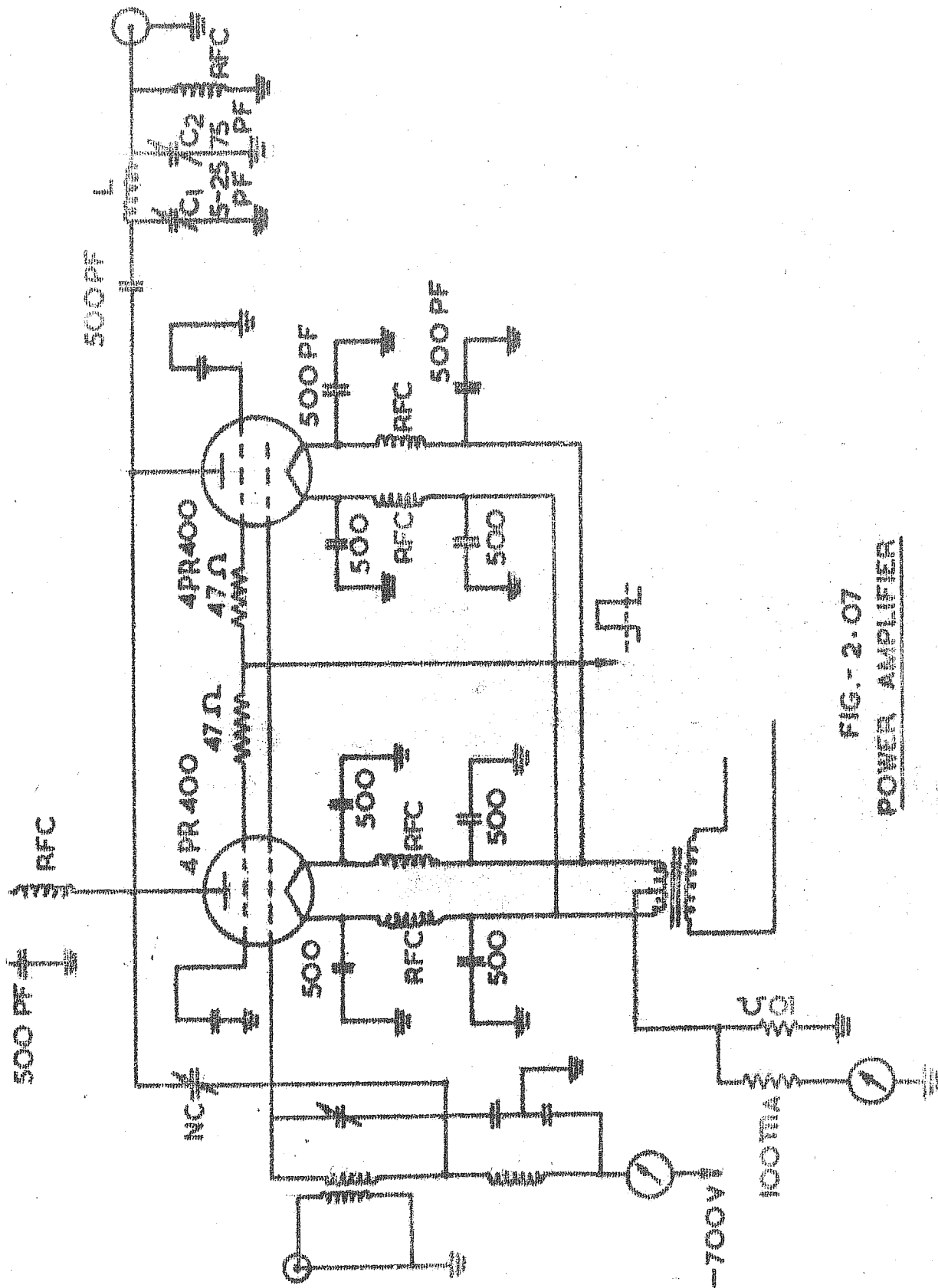


FIG. 2-07  
POWER AMPLIFIER



The supply voltages for the different elements of the tubes used in the transmitter are indicated in table (2.1). The screen grid supplies for the driver and power amplifier tubes are generated using two modulator units (figure 2.08). Other d.c. supplies are obtained using regulated power supply units. Table (2.1) shows all the supplies at different stages of amplifications, the coupling between the stages, and the intermediate power levels.

An on line power meter measures the peak power output of the transmitter before being fed to the transmitting antenna array. The fluctuations if any in the transmitted power can thus be continuously monitored. The power meter can also give the reflected power and hence the standing wave ratio can be obtained. Any mismatch between the transmitter output impedance and the antenna impedance can thus be observed and rectified.

#### 2.1.4 Receiving system

The receiving system consists of two receivers and associated recording and display systems. The two receivers are fed from a common receiving antenna array, through a two way power divider.

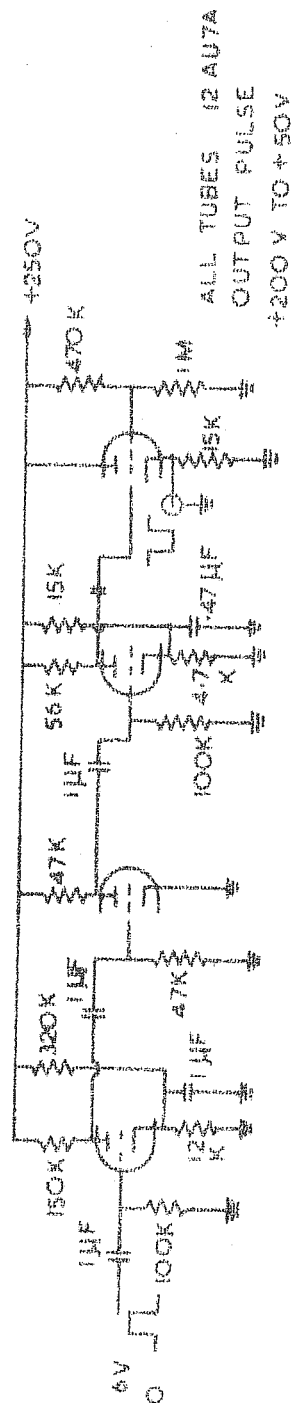
##### (a) Receiver for amplitude studies (Receiver I)

A block diagram of the receiver used for the study of time variations in the amplitude of the radar echo, is shown in figure (2.09). The circuit diagram of the initial I.F. and R.F. stages are shown in figure (2.12).

TABLE 2.1 TRANSMITTER SUB-UNITS, THE MODE OF COUPLING BETWEEN THEM AND THE INTERMEDIATE POWER LEVELS

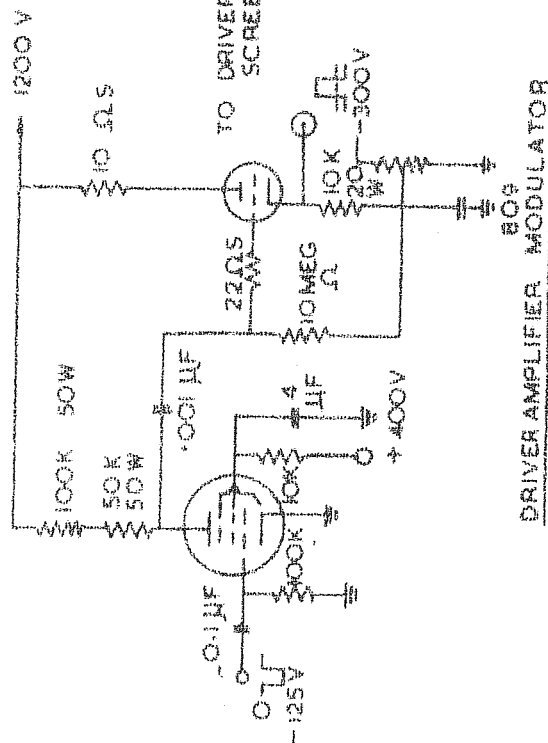
STAGE	VALVES USED	INPUT CIRCUITS IMPEDANCE	OUTPUT CIRCUITS IMPEDANCE	DRIVE POWER IN WATTS +	OUTPUT POWER IN WATTS	SUPPLY VOLTS				REMARKS
						PLATE	SCREEN	GRID	CATHODE +	
POWER AMPLIFIER	2 X BEL 400	TRANS-FORMER COUPLED	$\pi$ TYPE 52 $\Omega$ S	40 WATTS	12K WATTS	8000 V	-800 V +450 V PULSE	-700V	5V 14 Amps	+PER TUBE
DRIVER AMPLIFIER	BEL 125	TRANS-FORMER COUPLED	$\pi$ TYPE 52 $\Omega$ S	20 WATTS	1K WATTS	4000 V	-150 V +500 V PULSE	-300V	-75 V	
EXCITER	807	TRANS-FORMER COUPLED	$\pi$ TYPE 52 $\Omega$ S	0.4 WATTS	80 WATTS	700 V	+300 V	-75 V		
MODULATOR FOR POWER AMPLIFIER	5763	TRANS-FORMER COUPLED	TRANS-FORMER COUPLED	35 WATTS	8 WATTS	300V	270 V	-25.5V		
	12 BY 7	TRANS-FORMER COUPLED	TRANS-FORMER COUPLED	50m WATTS	2 WATTS	300 V	185 V	-5V		
	807	-	-	-	-	2400 V	+400 V	-	-	INPUT PULSE AMPLITUDE 0 TO -125 V
MODULATOR FOR DRIVER	3E 29	-	-	-	-	2400 V	-	-	-300V	OUTPUT PULSE AMPLITUDE -150V TO +450V
	807	-	-	-	-	1400 V	+400 V	-	-	INPUT PULSE AMPLITUDE 0 to -125V
DRIVER	809	-	-	-	-	1400 V	-	-	-300V	OUTPUT PULSE AMPLITUDE -150V TO +500V

# PULSE AMPLIFIER AND INVERTER CIRCUIT



ALL RESISTORS ARE 1WATT

## MODULATOR UNIT



## DRIVER AMPLIFIER MODULATOR

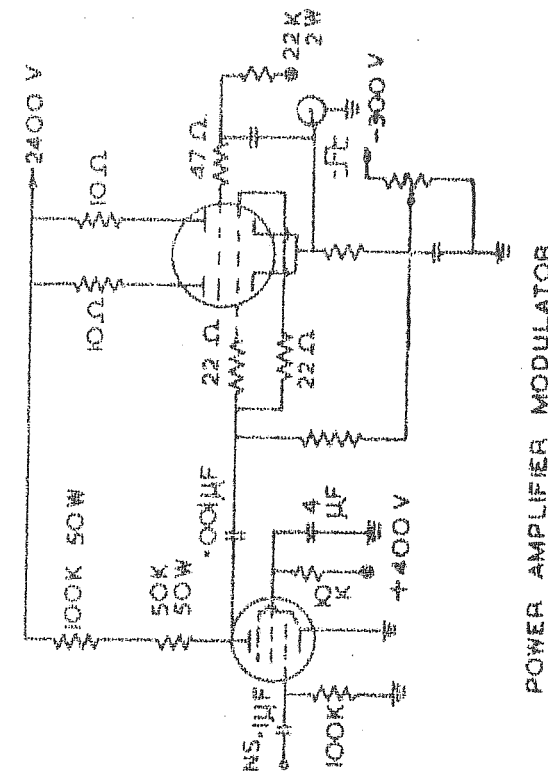


FIG. 2.08: MODULATOR UNIT; PULSE AMPLIFIER AND INVERTER, DRIVER AMPLIFIER MODULATOR AND POWER AMPLIFIER MODULATOR

# RECEIVER 1. AMPLITUDE STUDY

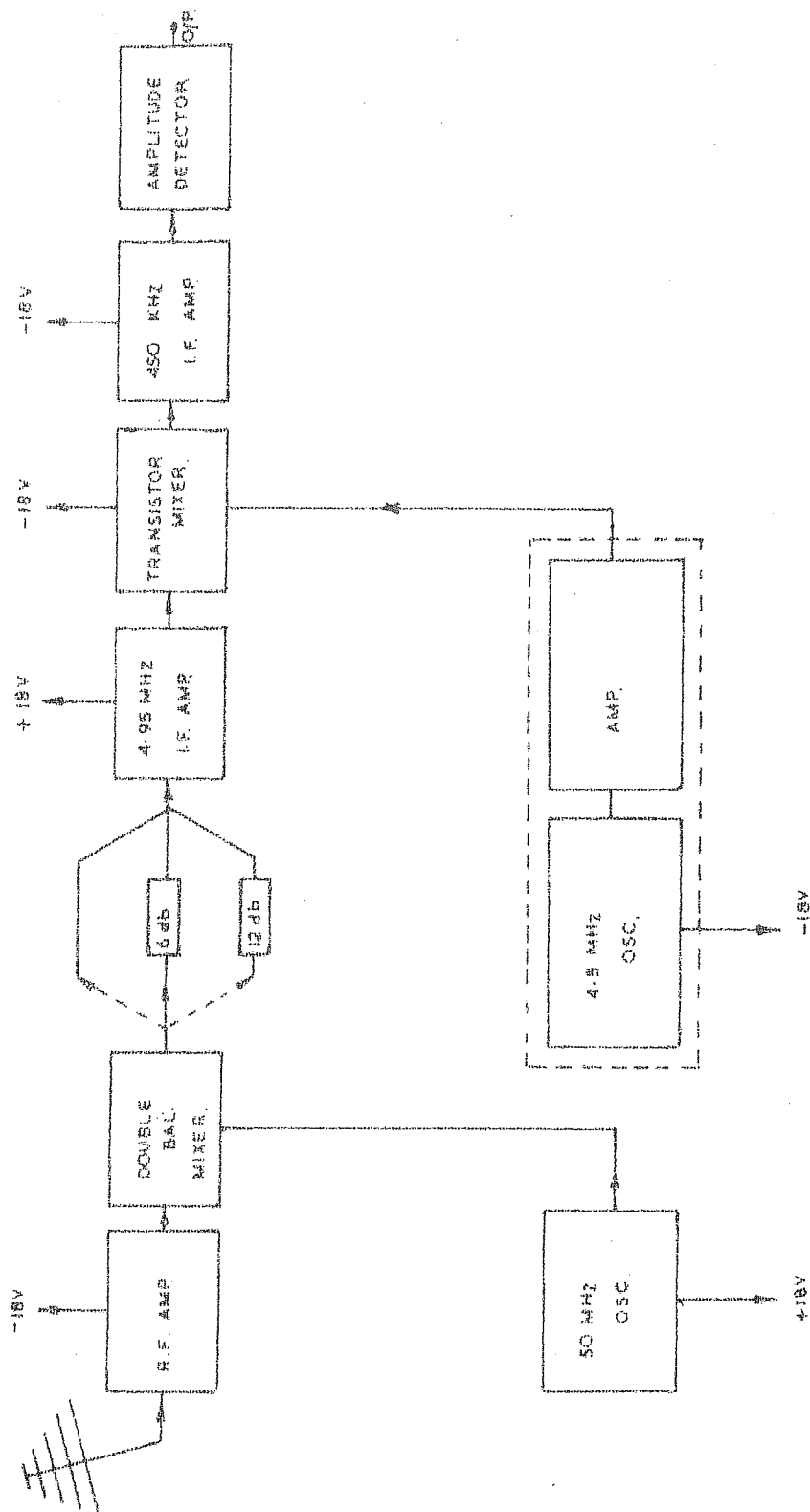


FIG. 2.09: BLOCK DIAGRAM OF RECEIVER 1

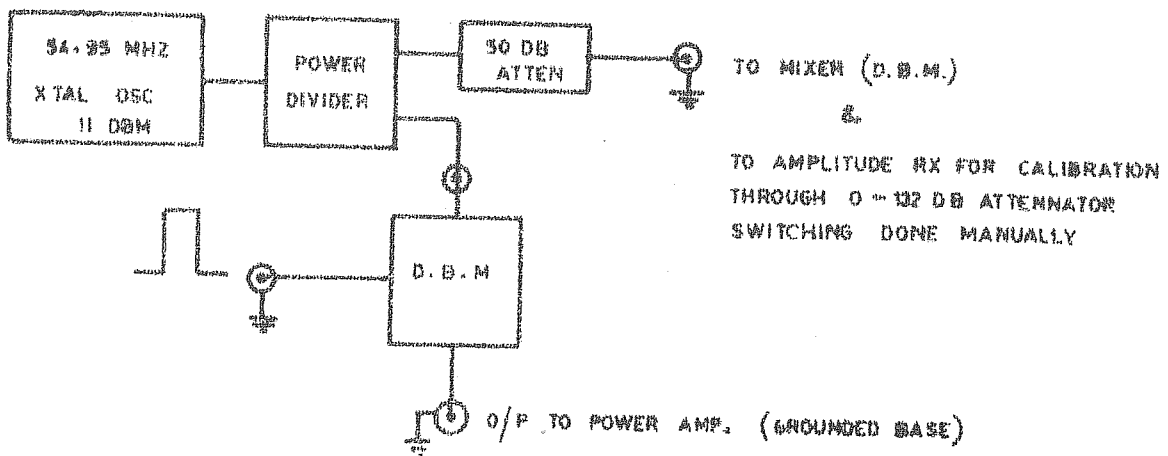


FIG. 2.10: RECEIVER CALIBRATION CIRCUIT

### SAMPLE AND HOLD

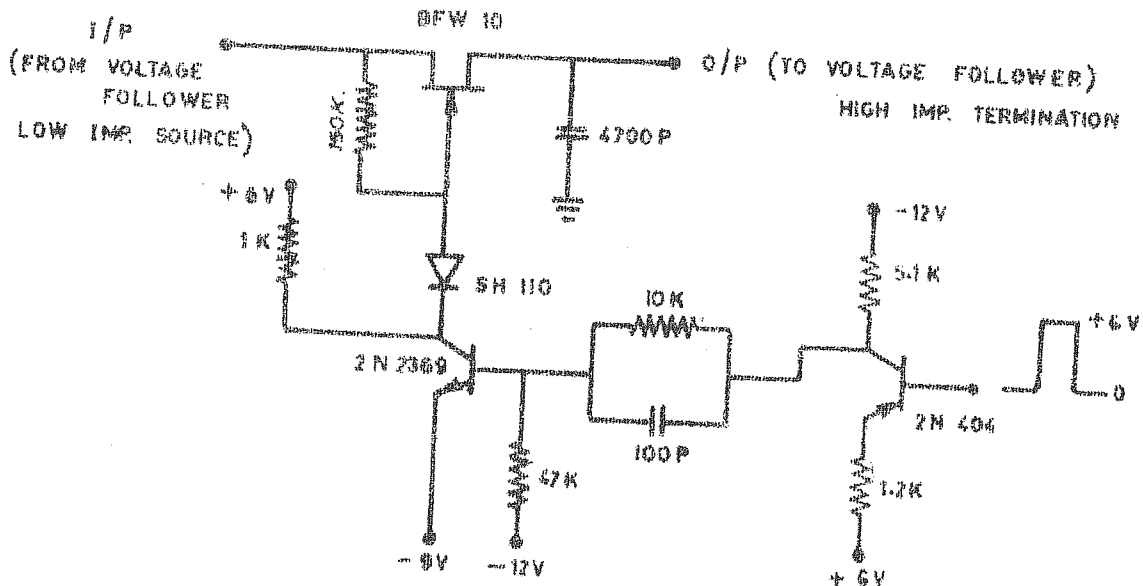


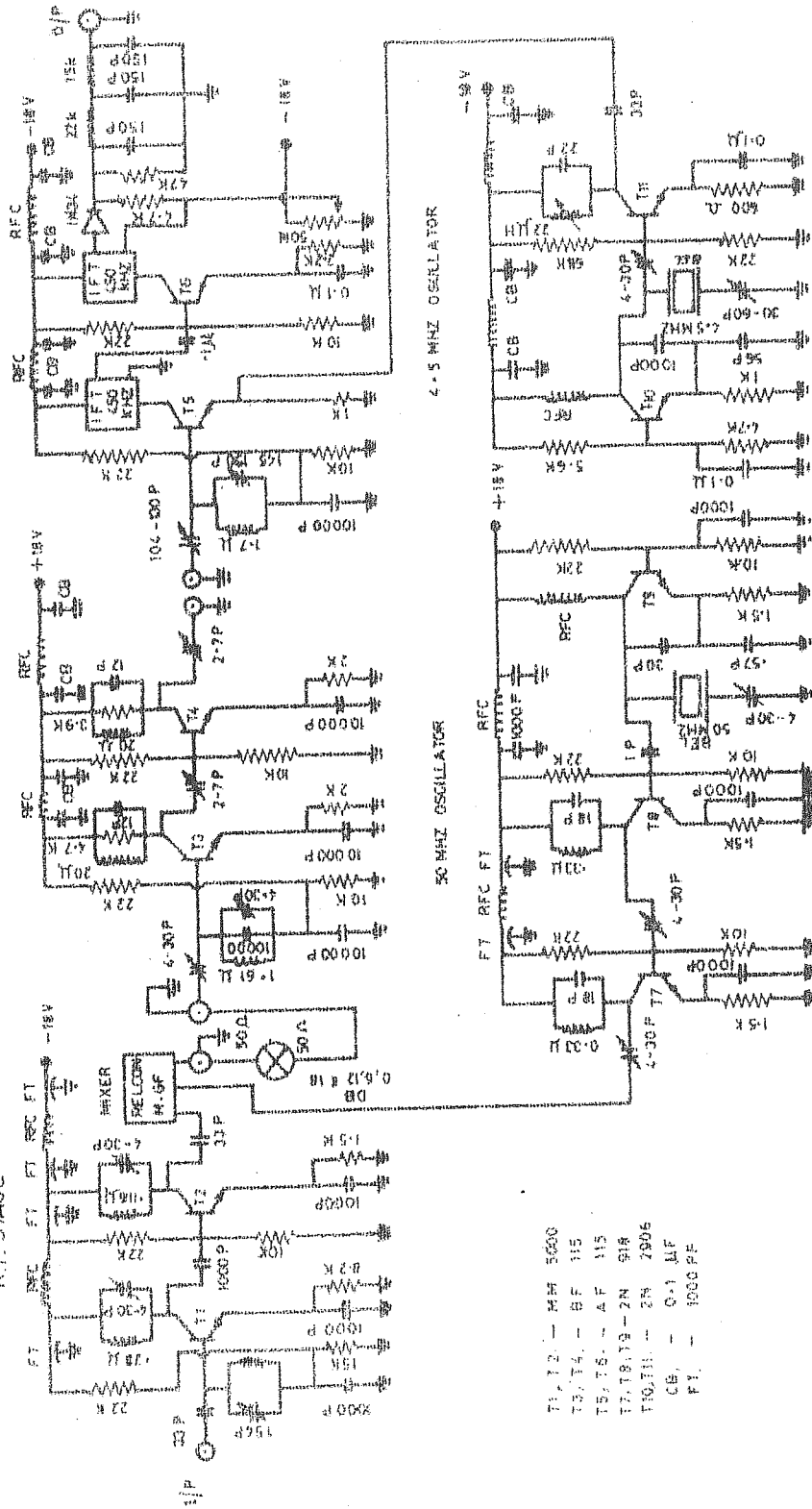
FIG. 2.11: SAMPLE AND HOLD CIRCUIT

# RX. SIGNAL AMPLITUDE RECORDING.

## SECOND I.F. STAGE & DETECTOR

## FIRST I.F. STAGE

## R.F. STAGE



- T1, T2 - 6X4
- T3, T4 - 6X4
- T5, T6 - 6X4
- T7, T8, T9 - 6X4
- T10, T11 - 6X4
- CB - 0.1 MF
- FT - 1000 PF

FIG. 2.12: RECEIVER 1: R.F., FIRST I.F., SECOND I.F. AND DETECTOR STAGES; AND 54.95 MHz OSCILLATOR

The R.F. amplifier consists of two common emitter tuned amplifier stages making use of low noise MM 5000 transistors. The first mixer used is a Relcom double balanced mixer which also gives very good isolation. The 50 MHz local oscillator is a crystal controlled one and is of colpitts type. This is followed by two stages of amplification and the 7 dbm output of these stages is fed to the Mixer. The I.F. amplifier has two stages making use of B.F. 115 transistors. The 4.5 MHz crystal oscillator output is fed to the emitter of the second mixer which makes use of an AF 115 transistor. The output of the second mixer which is at 450 KHz is amplified using one stage of AF 115 transistor. A commercially available intermediate frequency transformer (I.F.T.) is used in this stage, and the required bandwidth is obtained by shunting the primary of the I.F.T. This is followed by a diode detector and filter.

The receiver has an overall maximum gain of 118 dB which can be reduced in steps of 6 db if necessary. This attenuator is introduced between the first mixer and 4.95 MHz. I.F. amplifier so that the signal to noise ratio is not affected. The noise figure of the receiver is about 2.6 db and the bandwidth is 12 KHz.

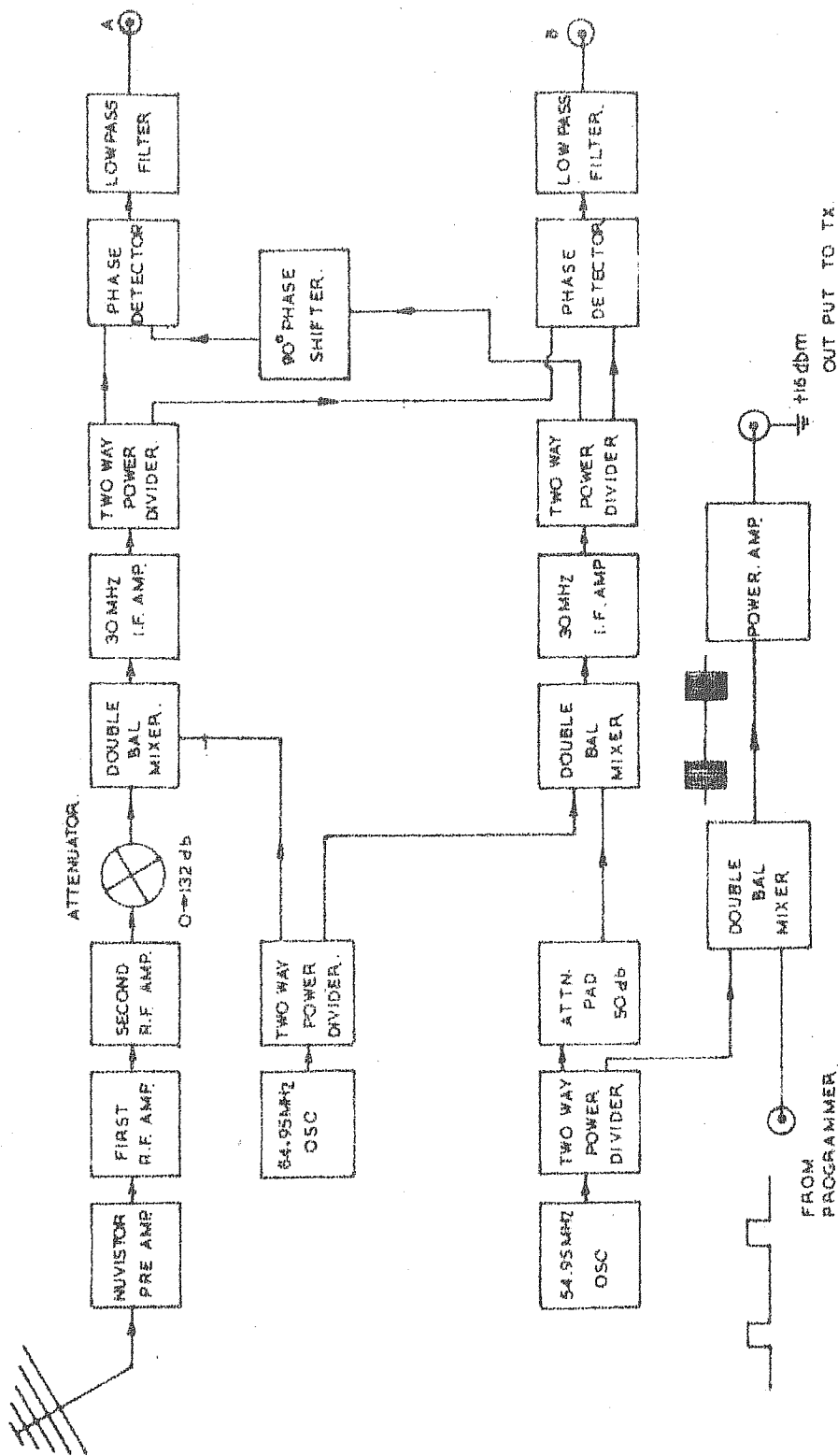
The power supplies of +18 and -18 volts are obtained using a series regulator.

(b) Receiver for spectral studies: (Receiver II)

Figure (2.13) represents schematically, the different stages employed in the receiver used for the study of spectral characteristics of the received echo.

The nuvistor (6CW4) preamplifier (figure 2.14) used has a noise figure of 3.5 db and a gain of 13 db. Noise figure of the first R.F. amplifier (figure 2.14) is 2.6 db and has a gain of 41 db. This consists of two amplifier stages making use of MM 5000 transistors. The second R.F. amplifier (figure 2.15) consists of 2 stages making use of 2N918 transistors and has a gain of 49 db. The 54.95 MHz signal at the output of the second R.F. stage is brought down to the required power level using a broad band 0-132 db attenuator variable in steps of 1 db and is mixed with 84.95MHz oscillator output using a double balanced mixer. The 0-132 db attenuator is used to adjust the power level at the input of the double balanced mixer to -43 dbm. The mixer stage is followed by two 30 MHz I.F. amplifier stages (figure 2.15) which bring the power level to +3 dbm. These amplifiers contain two stages making use of BF 115 transistors. A two way power divider, feeds the signal to two phase detectors. This forms the signal channel of the receiver used for spectral studies.

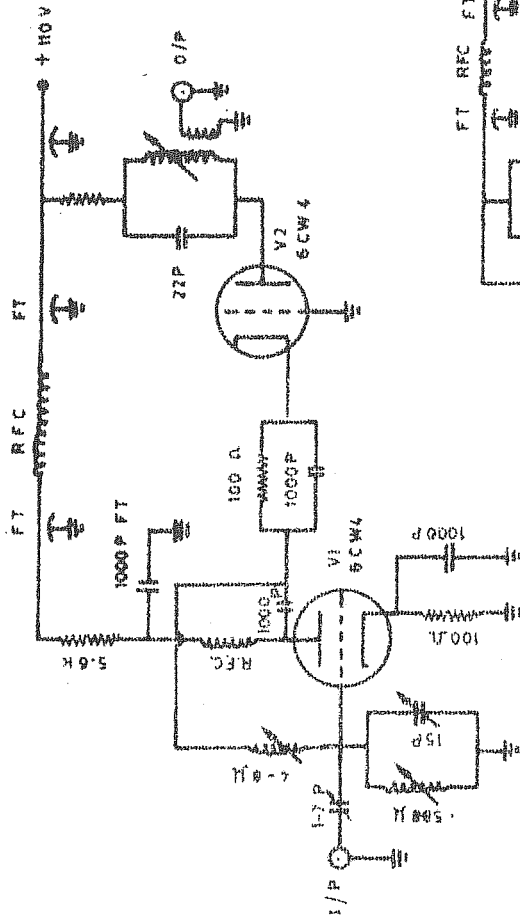




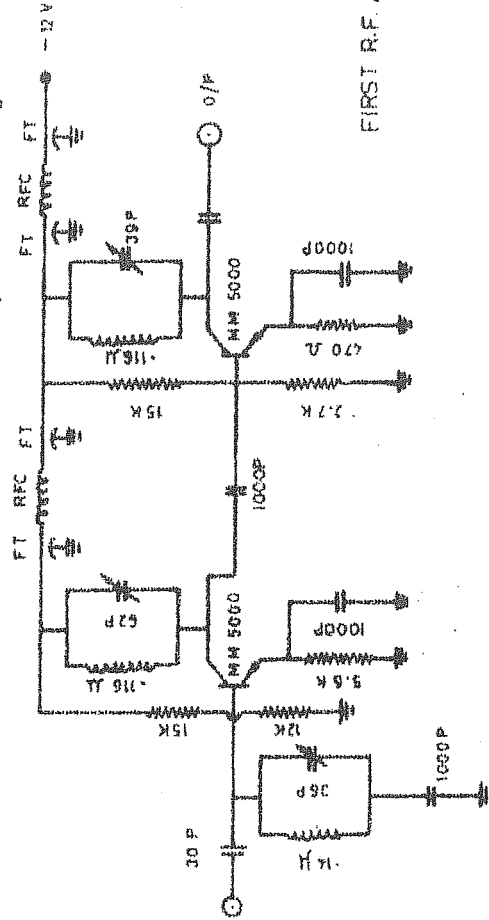
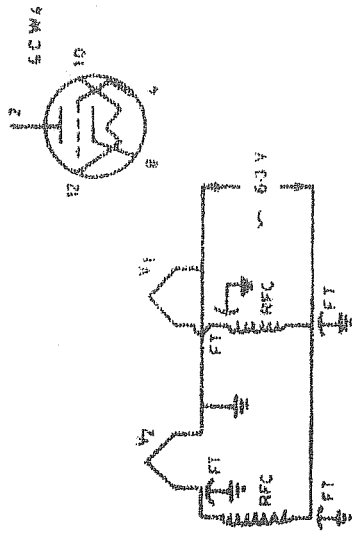
RECEIVER 2. - SPECTRAL STUDY.

FIG. 2.13: BLOCK DIAGRAM OF RECEIVER II

# PRE-AMPLIFIER



# FILAMENT CONNECTION



# FIRST R.F. AMPLIFIER

FT = 1000P

FIG. 2.14: RECEIVER II - PRE-AMPLIFIER AND FIRST R.F. AMPLIFIER

30 MHz 1. F AMPLIFIER (ONE SECTION)

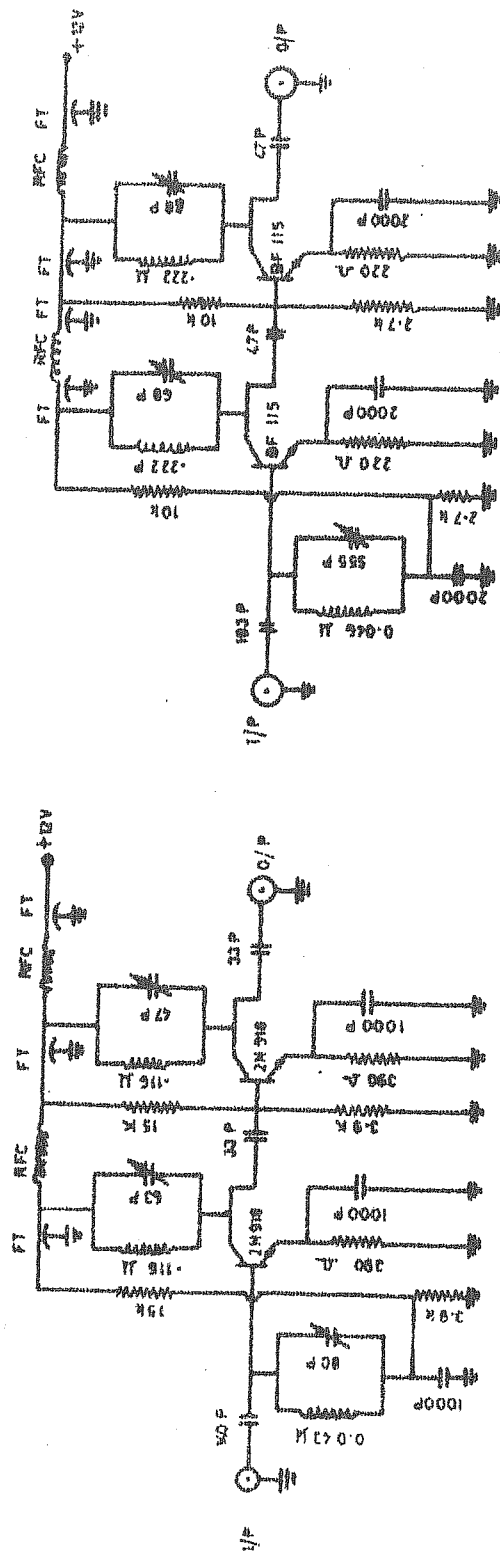


FIG. 2.15: RECEIVER I I. SECOND R.F. AMPLIFIER AND 30MHz I I. AMPLIFIER

An identical system is used to form the reference channel of the receiver. Instead of the received echo at 54.95 MHz, reference signal of 54.95 MHz at -43 dbm power level is fed to the double, balanced mixer, which is followed by the IF stages and a two way power divider. The 84.95 MHz crystal oscillator output, is fed to the double balanced mixers in the signal channel and the reference channel through a two way power divider.

One output from the signal channel and one from the reference channel are fed to a phase detector. The other two outputs of the signal and reference channels are fed to a second phase detector, with a  $90^\circ$  phase shift in the output from the reference channel. A  $\lambda/4$  RG 58/U cable is used to obtain the  $90^\circ$  phase shift. The outputs of the two phase detectors are passed through low pass filters (figure 2.03) with cut off at about 10 KHz. These low pass filters are active filters using operational amplifiers. The outputs of the filters, are fed to a spectrum analyser unit, for obtaining the doppler shift in the received echo.

#### 2.1.5 Spectrum analyser unit

The phase detected outputs from receiver II represent the real and imaginary parts of the complex voltage representing the frequency variation in the received echo. This complex voltage is spectral analysed using a McNamara system of double doppler shift analyser. Figure (2.16) shows how the outputs of Receiver II are

# SPECTRUM ANALYSER

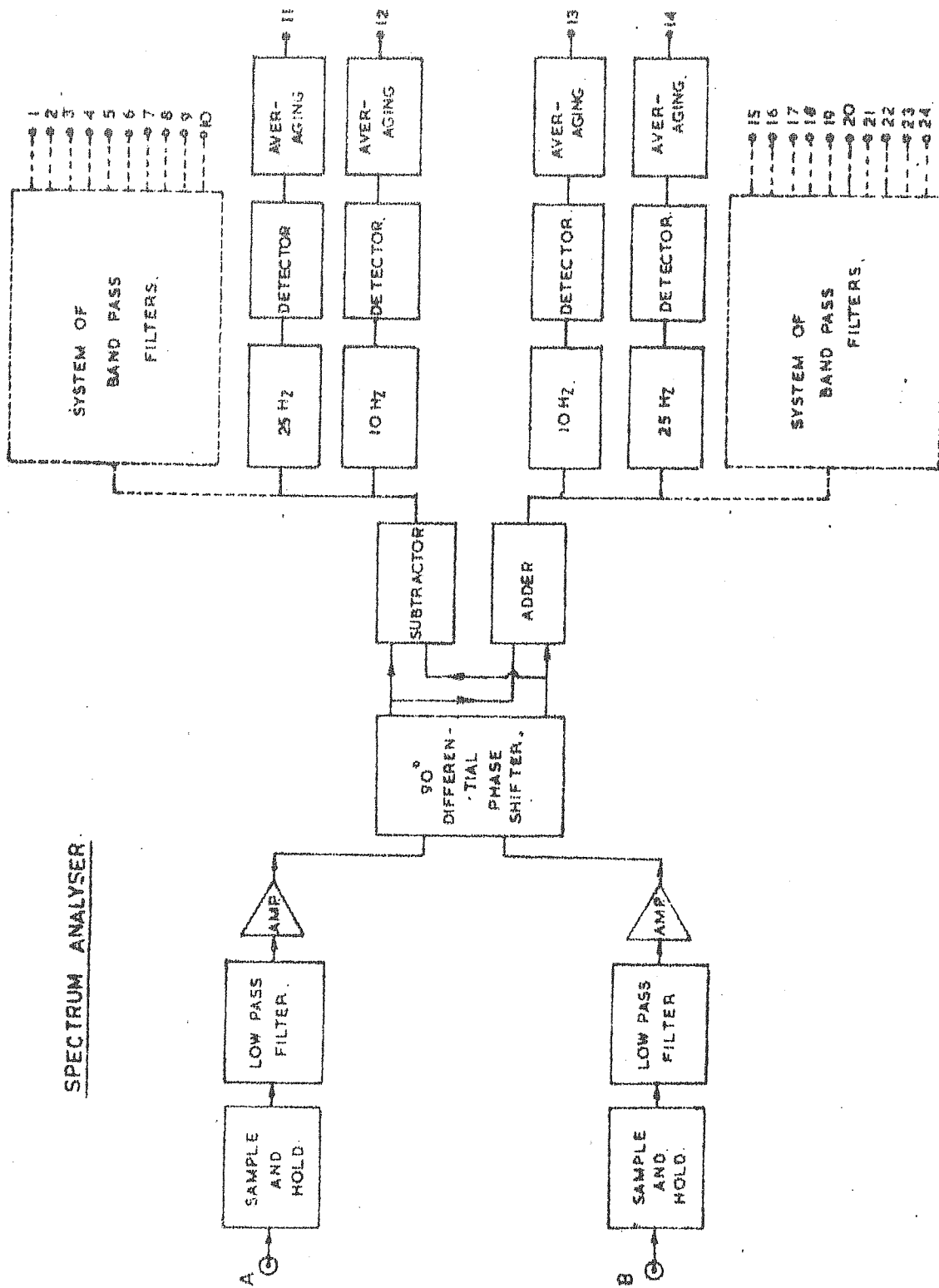
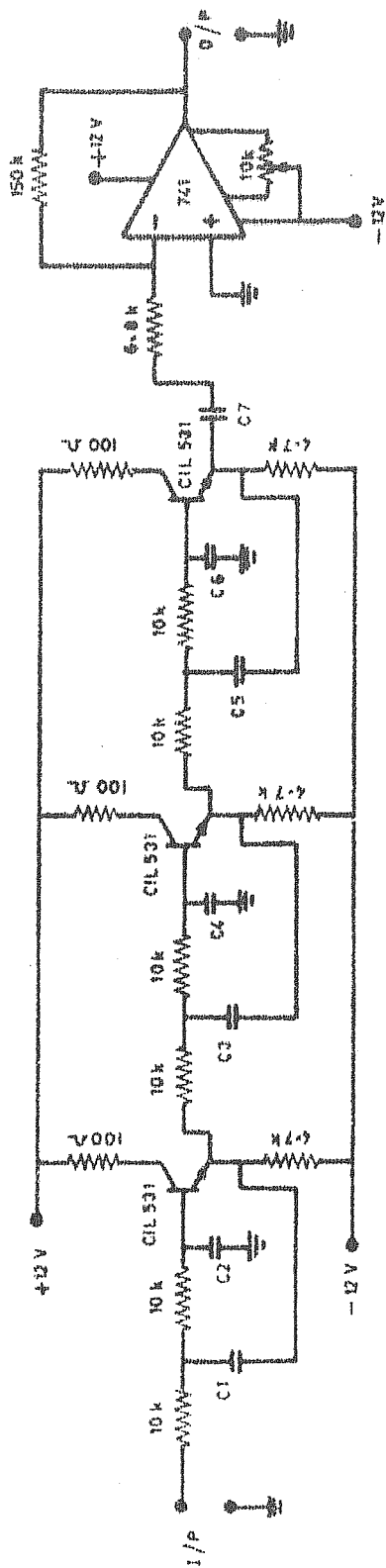


FIG. 2.16: BLOCK DIAGRAM OF SPECTRUM ANALYSER

processed to obtain the voltage spectrum. These outputs are sent through two channels which are identical up to the differential phase shifter stage.

Using height selection gates, with variable delay and width (the same as those used in the amplitude recording system) these signals are sampled and held (figure 2.11). The modulation in the signal which contains the required doppler shift information is separated from the high frequency carrier by passing through low pass filters with a cut off at 200 Hz. The outputs of the low pass filters are amplified to the required level using operational amplifiers (figure 2.17). The two amplified outputs thus obtained are fed to a  $90^\circ$  wide band differential phase shifter (figure 2.18) which has a frequency range of 9 Hz to 180 Hz with an estimated theoretical error of  $\pm 0.27$  degrees. A six pole network has been used for the purpose, and the unit has an insertion loss of 17.8 db. The two phase shifted outputs are fed to an add and subtract unit (figure 2.19 i). Operational amplifiers are used as adders and subtractors. This separates the upper and lower side bands, representing positive and negative doppler shifted components respectively. These outputs are fed to a system of 24 band pass filters (figure 2.19 ii) 12 on the positive side and 12 on the negative side. Each filter consists of an operational amplifier with a Twin - T network in the feedback circuit. The doppler spectrum of the received signal is represented by the 24 outputs of the filters taken in proper order.

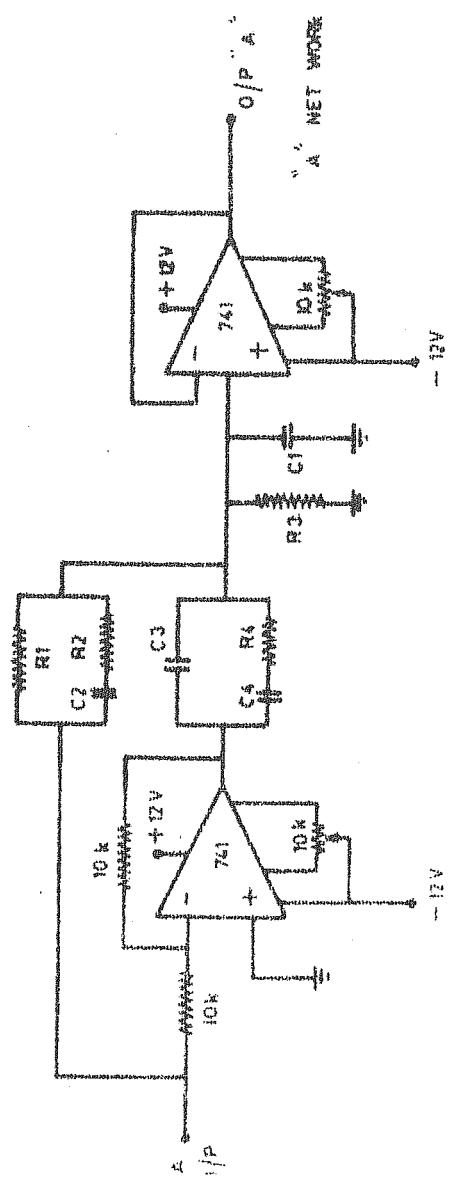
# LOW PASS FILTER AND AMPLIFIER CIRCUIT (ONE SECTION)



$C1 = C3 = 0.1 \mu F$   
 $C2 = C4 = C5 = C6 = 33000 pF$   
 $C7 = 100 \mu F$

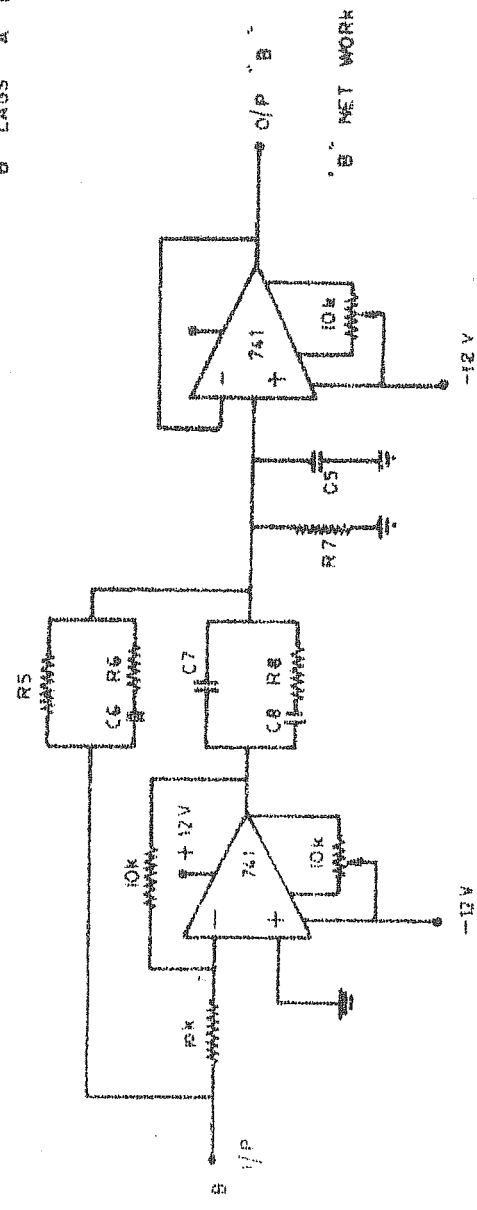
FIG. 2.17: LOW PASS FILTER AND AMPLIFIER - ONE SECTION

# BROAD BAND 90° PHASE SHIFTER



"A" LAGS "B" BY 90°

- R1 = 20K-842K
- R2 = 36-358K
- R3 = 60-0822K
- R4 = 58-9406K
- R5 = 1412-2617K
- R6 = 42-9546K
- R7 = 208-5619K
- R8 = 96-6064K



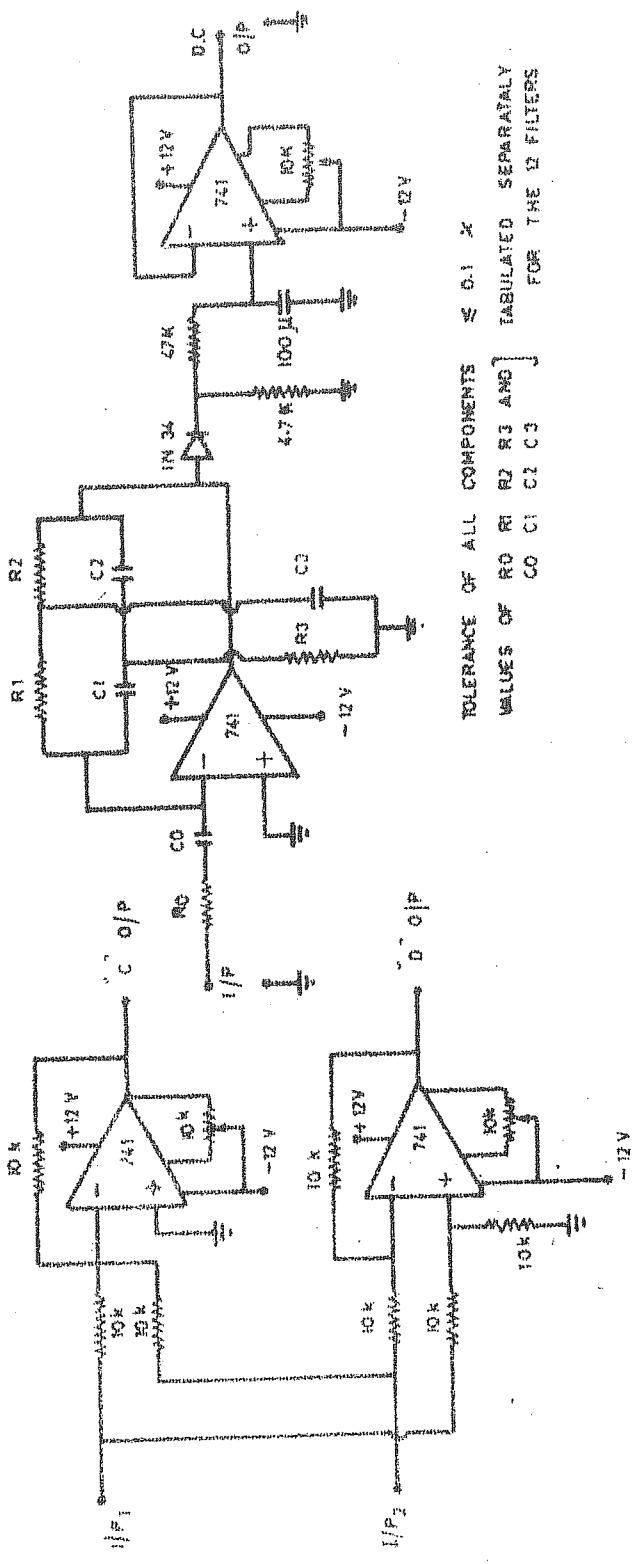
TOLERANCE OF ALL COMPONENTS  $\leq 0.1\%$

FIG. 2.18: 90° WIDEBAND DIFFERENTIAL PHASE SHIFTER



# ADD & SUBTRACT CIRCUIT

# BAND PASS FILTER CIRCUIT



TOLERANCE OF ALL COMPONENTS  $\leq 0.1\%$   
 TOLERANCE OF ALL RESISTORS  $\leq 1\%$   
 VALUES OF R0 R1 R2 R3 AND C0 C1 C2 C3 TABULATED SEPARATELY FOR THE 12 FILTERS

FIG. 2.19: (I) ADD AND SUBTRACT CIRCUIT  
 (II) BAND PASS FILTER

	IN K $\Omega$				IN PF			
FREQ.	R <sub>0</sub>	R <sub>1</sub>	R <sub>2</sub>	R <sub>3</sub>	C <sub>0</sub>	C <sub>1</sub>	C <sub>2</sub>	C <sub>3</sub>
10 CPS.	50.0001	816.3279	183.6725	209.9117	312.310	194.96	86.651	758.20
25	125.0001	795.7571	204.2432	188.5323	509.30	80.00	311.70	337.67
40	200.0002	795.4558	204.5443	178.9764	198.94	50.02	194.52	222.31
55	275.0000	796.0398	203.9605	174.1686	105.23	36.35	141.88	166.15
70	350.0000	796.5872	203.4132	171.2954	64.96	28.54	111.77	132.73
85	425.0002	797.0269	202.9736	169.3882	44.06	23.49	92.25	110.54
100	500.0002	797.3740	202.6263	168.0316	31.83	19.96	78.55	94.72
115	575.0002	797.6536	202.3467	167.0163	24.07	17.35	68.40	82.86
130	650.0005	797.8806	202.1197	166.2293	18.83	15.34	60.57	73.65
145	725.0005	798.0688	201.9315	165.6007	15.14	13.75	54.36	66.28
160	800.0010	798.2275	201.7729	165.0870	12.43	12.46	49.30	60.25
175	875.0007	798.3618	201.6386	164.6599	10.39	11.39	45.10	55.23

COMPONENT VALUES FOR BAND PASS FILTERS

### 2.1.6 Recording units

#### (a) Amplitude recording system

A block diagram of the amplitude recording system is shown in figure (2.20). The delay of the sampling pulse is adjusted so that the peak of the received signal coincides with the trailing edge of the sampling pulse. Though there exists provision for three gate pulses with independently adjustable delays and widths so that up to three different height ranges can be studied simultaneously, only one is used for the present purpose. The sample and hold circuit (figure 2.11) essentially consists of an FET, which passes the signal to its output only during the sampling period. A capacitor across the output terminals gets charged to the signal level corresponding to the trailing edge of the sampling pulse and retains the charge till the next pulse arrives. At the arrival of the next sampling pulse, the FET becomes conducting and offers an easy discharge path to the capacitor, and the capacitor gets charged to the new signal level. The output of the sample and hold circuit is averaged (time constant is 1 sec) and fed to a strip chart recorder. The averaging circuit is shown in figure (2.24).

AMPLITUDE RECORDING SYSTEM

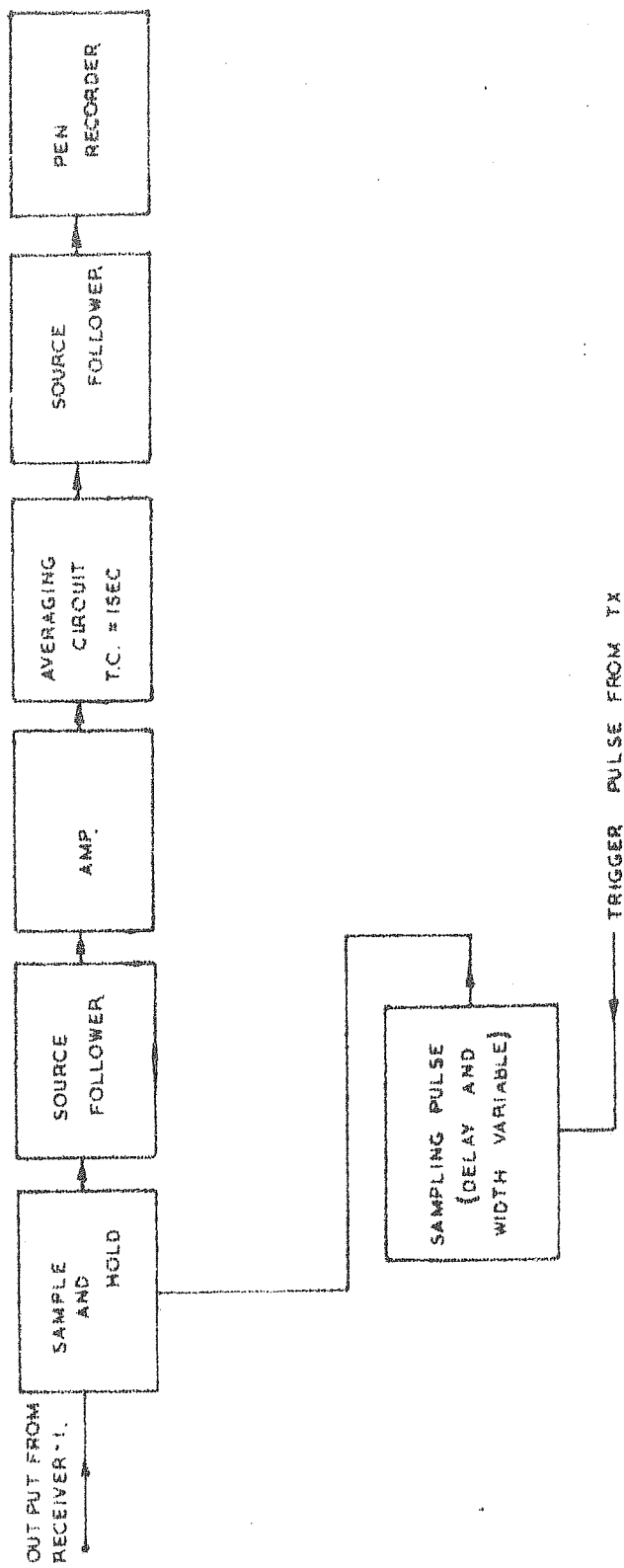


FIG. 2.20: BLOCK DIAGRAM OF AMPLITUDE RECORDING SYSTEM

(b) Spectral display and recording

The outputs of the bandpass filters in the spectrum analyser unit, are detected and averaged (time constant 4-5 seconds) and the resulting d.c. outputs are multiplexed and fed to an oscilloscope for display. The multiplexer used for this purpose is shown in figures (2.21, 2.22 and 2.23). The displayed frequency voltage spectrum is photographed with a camera attached to the oscilloscope screen. This spectrum is later used to obtain the doppler power spectra. The procedure for this is explained in section (2.3) of this thesis.

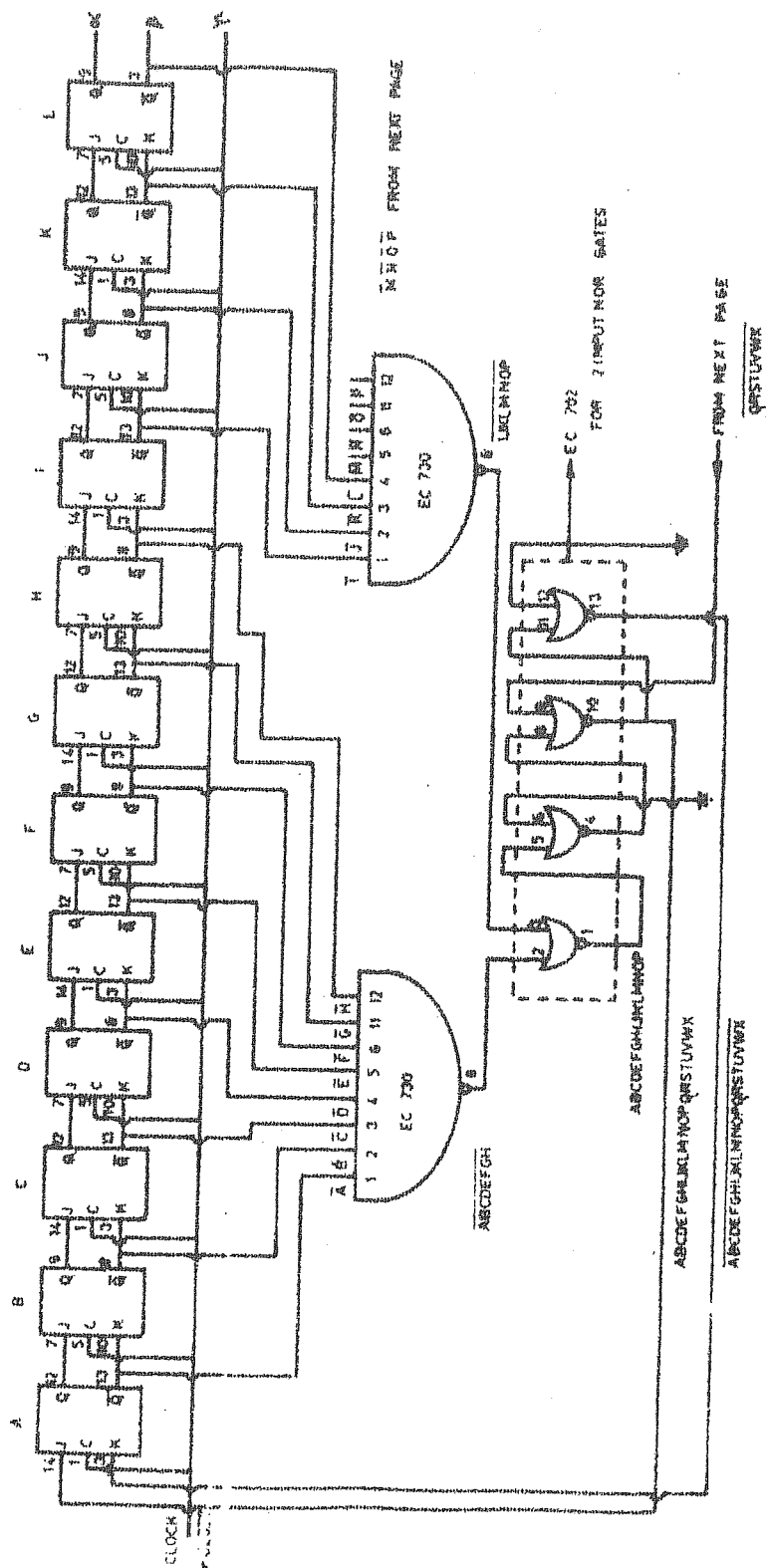
2.1.7 Antenna systems

Two sets of antenna arrays were used during the present studies. Each set contained two identical arrays, one for transmission of the radar signal, and the other for reception. Each array could be operated in vertical or oblique transmission (or reception) mode. The oblique transmission mode was obtained by introducing additional phaser cables at the feeding points of the different antennas in the arrays.

(a) Yagi array

Each yagi antenna in the array consists of a folded dipole which is the driving element, three directors and a reflector. The elements are in the north-south direction. Figure (2.25) is a schematic representation of the yagi array. Two rows of four yagi antennas each are spread in the east-west direction. The transmitting and

MULTIPLEXER - [24] STAGE RING COUNTER (1 PAGE)



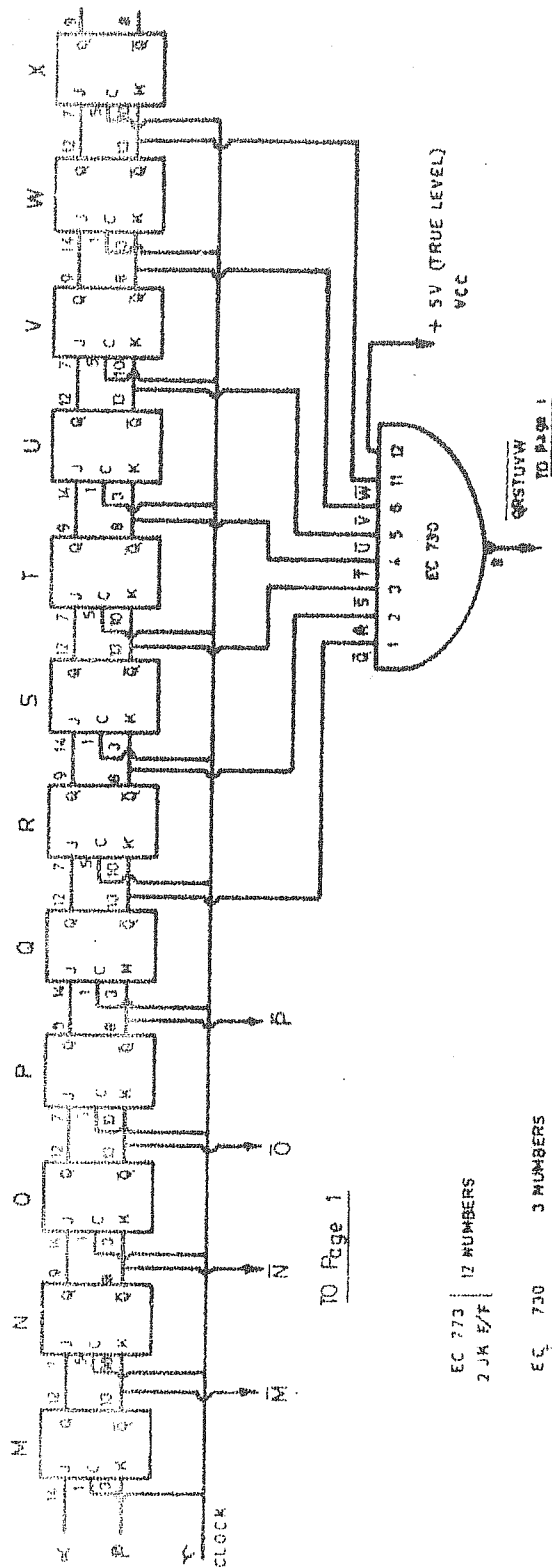
2000 年 1 月 2 日

世宗

5  
 6  
 7  
 8  
 9  
 10  
 11  
 12  
 13  
 14  
 15  
 16  
 17  
 18  
 19  
 20  
 21  
 22  
 23  
 24  
 25  
 26  
 27  
 28  
 29  
 30  
 31  
 32  
 33  
 34  
 35  
 36  
 37  
 38  
 39  
 40  
 41  
 42  
 43  
 44  
 45  
 46  
 47  
 48  
 49  
 50  
 51  
 52  
 53  
 54  
 55  
 56  
 57  
 58  
 59  
 60  
 61  
 62  
 63  
 64  
 65  
 66  
 67  
 68  
 69  
 70  
 71  
 72  
 73  
 74  
 75  
 76  
 77  
 78  
 79  
 80  
 81  
 82  
 83  
 84  
 85  
 86  
 87  
 88  
 89  
 90  
 91  
 92  
 93  
 94  
 95  
 96  
 97  
 98  
 99  
 100  
 101  
 102  
 103  
 104  
 105  
 106  
 107  
 108  
 109  
 110  
 111  
 112  
 113  
 114  
 115  
 116  
 117  
 118  
 119  
 120  
 121  
 122  
 123  
 124  
 125  
 126  
 127  
 128  
 129  
 130  
 131  
 132  
 133  
 134  
 135  
 136  
 137  
 138  
 139  
 140  
 141  
 142  
 143  
 144  
 145  
 146  
 147  
 148  
 149  
 150  
 151  
 152  
 153  
 154  
 155  
 156  
 157  
 158  
 159  
 160  
 161  
 162  
 163  
 164  
 165  
 166  
 167  
 168  
 169  
 170  
 171  
 172  
 173  
 174  
 175  
 176  
 177  
 178  
 179  
 180  
 181  
 182  
 183  
 184  
 185  
 186  
 187  
 188  
 189  
 190  
 191  
 192  
 193  
 194  
 195  
 196  
 197  
 198  
 199  
 200  
 201  
 202  
 203  
 204  
 205  
 206  
 207  
 208  
 209  
 210  
 211  
 212  
 213  
 214  
 215  
 216  
 217  
 218  
 219  
 220  
 221  
 222  
 223  
 224  
 225  
 226  
 227  
 228  
 229  
 230  
 231  
 232  
 233  
 234  
 235  
 236  
 237  
 238  
 239  
 240  
 241  
 242  
 243  
 244  
 245  
 246  
 247  
 248  
 249  
 250  
 251  
 252  
 253  
 254  
 255  
 256  
 257  
 258  
 259  
 260  
 261  
 262  
 263  
 264  
 265  
 266  
 267  
 268  
 269  
 270  
 271  
 272  
 273  
 274  
 275  
 276  
 277  
 278  
 279  
 280  
 281  
 282  
 283  
 284  
 285  
 286  
 287  
 288  
 289  
 290  
 291  
 292  
 293  
 294  
 295  
 296  
 297  
 298  
 299  
 300  
 301  
 302  
 303  
 304  
 305  
 306  
 307  
 308  
 309  
 310  
 311  
 312  
 313  
 314  
 315  
 316  
 317  
 318  
 319  
 320  
 321  
 322  
 323  
 324  
 325  
 326  
 327  
 328  
 329  
 330  
 331  
 332  
 333  
 334  
 335  
 336  
 337  
 338  
 339  
 340  
 341  
 342  
 343  
 344  
 345  
 346  
 347  
 348  
 349  
 350  
 351  
 352  
 353  
 354  
 355  
 356  
 357  
 358  
 359  
 360  
 361  
 362  
 363  
 364  
 365  
 366  
 367  
 368  
 369  
 370  
 371  
 372  
 373  
 374  
 375  
 376  
 377  
 378  
 379  
 380  
 381  
 382  
 383  
 384  
 385  
 386  
 387  
 388  
 389  
 390  
 391  
 392  
 393  
 394  
 395  
 396  
 397  
 398  
 399  
 400  
 401  
 402  
 403  
 404  
 405  
 406  
 407  
 408  
 409  
 410  
 411  
 412  
 413  
 414  
 415  
 416  
 417  
 418  
 419  
 420  
 421  
 422  
 423  
 424  
 425  
 426  
 427  
 428  
 429  
 430  
 431  
 432  
 433  
 434  
 435  
 436  
 437  
 438  
 439  
 440  
 441  
 442  
 443  
 444  
 445  
 446  
 447  
 448  
 449  
 450  
 451  
 452  
 453  
 454  
 455  
 456  
 457  
 458  
 459  
 460  
 461  
 462  
 463  
 464  
 465  
 466  
 467  
 468  
 469  
 470  
 471  
 472  
 473  
 474  
 475  
 476  
 477  
 478  
 479  
 480  
 481  
 482  
 483  
 484  
 485  
 486  
 487  
 488  
 489  
 490  
 491  
 492  
 493  
 494  
 495  
 496  
 497  
 498  
 499  
 500  
 501  
 502  
 503  
 504  
 505  
 506  
 507  
 508  
 509  
 510  
 511  
 512  
 513  
 514  
 515  
 516  
 517  
 518  
 519  
 520  
 521  
 522  
 523  
 524  
 525  
 526  
 527  
 528

# MULTIPLEXER 24 STAGE RING COUNTER

II Page



TO Page 1

EC 773 12 NUMBERS  
2 JK F/F

EC 730 3 NUMBERS  
EC - 702 1 CHIP

EC 773 EC 730 EC 702

VCC  
GROUND

PIN 4  
PIN 11

14  
7

24 OUTPUTS ARE TAKEN AT THE 24 Q  
POINTS OF THE F/F'S Q/P TO THE GATE  
O/P TO THE GATE SWITCHES

FIG. 2.22: MULTIPLEXER UNIT - II

MULTIPLEXER - ONE OF THE 24 SWITCHES

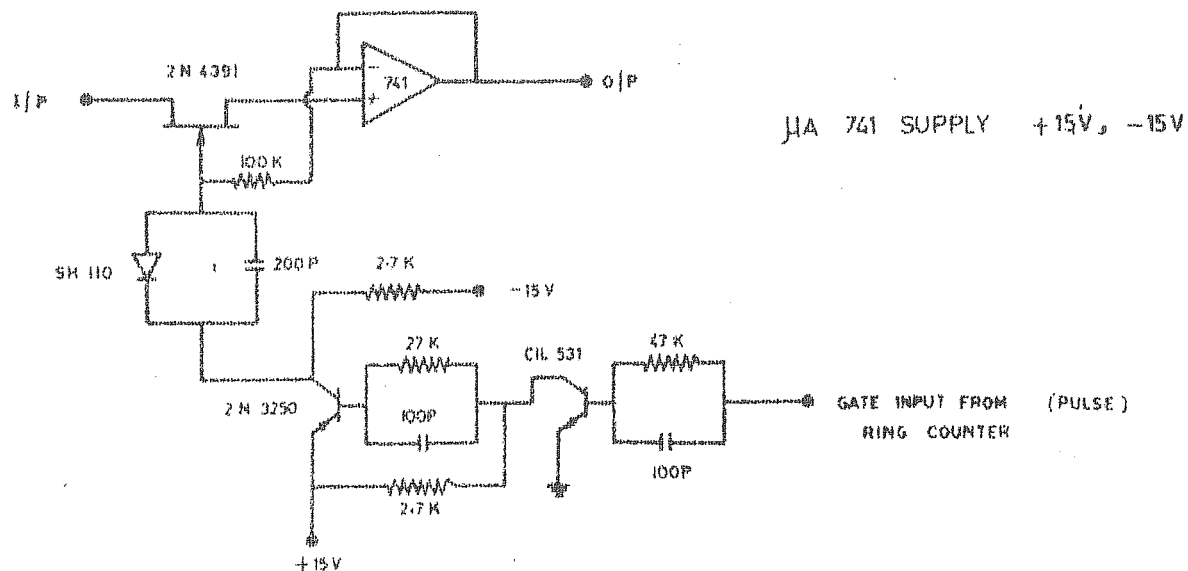


FIG. 2.23: MULTIPLEXER UNIT - III

SIGNAL STRENGTH RECORDING CIRCUIT.

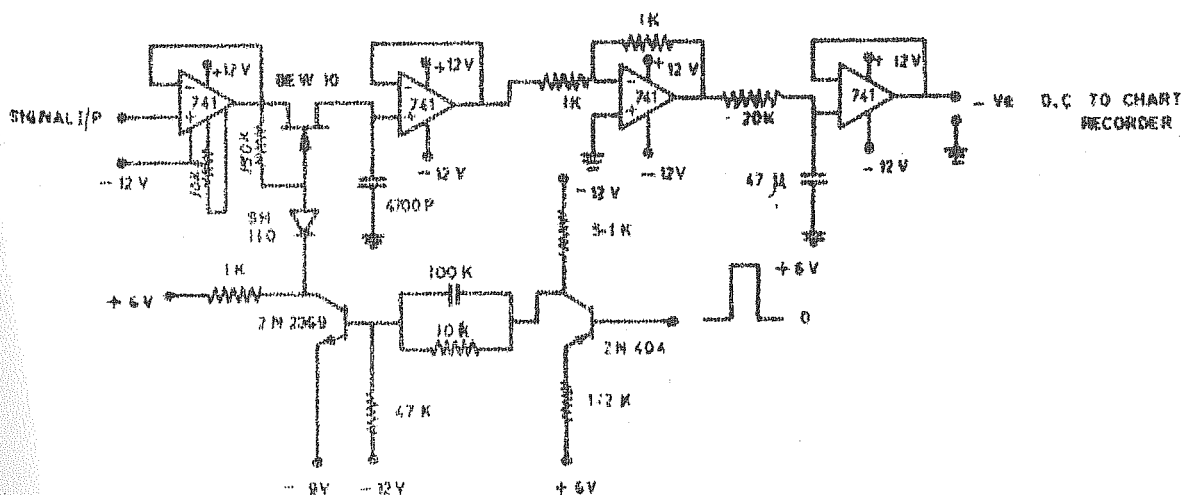


FIG. 2,24: AMPLITUDE RECORDING CIRCUIT



# ANTENNA ARRAYS

## 1. YAGI - ARRAY

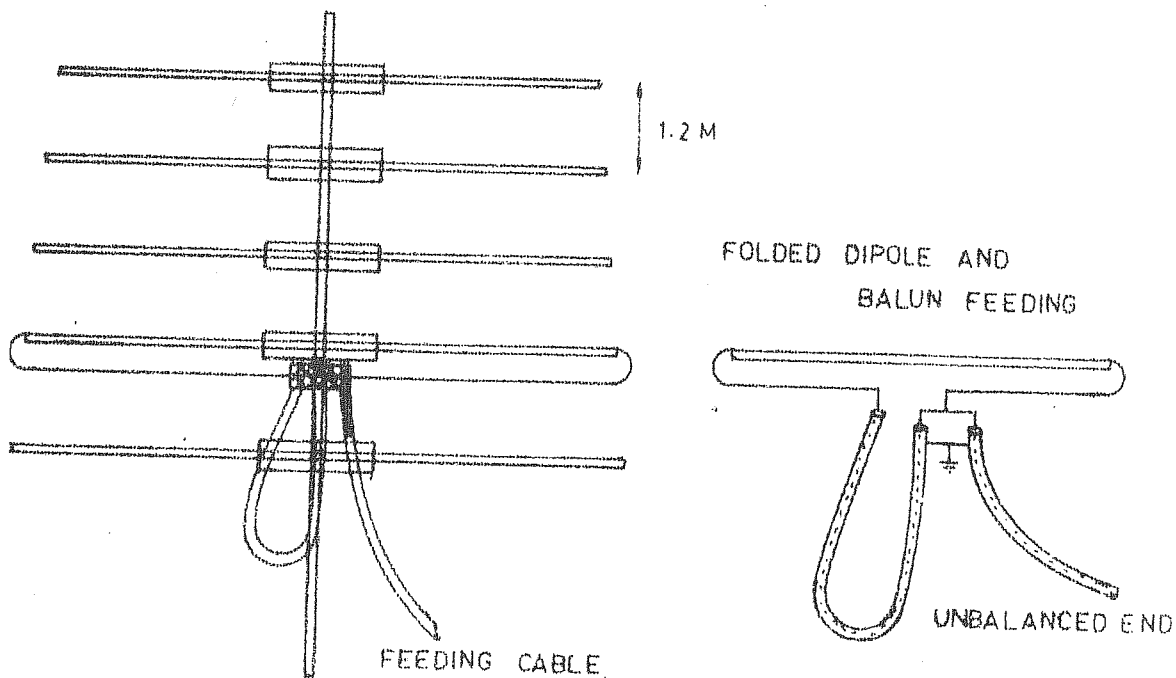
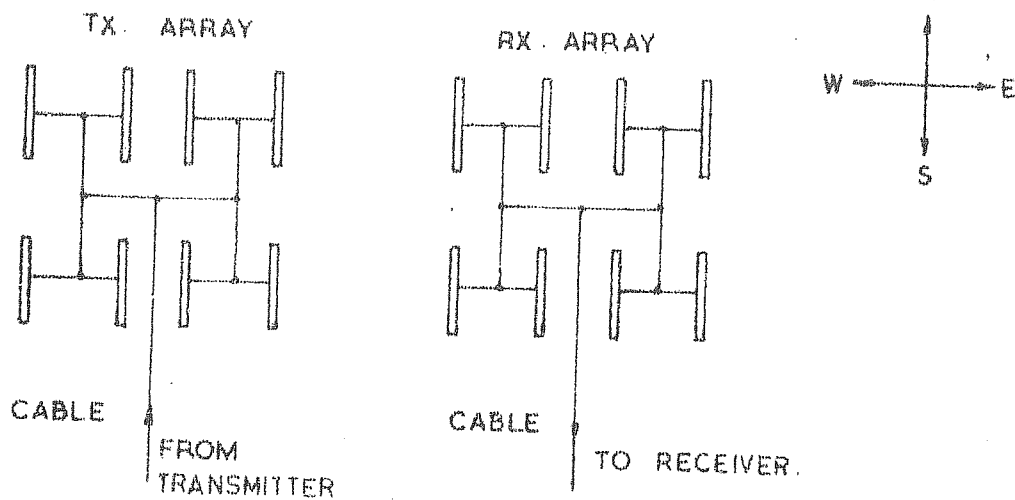


FIG. 2.25: ANTENNA SYSTEM: 1 - YAGI ARRAY WITH BALUN FEEDING

receiving arrays are separated by a distance of about 4 to 5 wavelengths to reduce the leakage of 54.95 MHz signal during the receiving mode. This configuration of the array gives a narrow beam in the east-west plane.

The impedance of the arrays is adjusted to be  $52\ \Omega$ . The array has a gain of about 18 db over an isotropic radiator, and beamwidth in the H and E planes are about  $15^\circ$  and  $20^\circ$  respectively. The beam is polarised in the north-south plane.

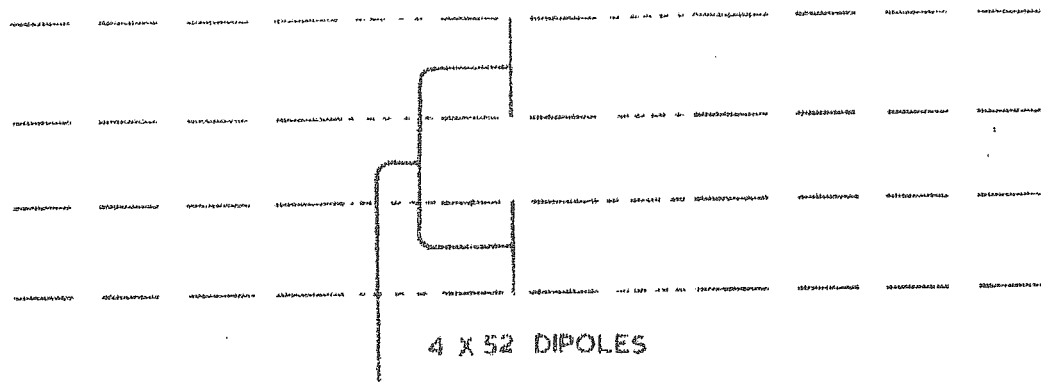
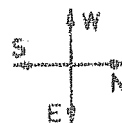
The method of feeding and receiving the signal is shown schematically in figure (2.25). A balun (balanced to unbalanced converter) converts the balanced  $52\ \Omega$  impedance of the antenna into an unbalanced  $52\ \Omega$  impedance at the feeding and receiving points.

The beam of the antenna in the usual mode of operation is vertical. It can be made oblique, by adding additional phaser cables at the feeding points of the different antennas in an array.

#### (b) Dipole array

This array was set up with the joint efforts of NOAA scientists (Boulder, Colorado) and Space Physics Division (SSTC, Trivandrum, India). This consists of 208 dipoles in the geometry of  $52 \times 4$  dipoles (52 dipoles in one row spread in the north-south direction with four such rows in the east-west direction. Similar arrays are used for transmission and reception. The dipole elements are made of RG 8 A/U coaxial cables. The array is shown schematically in figure (2.26).

## 2. DIPOLE ARRAY



FEEDING OR RECEIVING END

IDENTICAL ARRAYS ARE USED FOR TRANSMISSION  
AND RECEPTION

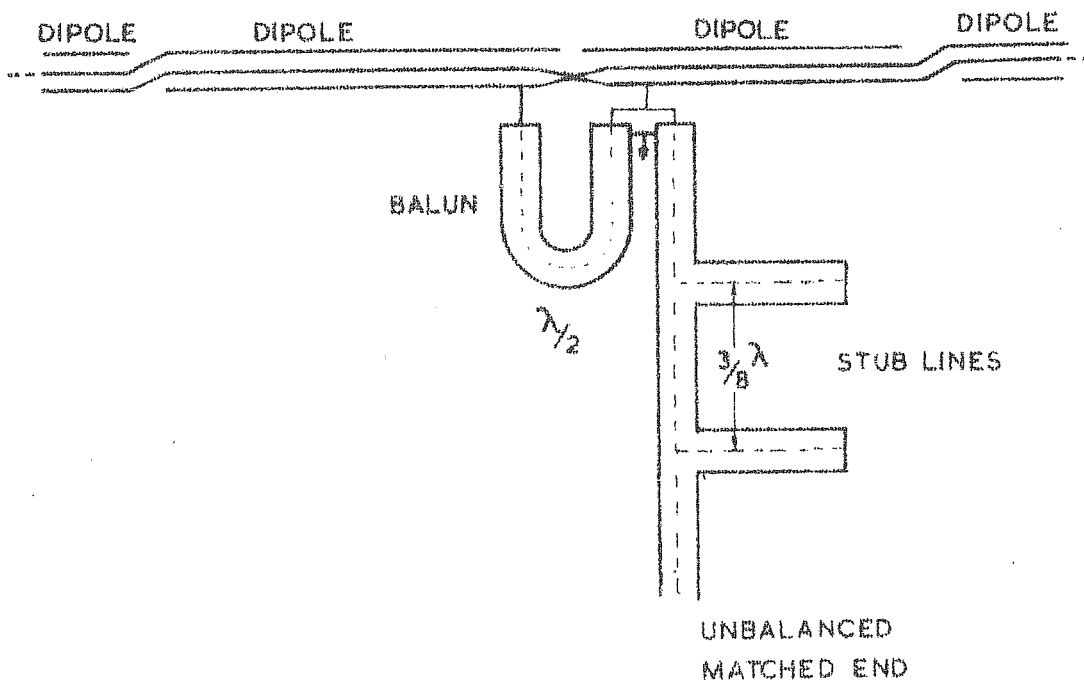


FIG. 2.26: ANTENNA SYSTEM: 2 - DIPOLE ARRAY WITH  
STUBLINE MATCHING AND BALUN FEEDING

The impedance of the array is adjusted to be  $52 \Omega$  by a stub line matching device. The balanced impedance is converted into unbalanced one using baluns at the feeding (or receiving) points of the array. The method of feeding is shown in the figure (2.26). The array has a beam width of about  $3^\circ$  in the E plane and  $27^\circ$  in the H plane. The dipole elements being spread in the north-south direction, a wider beam in the east-west plane is obtained. A gain of 25 db over an isotropic radiator is estimated for this array. The beam is polarised in the north-south plane.

Like the Yagi array, the beam of the dipole array can be made oblique by using necessary additional phaser cables at the feeding and receiving points.

For the present studies both the yagi and dipole arrays were used, and were operated both in vertical and oblique (first at  $45^\circ W$  and later at  $30^\circ W$  from vertical) modes.

#### 2.1.8 Calibration of the amplitude receiver

The linearity of the amplitude receiver is tested using a calibration network (figure 2.10). A part of the 54.95 MHz signal from the programmer unit, is fed at the input of the amplitude receiver through an attenuator. The output of the receiver, recorded on the strip chart recorder, for known voltage inputs to the receiver is noted. By changing the attenuation the linearity of the receiver is tested. This frequent check, is intended to eliminate the inaccuracies in the results, that can arise due to any possible non-linearity in the receiver.

## 2.2 In-situ measurements of J and ne

### 2.2.1 Measurement of J:

Proton precession magnetometers used for the measurement of the total magnetic field during the reported flights were miniaturised rugged versions of packard and varian type (Cahill et al. 1956). The magnetometer consists of the sensor, a programming multivibrator, the cycling relay, polarising power supply and the main high gain amplifiers (Sastry, 1964).

The total intensity of magnetic field  $F$  is measured using the proton precession magnetometer. A proper theoretically predicted base value (in the absence of electrojet currents) is selected and the depatures  $\Delta F$  of the measured field from this base value is calculated.  $\Delta F$  values are plotted against altitude to obtain the "difference curves". The current density profiles are derived from the slopes of these difference curves, under certain assumptions regarding the nature and extent of the electrojet currents. The effect of the currents induced in the conducting earth is also taken into account during this conversion. Current density  $J$  in  $\text{amps}/\text{km}^2$  is calculated using the formula (Sastry 1970).

$$J(h) = \frac{10}{4\pi} (\Delta F_{h_1} - \Delta F_{h_2}) / (h_2 - h_1) \text{ Amps}/\text{km}^2$$

where  $\Delta F_{h_1}$  and  $\Delta F_{h_2}$  refer to  $\Delta F$  values at altitudes  $h_1$  and  $h_2$  close to each other, and are obtained from the "difference curve" in gammas.

$h = \frac{h_1 + h_2}{2}$  is the mean height in kms. where the current density is  $J(h)$ .

### 2.2.2 Measurement of $n_e$ .

Laboratory methods of measuring electron densities using Langmuir probes have been extended to the measurement of electron densities at the ionospheric levels with the advent of rocket studies a couple of decades ago. Since then various forms of Langmuir probes have been used for the measurements. Langmuir probe systems distinct from the conventional ones (Smith 1964) were used during the experiments reported here (Prakash and Subbaraya, 1967). This is functionally similar to the Smith system, but has many practical advantages over the same. It is much simpler, uses a single floating power supply; reduces leakage currents within the system to a minimum, and facilitates the use of a guard ring electrode without any additional electronics. An electrometer amplifier converts the sensor current into an analog voltage which is telemetered and recorded at ground stations.

The probe current profiles thus obtained are converted into electron density profiles using conversion factors obtained from other experiments which measure the absolute values of the electron density. Usually ionograms are used for this purpose.

### 2.3 Data reduction

#### 2.3.1 Correction of spectra for filter characteristics

The photograph of the radar spectrum represents the output voltages of the system of band pass filters. The characteristics of the filters modify the actual spectrum and what is observed is only the convolution of the actual spectrum by the filter characteristics. Knowing the filter characteristics one can compute the actual spectrum from the observed one to a certain degree of accuracy.

Let  $g_{ij}$  represents the transmission factor of the filter at the  $j$ th frequency. If  $V_{oi}$  is the actual output at the  $i$ th frequency and  $V_i$  is the output as observed from the spectral photograph, then one can have the approximate relation

$$\begin{bmatrix} V_i^2 \end{bmatrix} = \begin{bmatrix} V_{oi}^2 \end{bmatrix} \begin{bmatrix} g_{ij}^2 \end{bmatrix}$$

In the present case there are 12 filters and  $g_{ij}$  hence is a  $12 \times 12$  matrix,  $V_{oi}$  is a column matrix of 12 elements, which are to be computed, and  $V_i$  is a column matrix with 12 elements that are known. The  $g_{ij}^2$  values are normalised such that

$$\sum_j g_{ij}^2 = 1$$

So  $V_{oi}$  values can be obtained by multiplying the inverse of the matrix  $(g_{ij}^2)$  by the matrix  $(V_i^2)$ . The  $(V_{oi}^2)$  value thus obtained is a measure of the power at the  $i$ th frequency.

By feeding known voltages at known frequencies and observing the outputs of the bandpass filters, one can compute the  $g_{ij}$  values which can later be normalised according to the condition stated above.

### 2.3.2 Doppler spectrum and the velocity spectrum

The power spectrum of the radar echo represents the probability of velocity distribution in the electron density irregularities (section 1.2.3). The peak of the spectrum corresponds to the most probable velocity of these irregularities. A doppler shift  $\delta f$  in the spectrum corresponds to a velocity  $V_d$  of the irregularities in the direction of observation and is given by

$$V_d = - (c / 2 f_0) \delta f$$

where  $f_0$  is the transmitted frequency, and  $c$  is the velocity of electromagnetic waves. The velocity  $V_d$  is taken to be positive in the direction of transmission. The negative sign in the above equation shows that when  $V_d$  is positive  $\delta f$  is negative.

For oblique transmission, (radar beam at an angle with the vertical) the velocity computed from the power spectrum  $V_{obs}$  is to be modified to obtain the horizontal velocity of the irregularities. If one assumes that the motion of irregularities is only in the horizontal direction most of the time (a well accepted assumption), then these two velocities, are related by the equation.

$$V_{obs} = V_d \sin \theta, \text{ and hence } V_d \text{ can be computed.}$$



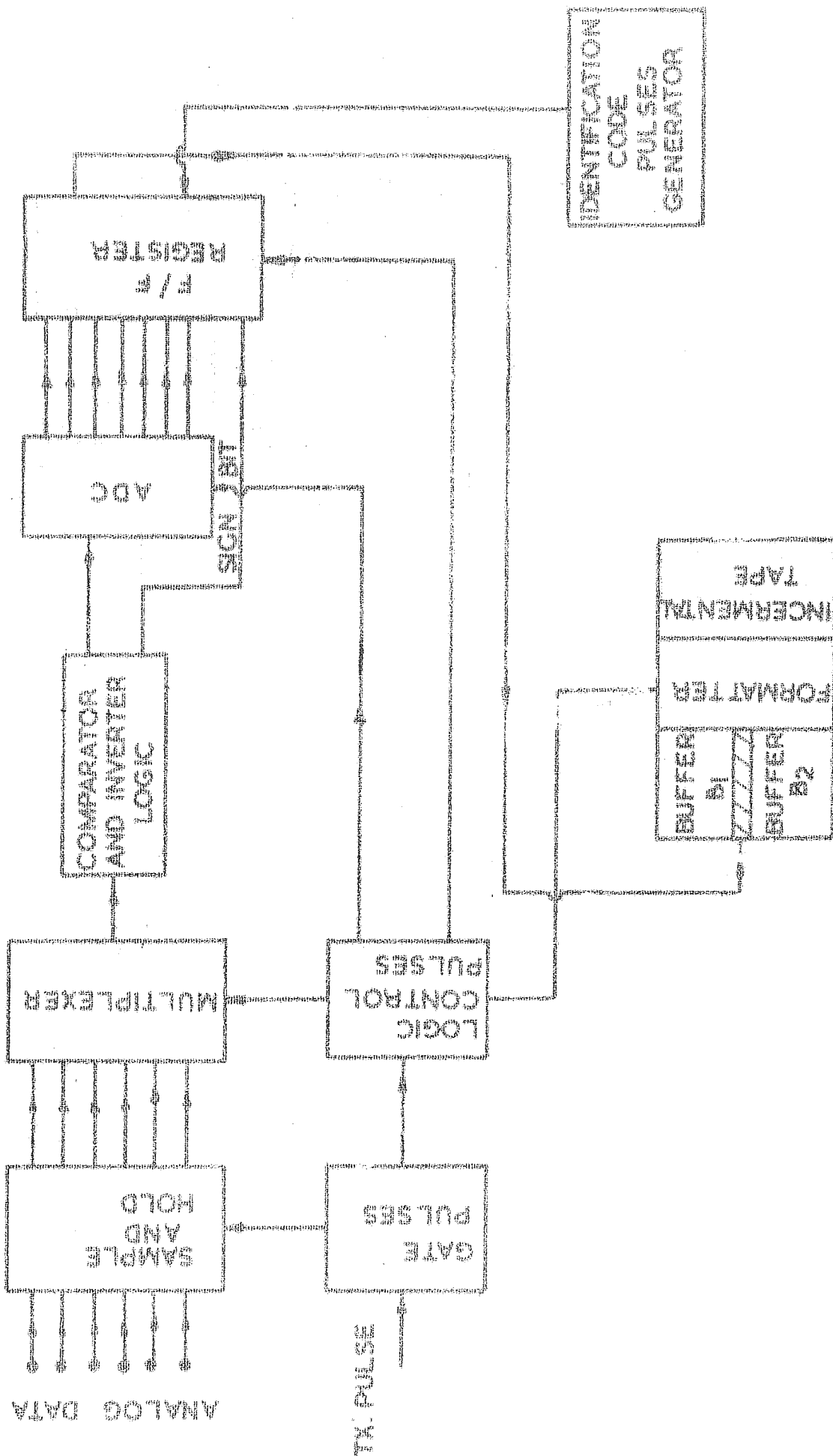
## 2.4 Digital data processing

There are many disadvantages associated with this method of analog data processing. The finite number of filters limits the number of spectral points to a very low value, thus affecting the frequency resolution. Though corrections can be applied to the frequency characteristics of the filters, the errors involved in the correction also puts a limit to the accuracy of the results obtained. The fading in the amplitude of the signal when is of the order of doppler shift associated with the spectra affect the accuracy of measurements. The fading rate, to some extent, can be identified from symmetric effect on both positive and negative sides of the spectra and can be corrected for. In order to obtain results to a better accuracy a digital data processing unit has been designed and will be operative in the near future for the radar studies.

The outputs of Receiver II, from different height ranges are multiplexed and converted into series outputs which are fed to a fast analog to digital converter. An ADC with a conversion time of about  $100 \mu\text{sec}$  is found to be suitable for the present studies. The parallel outputs of the ADC are stored in Flip-flop registers which on command are transferred to the buffer unit of the digital magnetic tape unit. The sign of the voltage at the input of the ADC, is stored as a sign bit along with the data. The accuracy of data thus recorded in the form

of say 7 data bits and a sign bit is limited to 1 in  $(2^7-1)$  which is sufficiently high.

The data thus recorded on the tape can be spectral analysed and the doppler spectrum of the radar echo can be obtained. Correction can be applied for amplitude fading, and the frequency resolution also will be sufficiently high. The block diagram of this digital data processing system, making use of a PERTEC dual buffer stage along with a PERTEC Tape transport unit is shown in figure (2.27). The compatibility of this unit with the IBM 360 enables the fast analysis of data recorded at a slower rate using the PERTEC unit.



MAGNETIC TAPE UNIT AND THE IMPORTANT INTERFACE UNITS

## C H A P T E R - I I I

### Electrostatic field and electrical conductivities within the equatorial electrojet

#### 3.1 Introduction

##### 3.1.1 Importance of the electric field studies

Measurement of electric field and its variation with altitude in the electrojet region is of significant importance in locating the region of generation of these fields and the mode of transmission from one region to another. The dynamo theory (Stewart, 1882) attempts to explain the generation of electric fields responsible for the currents in the ionosphere. The lack of proper knowledge of parameters required in the theory makes the picture very qualitative. To get a complete picture one requires knowledge of the world wide wind systems, the distribution of electron density, and correct knowledge of the conductivity parameters. The theoretical models, which are basically dependent on assumed values of the electric fields and average atmospheric parameters, fail to give a picture which can explain the major features of the observations.

The electric fields apart from driving the electric currents are responsible for a variety of phenomena in the ionosphere. The sporadic-E and the ionisation drifts in the F-region are manifestations of some such effects. In addition the role of electric fields in the generation mechanism of ionisation irregularities has been well

established by ground-based and rocket-borne experiments. The study with rocket-borne Langmuir probes from Thumba (Prakash et al. 1969a,b, 1970, 1971, 1972) has shown the existence of at least five types of ionisation irregularities, classified according to the instability mechanisms responsible for their generation.

- (i) Streaming irregularities with scale size 1-15 metres generated through two-stream instability mechanism.
- (ii) Irregularities of scale size 1-300 metres, produced through cross-field instability mechanism.
- (iii) Large scale irregularities observed during night times with vertical scale sizes of a few kms. and horizontal scale sizes of the order of about 40 kms. or more. The mechanism of generation of these irregularities is unknown.
- (iv) Irregularities with scale sizes in the range 30-300 metres produced by some unknown mechanisms.
- (v) Irregularities with scale sizes less than a few hundred metres observed below about 90 kms. These are most probably due to neutral turbulence and the wind shears.

The first two types are dependent on the ambient electric fields, the former one being through the streaming velocity of electrons and the latter through the orientation and the strength of the field itself. The characteristic features of these types of irregularities are discussed in section (1.3.2). A clear understanding of the mechanisms of generation of irregularities, requires a knowledge of the electric fields.

### 3.1.2 Estimation of electric field

In-situ measurement of electric fields in the ionosphere involves great technical difficulties as the fields are very small in magnitude. Electric field probes used for this purpose make use of sensors, mounted on long booms and project into the ionised medium. Large errors creep in these measurements because of the inadequate knowledge of the contact potentials of the sensors and the " $V \times B$ " corrections involved in the analysis. So far no reported results concerning the in-situ measurement of electric fields in the equatorial ionosphere exist. Two highly sophisticated rocket-borne experiments were carried out at Thumba, Trivandrum by CNRS group (Sartiel and co-workers) for the measurement of electric fields during the year 1972. The results of these experiments are not yet reported. Hence, one has to depend on indirect estimates of the electric fields. One of the main objectives of the experiments carried out at the equatorial station, Thumba (dip latitude  $0^{\circ} 47'S$ ) India,

during the period 1966-'71 was to study the nature of variation of the electric field and the associated conductivity parameters in the electrojet region. Estimates of the electric fields were made from in-situ measurements of the electrojet current density and electron density using rocket-borne payloads.

### 3.2 Observations and Analysis

#### 3.2.1 In-situ measurements of current density

In-situ measurement of electrojet currents using rocket-borne magnetometers was first suggested by Vestine and others in 1947. Later, the measurements of currents were carried by Singer, Maple and Bowen (1949), Cahill (1959), Maynard and Cahill (1965), Davies et al. (1967), Maynard (1967) and others. The results presented here are important as they are the only available simultaneous measurements of electrojet current density and the electron density.

Proton precession magnetometers were used for the measurement of total intensity of the magnetic field in the electrojet region. The current density profile is estimated from the height profile of the measured magnetic field (Section 2.2.1). The approximations used in the conversion of these magnetic field profiles into current density profiles set a limitation to the accuracy of the results obtained. Though the height estimations are correct to a great degree of accuracy, an error of about 10% is possible in the computed current density values.

### 3.2.2 Rocket measurements of electron density:

Rocket-borne Langmuir probes were used for the measurement of electron density in the E-region over Thumba (Section 2.2.2). Conversion of probe currents into electron density profiles were done mostly using conversion factors obtained from ionosonde, but for one of the flights (Nike Apache 10.37) reported here, it was done using data from an on-board resonance probe (Prakash et al. 1972). As the electron density values are derived from the observed plasma resonances the accuracy of the estimates are quite high.

The accuracy of the measurements with Langmuir probe is mainly determined by the accuracy of conversion of probe current data into electron density values. The disturbance caused by the rocket in the ambient medium also contributes to the inaccuracy of the estimates. An overall error of about 10% is estimated in the computed electron density values except for Flight 10.37, where the accuracy is much higher, as pointed out earlier.

### 3.2.3 Computation of conductivity parameters

Using the observed values of the electron density ( $n_e$ ) and the standard reference atmosphere model (CIRA 1965), the conductivity parameters  $\sigma_0$ ,  $\sigma_1$  and  $\sigma_2$  are calculated using the relations (Section 1.1.2).

$$\sigma_0 = n_e e^2 \left[ \frac{1}{m_e \nu_e} + \frac{1}{m_i \nu_i} \right]$$



$$\sigma_1 = n_e e^2 \left[ \frac{\nu_e}{m_e (\omega_e^2 + \nu_e^2)} + \frac{\nu_i}{m_i (\omega_i^2 + \nu_i^2)} \right]$$

$$\sigma_2 = n_e e^2 \left[ \frac{\omega_e}{m_e (\omega_e^2 + \nu_e^2)} - \frac{\omega_i}{m_i (\omega_i^2 + \nu_i^2)} \right]$$

The collision frequencies of electrons and ions  $\nu_e$  and  $\nu_i$  respectively are calculated using Chapman's formulae (Section 1.1.2).

$$\nu_{en} = 5.4 \times 10^{-10} N_0 T_0^{1/2}$$

$$\nu_{in} = 2.6 \times 10^{-9} m_i^{-1/2} (N_0 + n_e)$$

$$\nu_{ei} = \left[ 34 + 4.18 \log(T^3/n_e) \right] n_e T^{-3/2}$$

and

$$\nu_e = \nu_{ei} + \nu_{en}, \quad \nu_i = \nu_{ei} + \nu_{in}$$

An assumption that the vertical currents induced in the electrojet region by the primary field  $E$  are inhibited (Baker and Martin, 1953) leads to a Hall polarisation field given by the relation, (Section 1.1.2)

$$E_p = (\sigma_2 / \sigma_1) E$$

The conductivity of the medium is enhanced by this polarisation field and the effective conductivity  $\sigma_3$  (Section 1.1.2) is given by the relation,

$$\sigma_3 = \sigma_1 + \sigma_2^2 / \sigma_1$$

The existence of meridional currents in the electrojet region modifies the polarisation field  $E_p$ , and has been computed by Suguirra and Poros (1968) for a set of assumed boundary conditions for the current function. The effective conductivity  $\sigma_3$  also gets modified. The polarisation

field profile thus obtained for an assumed primary field of 2.5 mv/meter is shown in figure (3.1). With  $E_p$  profile obtained from the relation  $E_p = \frac{\sigma_2}{\sigma_1} E$  for  $E = 2.5$  mv/meter. The lower scale represents the computed  $\sigma_2/\sigma_1$  values and the upper scale the polarisation field. The close agreement between the two results justifies the assumption of inhibition of meridional currents, the approximation used in the computation of  $\sigma_3$ .

#### 3.2.4 Estimation of electric field profiles

The effective conductivity profile, thus obtained, along with the observed current density values, is used for the computation of the electrostatic fields, using the relation  $J = \sigma_3 E$ . The basic assumptions used in the present calculations are:

- (i) The electron density is equal to the positive ion density and negative ions are absent.
- (ii) Ions are assumed to be singly ionised.
- (iii) The ions are assumed to be of the same kind with an average mass  $m_i$ .
- (iv) The neutral temperature  $T_g$  is equal to the electron and ion temperatures  $T_e$  and  $T_i$  respectively. Effect of joule heating is neglected.
- (v) The collision frequencies are given by the Chapman's formulae.

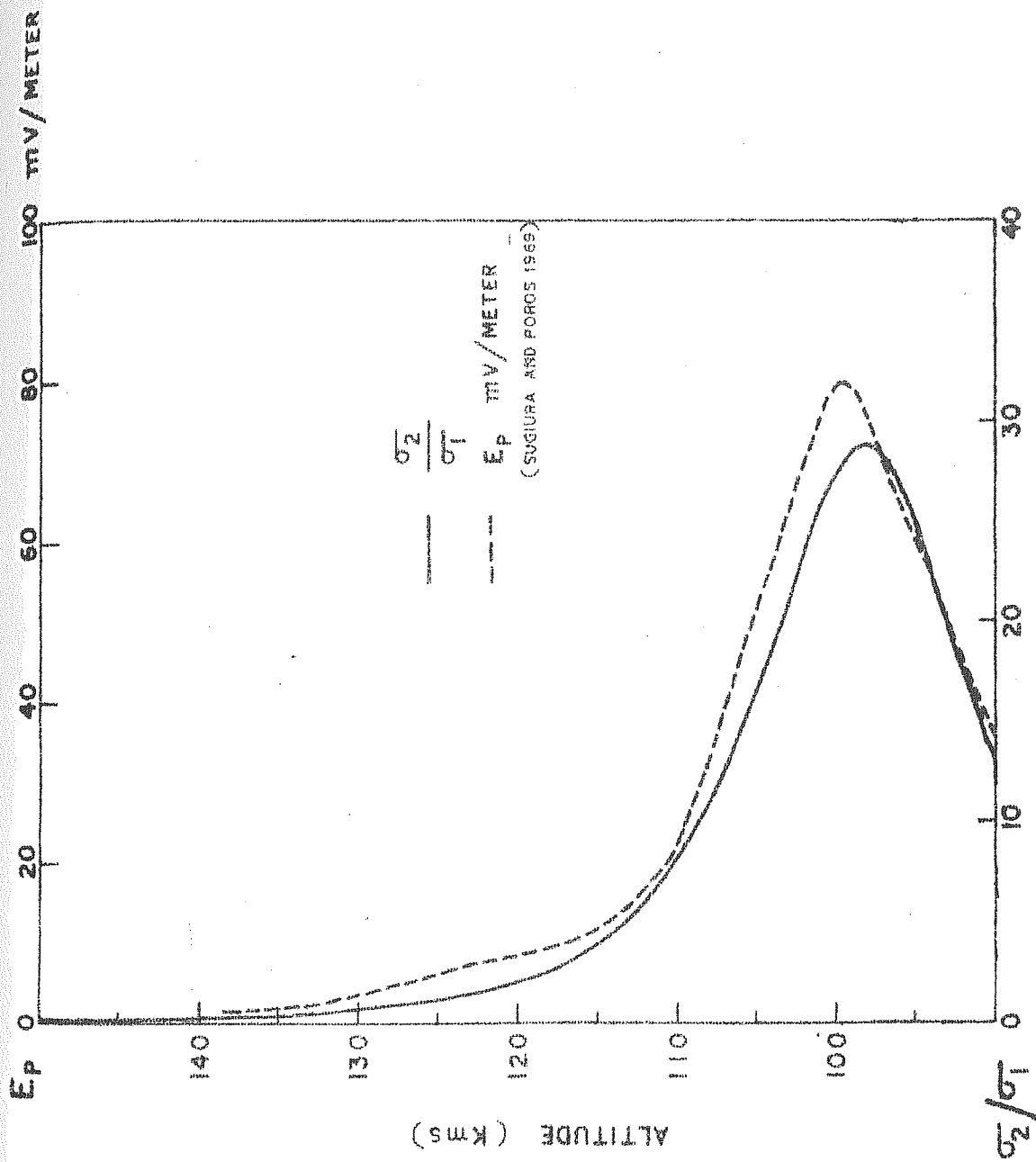


FIG. 3.1: COMPUTED  $\sigma_2/\sigma_1$  PROFILE COMPARED WITH THE PROFILE OF THE VERTICAL POLARISATION FIELD (FOR A PRIMARY FIELD OF 2.5 mV/m) AS GIVEN BY THE MODEL DUE TO SUGIURA AND POROS (1969).

- (vi) A standard atmospheric model is assumed for the distribution of neutral particles in the atmosphere.

The significance of the present results in relation to some of the assumptions made is discussed in section (3.4) of this chapter.

### 3.3 Results

#### 3.3.1 Flight details

Table (3.1) shows a summary of the Langmuir probe and proton precession magnetometer flights from Thumba. 20.05 and 20.07 were daytime flights both containing magnetometer and Langmuir probe payloads; while 10.37 and 20.06 were daytime flights, the former one giving only Langmuir probe data and the latter one only magnetometer data. The local times of these flights being nearly same (1040 hrs. IST and 1108 hrs. IST respectively), the data from one set was used to supplement the data from the other set. Thus for practical purposes there were three daytime flights. One night time flight 20.08 which contained both Langmuir probe and magnetometer payloads, was not used for the present studies because of the large inaccuracies involved in night time current density measurements. The daytime data has been used to study the height variations of the electrostatic field and the associated conductivities.

Table (3.1)

Sl.No.	Flight	Date and Time	Available results
1.	20.05	7 July 1966 1345 hrs.IST	Langmuir probe and magnetometer data
2.	20.06	29 Aug.1968 1108 hrs.IST	Only magnetometer data
3.	20.07	29 Aug.1968 1415 hrs.IST	Langmuir probe and magnetometer data
4.	20.08	29 Aug.1968 2300 hrs.IST	Langmuir probe and magnetometer data
5.	10.37	28 Jan.1971 1040 hrs.IST	Only Langmuir probe data

### 3.3.2 Summary of the results

Figures (3.2), (3.3) and (3.4) show the experimentally observed electrojet current density and electron density profiles for the three daytime flights. Also inserted in the figures are the computed profiles of the Cowling conductivity  $\sigma_3$  and the  $\sigma_2/\sigma_1$  profile of figure (3.1).

Flight 20.05 (fig.3.2) shows the current density maximum around 106 kms. and an electron density maximum around 107 kms. in the electrojet region. Computed  $\sigma_2/\sigma_1$  has a maximum at about 99 kms, and  $\sigma_3$  at about 103 kms. The corresponding heights in the case of 20.07 are 107 kms for  $J$ , 115 kms. for  $n_e$  and 103 kms. for  $\sigma_3$ . These values for 20.06 (complemented by 10.37) are 105 kms, 109 kms and 102 kms. respectively.  $\sigma_2/\sigma_1$  peak does not show any

7 July 1966  
1345h IST

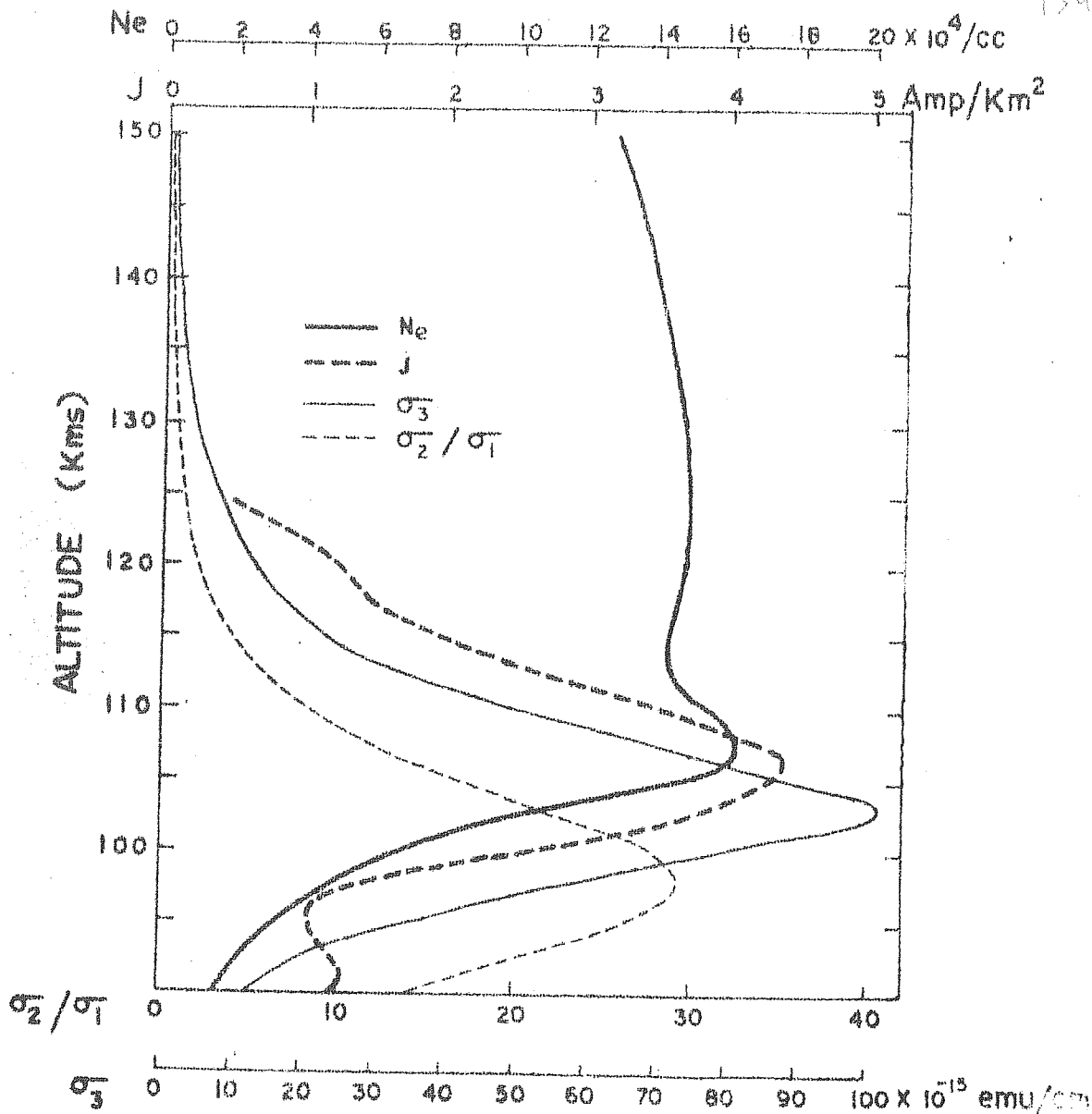
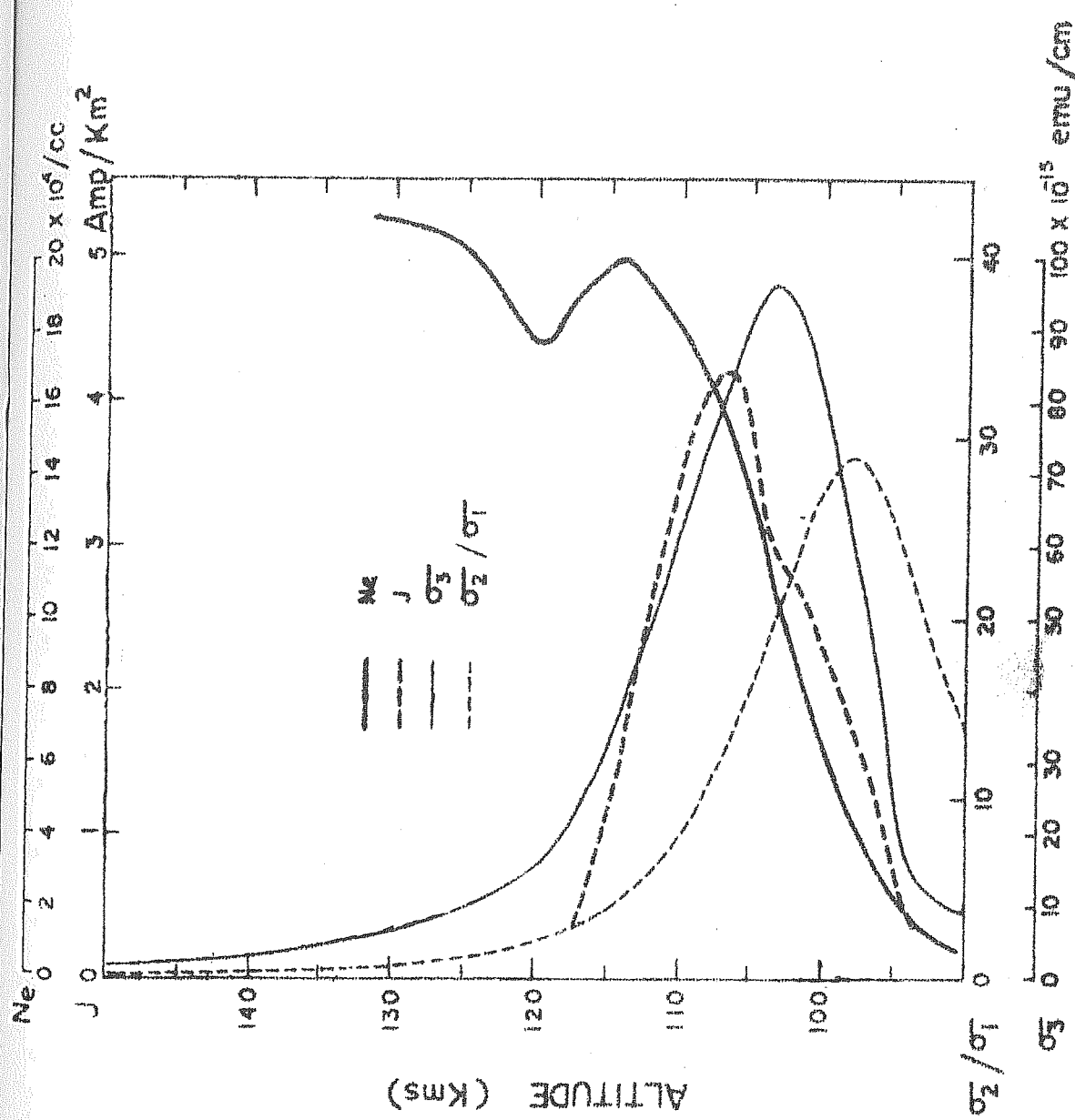


FIG. 3.2: COMPUTED VALUES OF  $\sigma_2/\sigma_1$  AND THE EFFECTIVE CONDUCTIVITY  $\sigma_3$  ARE COMPARED WITH THE EXPERIMENTALLY MEASURED ELECTROJET CURRENT DENSITY. ALSO SHOWN IS THE EXPERIMENTAL ELECTRON DENSITY PROFILE USED IN THE COMPUTATIONS - FLIGHT 20.05

29 Aug 68  
14151ST



F. 3. 3.3: COMPUTED VALUES OF  $\sigma_2/\sigma_1$  AND THE EFFECTIVE CONDUCTIVITY  $\sigma_3$  ARE COMPARED WITH THE EXPERIMENTALLY MEASURED ELECTROJET CURRENT DENSITY. ALSO SHOWN IS THE EXPERIMENTAL ELECTRON DENSITY PROFILE USED IN THE COMPUTATIONS - FLIGHT 70.07

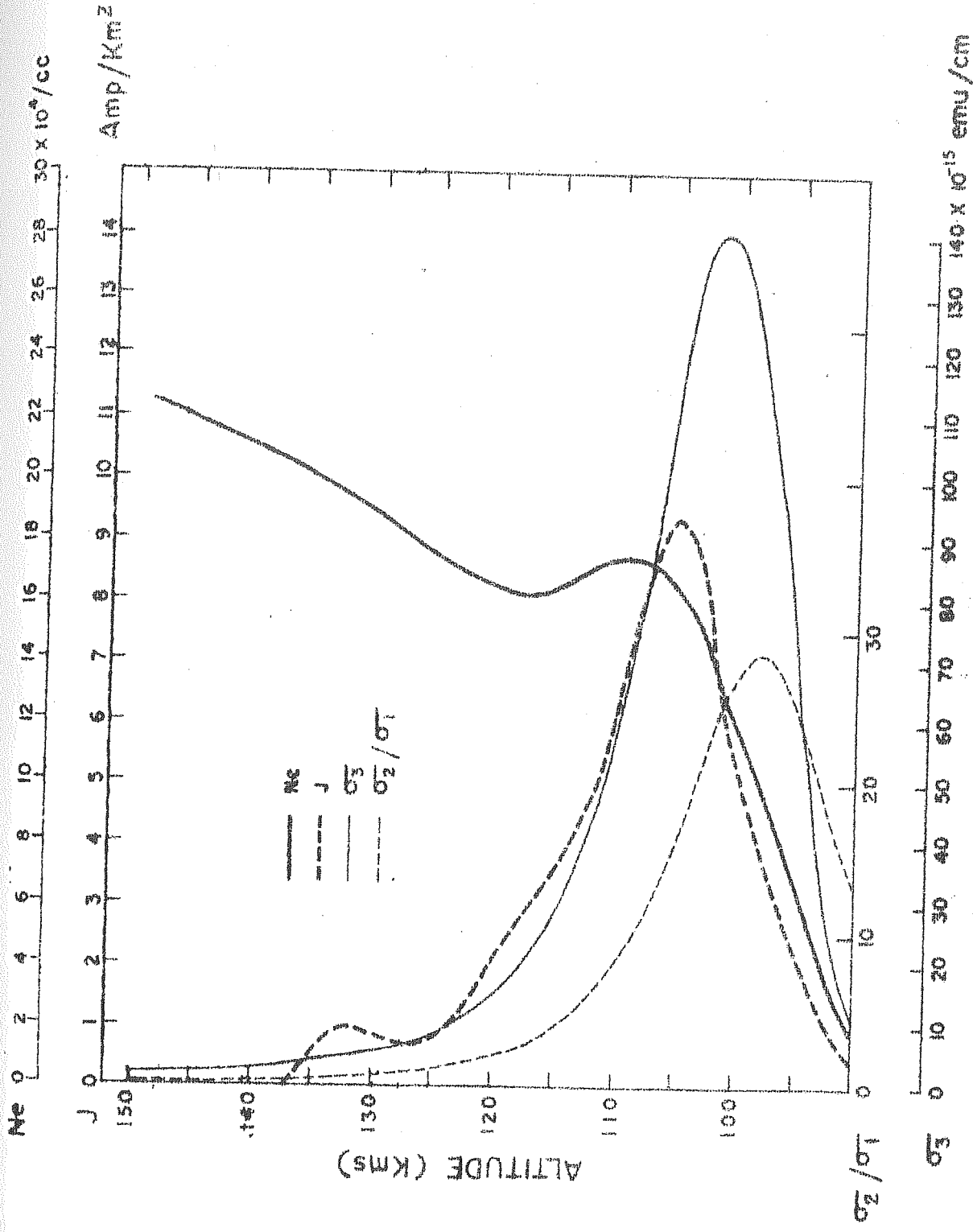


FIG. 3.4:  $\sigma_2/\sigma_1$  AND THE EFFECTIVE CONDUCTIVITY  $\sigma_3$  COMPUTED FROM THE ELECTRON DENSITY PROFILE OF FLIGHT 10.37 SHOWN ALONG WITH THE ELECTROJET CURRENT MEASURED ON FLIGHT 20.06. THE ELECTRON DENSITY PROFILE USED IN THE COMPUTATION IS ALSO SHOWN IN THE FIGURE.



variation in its peak height from flight to flight. It always remains below 100 kms. The height of  $\sigma_3$  peak is consistently above 100 kms (at about 103 kms.) in all the flights. The current density  $J$  in all the cases can be seen to peak at a height above 105 kms. The peak of the  $\sigma_2$  profile depends on the nature of the electron density profile. A closer examination of the figures shows the following additional features.

- (i) A decrease in the current density by a factor of half is not accompanied by equally significant changes in the electron density or Cowling conductivity parameters. The fall in the current density, hence, seems to be due to a fall in the electrostatic field strength.
- (ii) The electron density peak in the E-region is seen to be well above the maximum of the electrojet current density and the Cowling conductivity. This feature is relevant to the region of generation of streaming irregularities.
- (iii) Cowling conductivity  $\sigma_3$  reaches a maximum at a height which is always above the peak of  $\sigma_2/\sigma_1$ . The height difference is of the order of a few kms.
- (iv) The electrojet current density reaches a maximum at a height which is consistently above the peak of the Cowling conductivity  $\sigma_3$ . The height difference is of the order of a few kms.

### 3.4 Discussion of results

#### 3.4.1 Region of streaming irregularities

The electron density peak in the E region observed consistently above the peaks of current density and Cowling conductivity profiles is of some relevance in the study of ionisation irregularities that are known to be associated with the streaming of electrons. When the drift velocity of electrons with respect to the positive ions, crosses a threshold, the conditions become favourable for the development of two-stream instability mechanism (Farley 1963, Farley and Balsley 1971). The irregularities produced by this mechanism classified as Type I from ground-based VHF scatter radar studies are, therefore, confined to those regions where the streaming velocity of electrons with respect to ions exceeds the threshold. The current density  $J$  is related to the drift velocity  $v_d$  and the number density  $n_e$  of the electrons by the relation

$$J = n_e e v_d$$

It was pointed out in section (3.3.2) that the electron density continues to show an increase with height even after the current density has reached its peak value and is in the decreasing phase. This indicates that the drift velocity  $v_d$  of electrons relative to ions falls off at a much faster rate than  $J$ , above the current density peak. In other words,  $v_d$  has its maximum value below the current density peak.

### 3.4.2 Nature of Cowling conductivity

The effective Cowling conductivity  $\sigma_3$  is given by the relation

$$\sigma_3 = \sigma_1 + \left( \frac{\sigma_2}{\sigma_1} \right) \sigma_1$$

The first term  $\sigma_1$ , on the right hand side of the above relation is less by a factor of the order of  $10^3$  than the second term in the region near the Cowling conductivity peak and hence the above relation can be approximated to

$$\sigma_3 \approx \sigma_2 \left( \frac{\sigma_2}{\sigma_1} \right)$$

The ratio  $\sigma_2/\sigma_1$  to a first approximation is independent of the ambient electron density and has a peak below 100 kms. The variations with altitude in  $\sigma_3$  has an  $n_e$  dependence through  $\sigma_2$  the Hall conductivity. As can be seen from the equation (1.6, Section 1.1.2)  $\sigma_2$  has an explicit dependence on the electron density and, therefore, the peak of  $\sigma_2$  profile varies with shift in the peak of the  $n_e$  profile. In general,  $\sigma_2$  maximum is at a higher altitude than the  $\sigma_2/\sigma_1$  maximum. The increase in  $\sigma_2$  with  $n_e$  above the maximum of  $\sigma_2/\sigma_1$  lifts the peak of  $\sigma_3$  to a level above the maximum of  $\sigma_2/\sigma_1$ . The role of collision parameters and electric fields in the variation with height of  $\sigma_3$  will be discussed in the next section which deals with the electrostatic fields in the electrojet region.

### 3.4.3 Electrostatic fields within the electrojet

Though the position of the electrojet current density peak has been found to be different on different occasions, it has been consistently found to be above the Cowling conductivity peak, the height difference being a few kms. This may be due to one or more of the following reasons:

- (i) The computed  $\sigma_1$  and  $\sigma_2$  are unrealistic
- (ii) There exists a vertical gradient in the primary electric field, in the electrojet region.

The computed Cowling conductivity profile, if deviates considerably from the actual conductivity profile in the electrojet region, can cause such a height discrepancy in the computed conductivity and measured current density profiles. Such a deviation can be expected to be due to inadequacies in the neutral atmospheric model used or in the theoretical formulae used in the computation of collision frequencies. Instead of Chapman's formulae used here for collision frequencies, when the modified Bank's formulae were used, the  $\sigma_3$  profiles came down by a few kms. thereby increasing the height difference between the current density and the conductivity profiles. In this context it is interesting to note that Thrane and Piggot (1966) found that the electron collision frequencies calculated from their radio frequency experiments differ very much from the values computed for the standard atmosphere at height

above 90 kms. The experimental values are larger than the computed values by a factor which is close to unity at 100 kms. is 3 at 110 kms. and reaches a value of 10 at 130 kms. In the height region of about 105 kms. ( $\omega_e \simeq 7.04 \times 10^6$ ,  $\nu_e \simeq 4 \times 10^4$ ,  $\omega_i \simeq 1.28 \times 10^2$  and  $\nu_i \simeq 4.34 \times 10^3$ ) considering the relative magnitude of the gyro-frequency and collision parameters, the expressions for  $\sigma_1$  and  $\sigma_2$  can be approximated to

$$\sigma_1 = n_e e^2 \left[ \frac{\nu_e}{m_e \omega_e^2} + \frac{1}{m_i \nu_i} \right] \quad \text{and}$$

$$\sigma_2 \simeq n_e e^2 \left[ \frac{1}{m_e \omega_e} \right]$$

As can be seen from these relations, an increase in  $\nu_e$  will increase the Pedersen conductivity  $\sigma_1$ , while the Hall conductivity  $\sigma_2$  remains more or less unaffected. A detailed computation of these parameters has shown that even a large increase in collision frequencies as reported by Thrane and Piggot, could not lift the Cowling conductivity profile, by a few kms. and make its peak coincide with the current density peak.

As pointed out earlier, the collision frequencies used here were calculated for a standard model atmosphere (CIRA 1965) with the assumption that  $T_e = T_i = T_g$  where  $T_e$  is the electron temperature,  $T_i$  the ion temperature and  $T_g$  the neutral temperature. In actual case the presence of an external electric field will raise the kinetic temperature of both electrons and ions through joule heating; the

electrons being heated more than the ions. Rocket observations (Prakash et al. 1967) using Langmuir probe payloads, gave higher electron temperatures than that given by the CIRI model for neutral particles. The reliability of these measurements, however, is not well established. Such an increase in the kinetic temperature will reflect in the collision frequencies. The electron neutral collision frequency which is proportional to the square root of the kinetic temperature will show an increase (Section 1.1.2). As has already been discussed, such an increase in the electron collision frequency cannot lift the Cowling conductivity profile upwards by a few kms. It must also be noted here that if these height discrepancies are to be attributed to inadequacies in the atmospheric models used drastic changes in these models will be necessary to lift the conductivity profile upwards by a few kms, and make its peak coincide with the current density profile.

Thus one can rule out the first possibility of the conductivity parameters being unrealistic, in explaining the height differences in the peaks of the conductivity and the current density, unless there exist drastic difference in the atmospheric model used. Hence, a more straightforward explanation for the observed height discrepancy can be that the horizontal electrostatic field is varying with altitude. If the primary eastward electric

field increases with altitude in the electrojet region, the electrojet current density can peak at a greater height than the Cowling conductivity. The values of the electrostatic field for the different flights, calculated from the equation  $J = \sigma_3 E$  as discussed earlier, are given in fig. (3.5).

From the figure it can be seen that the electric field tends to increase steadily with altitude in the electrojet region for all the flights except for 20.05. For 20.05 the electric field exhibits a tendency towards a maximum at about 110 kms. Sastry (1970) finds that the results of 20.05 were exceptional in other respects also. The electric field value ranges from about 0.3 mv/m at about 90 kms. to about 1.4 mv/m at about 115 kms. The electric fields in the region of maximum currents ranges from 0.4 mv/m to 0.9 mv/m. The electric field value of 2.5 mv/m assumed by Suguira and Cain (1966) and Suguira and Poros (1969) in their electrojet models, is much higher than the present values by a factor ranging from 3 to 8. The electric field value of 2.5 mv/m seems to be very unrealistic.

The primary field thus being a parameter varying with altitude in the electrojet region, the Hall polarisation field will no longer have a height profile similar to that of  $\sigma_2/\sigma_1$  as expected from equation (1.16 - Section 1.1.2). Equation (1.16) is used to compute the height profiles of the Hall polarisation field from the primary fields computed earlier for the different flights.

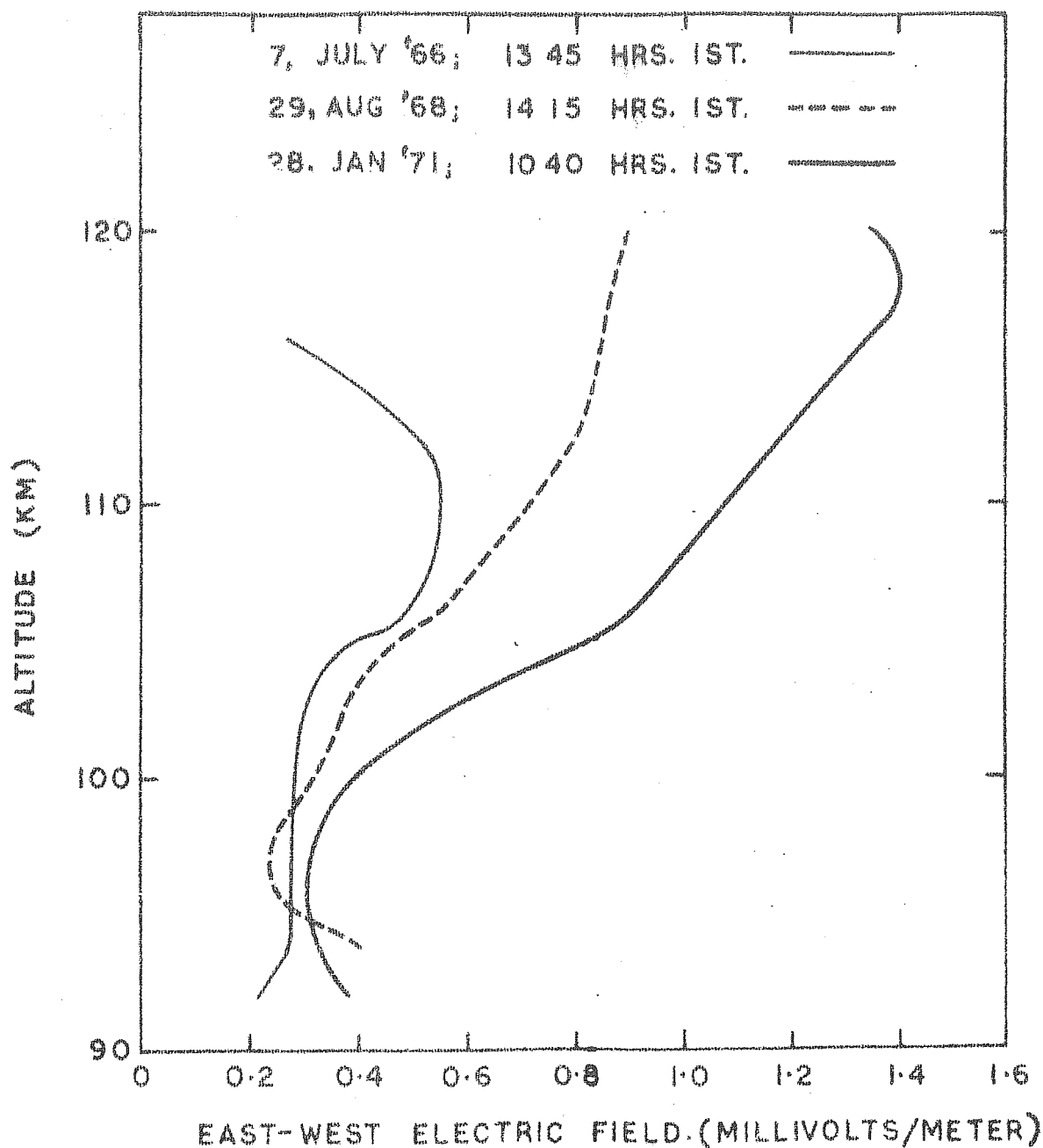


FIG. 3.5: THE PRIMARY EAST-WEST ELECTROSTATIC FIELD  
CALCULATED FROM THE ELECTRICAL CONDUCTIVITY  
AND THE ELECTRIC CURRENTS OF FIGURES 3.2-3.4



7 JULY '66 1345 HRS 15 T  
 29 AUG '68 1415 HRS 15 T  
 28 JAN '71 1040 HRS 15 T

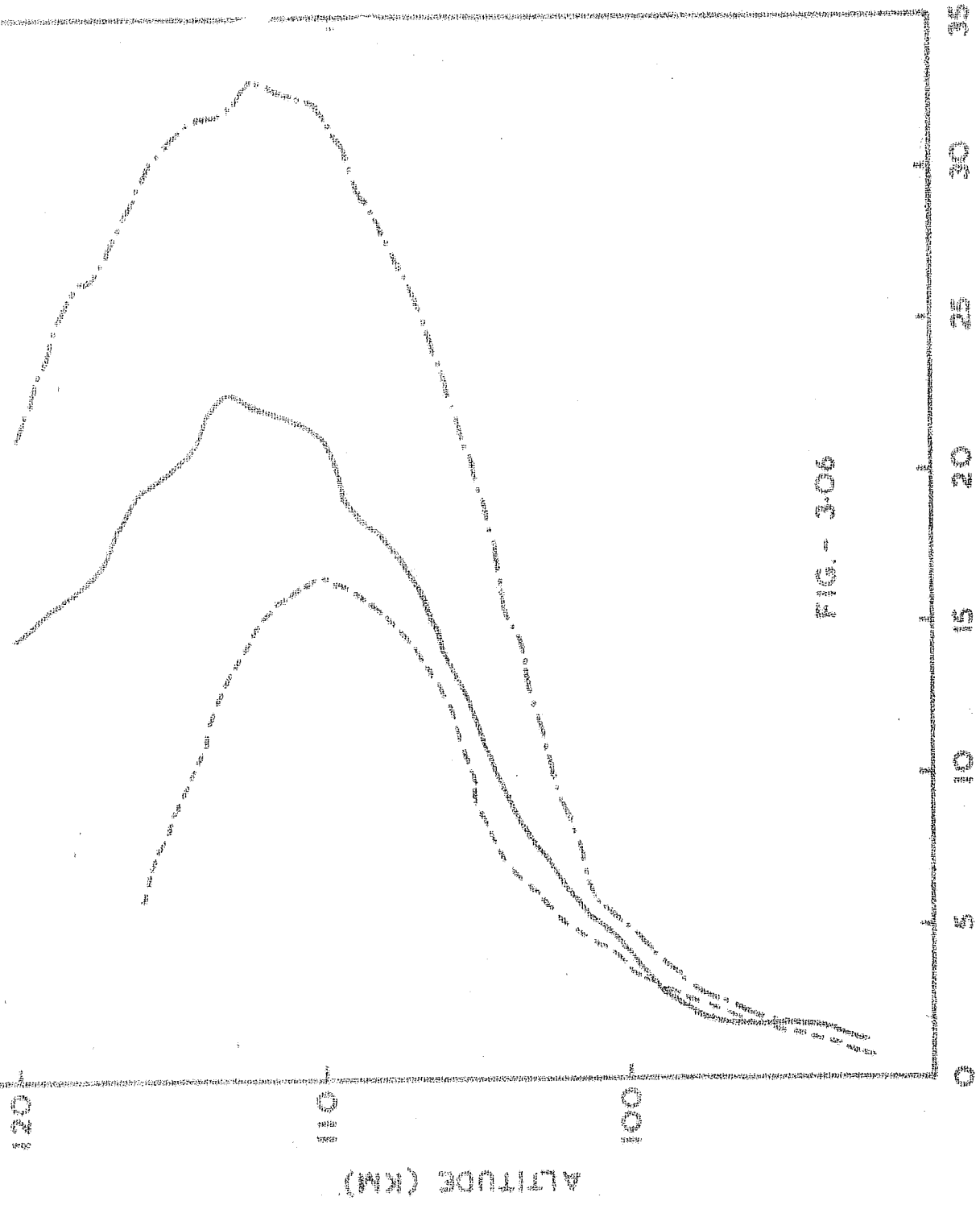


FIG. - 3.06

VERTICAL POLARISATION FIELD  
 MILLIVOLTS/METER

Fig. (3.6) shows the height variation of the Hall polarisation field.

The Hall polarisation field has an important role, in the generation mechanisms of irregularities. A critical study of the variations in  $E_p$  in relation to the variations in the electron density and its gradients is necessary for understanding the crossfield instability mechanism and the influence of the electron streaming on modifying the scale sizes of the irregularities produced by this mechanism.

### 3.5 Conclusions

The observations and results presented here lead to the following conclusions:

(1) In the electrojet region of the ionosphere, the Cowling conductivity has a maximum at about 103 kms. and is always below the electron density peak. It is seen consistently above the maximum of  $\sigma_2/\sigma_1$  which is below 100 kms.

(2) The electrojet current density reaches its maximum at a height which is a few kms. above the maximum of the east-west conductivity. This is, most likely, due to an increase in the value of the primary east-west electric field, with increase in altitude.

Inadequacies in the neutral atmospheric model, or in the assumptions involved in the evaluation of collision frequencies, and its variation with joule heating are not likely to explain the height differences in the conductivity and current density peaks.

(3) The magnitude of the electric fields obtained by the present studies show that the value assumed by Suguira and Cain, and Suguira and Poros in their electrojet model is far from realistic; being more by a factor ranging from 3 to 8.

(4) The drift velocities of electrons reach a maximum at the current density peak and shows a decrease with increase in height.

Electric fields in the E-region during Morning  
and Evening hours

4.1 Introduction

4.1.1 Objectives of present study

The nature of the electric fields in the E-region during the morning and evening hours, close to the electrojet reversal periods, form an important aspect of the investigation of the sources of these fields and their transmission from place to place. The electrojet currents being weak during these periods the normal method of studying the currents and the associated electric fields, through an analysis of ground level geomagnetic field variations, or from the conventional ionogram traces from the E-region, does not yield conclusive results. The basic assumption of a dynamo field, that does not vary with altitude or time of the day, used in all the existing electrojet models is not supported by experimental results and, hence, is questionable. These models, therefore, are incapable of giving any quantitative picture of the current system which can be used for the electric field studies. Another drawback of these models (Suguira and Cain 1966, Suguira and Poros 1969) is the large unrealistic field value assumed in the determination of the current contours. A proper understanding of these fields, as regards their origin and distribution, requires a complete knowledge of their variation with time and height. The knowledge of these fields during the morning and evening hours, hence, has special significance.

Back scatter radar observations made from Thumba (dip latitude  $0^{\circ} 47'S$ ) during the morning and evening hours, for an year (1973-74) are used to estimate the general nature of the electric fields and their variation with altitude during the electrojet reversal periods.

#### 4.1.2 Electric fields from drift velocities

The electrojet current density  $J$  is related to the electron density  $n_e$  and the drift velocity  $v_d$  of the electrons with respect to the ions by the relation,

$$J = n_e e v_d$$

where  $e$  is the electronic charge. If  $E$  is the primary electric field driving the electrojet currents and  $\sigma_3$  is the effective Cowling conductivity of the medium (Ref. Chapter I), then the electrojet current density  $J$  is given by the relation,

$$J = \sigma_3 E$$

From these two relations one can write  $E$  in terms of the drift velocity  $v_d$  of electrons as

$$E = (n_e e / \sigma_3) v_d$$

This shows a linear relation between  $E$  and  $v_d$  since the term inside the bracket is independent of  $n_e$  because of the explicit dependence of  $\sigma_3$  on  $n_e$  (Equations 1.05, 1.06 and 1.20, Section 1.1.2) to a first approximation. The constant of proportional is different at different altitudes.

As discussed in section (2.3), the drift velocity of electrons are obtained from a study of the radar echoes. The echo contains informations regarding the variations in amplitude of the ionisation irregularities, in the scattering volume, as variations in the amplitude of the echo; and regarding the motion of these irregularities as a change in its spectral characteristics. The phase velocity of the irregularities obtained from the spectra, are related to the drift velocity of electrons. The nature of the relation is different for different types of irregularities and depends on the operative instability mechanism. Knowing the drift velocity of the electrons, one can estimate the electric fields driving the currents.

#### 4.1.3 Height variation of the electric field

The region of generation of irregularities depends on the ambient physical parameters and the instability mechanism responsible for the generation of these irregularities. For example, a region where the drift velocity of electrons exceed the ion acoustic velocity, the two-stream instability mechanism is favoured; while a region, where the electron density gradients are high, and there exist electric fields in the direction of these gradients is favourable for the development of crossfield instability mechanism. Both these mechanisms being controlled by the electric fields, a study of the height variation of the region of generation of the ionisation irregularities will show the nature of variation of

these fields with altitude. The back scatter echo peak corresponds to the height region containing irregularities of maximum amplitude. Informations regarding the variation with altitude of the electric fields can be obtained from a study of the time variation in the peak of the radar echo. Though a change in the distribution of electron density gradients with time can cause a shift in the radar echo peak, this effect can be neglected, in case when the variation in the electron distribution are slow compared with the period over which the echo peak shows a considerable shift in altitude.

These observations were carried out during both morning and evening hours close to the electrojet current reversals to study the nature of height variation of the primary electric fields.

#### 4.2 Observations and results

##### 4.2.1 Morning hours

The doppler spectra of the back scatter radar echoes were observed during morning and evening hours, on a number of days. The transmitting and receiving antennas had their beams looking at the electrojet region, at an angle of  $30^{\circ}$  with the vertical, towards the west. Figure (4.1) represents the typical nature of the spectra. The spectral curves are arranged in a time sequence, starting from an early morning hour. The time at which a particular spectrum is taken,

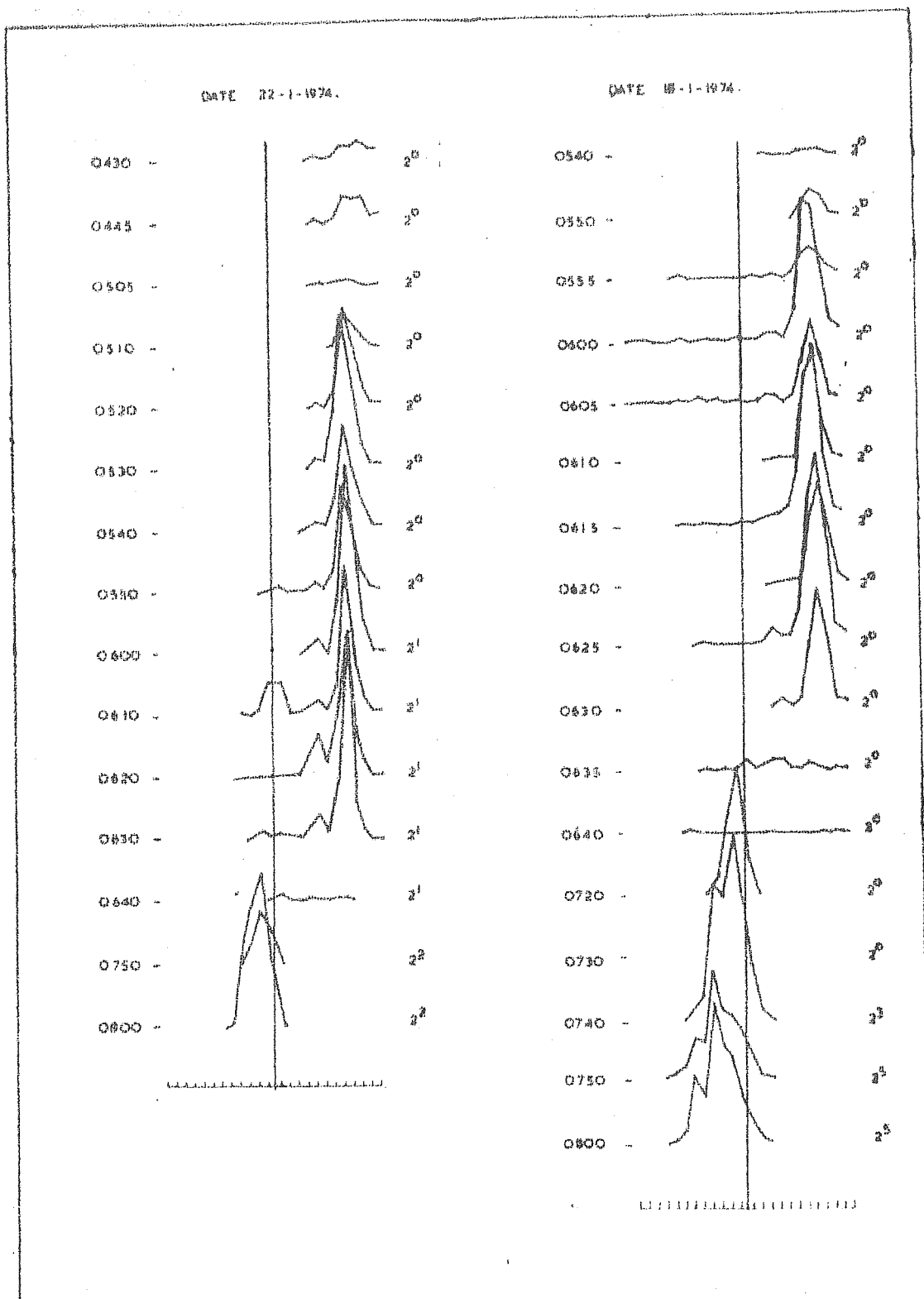


FIG. 4.1: TIME VARIATION IN THE SPECTRAL CHARACTERISTICS DURING THE MORNING HOURS FOR TWO DAYS (22 JAN. 1974 AND 18 JANUARY 1974) - X AXIS REPRESENTS THE DOPPLER SHIFT IN FREQUENCY OF THE RECEIVED SIGNAL AND RANGES FROM -175 Hz to +175 Hz.



is indicated on the left side of the spectrum, and the relative attenuation in the amplitude is indicated by the number on the right side of the spectrum. For example, a spectrum with an attenuation  $2^2$  shows that spectrum has an amplitude which is actually 4 times the amplitude shown in the diagram. The one with no attenuation ( $2^0$ ) is taken as the reference spectrum.

The amplitude of a spectrum is a measure of the mean square fluctuations in the amplitude of the electron density irregularities of scale size about 3 meters. The electrojet currents being comparatively weak during the morning hours, the amplitudes of the irregularities are small and results in a low signal to noise ratio during these periods. Though the study of radar echoes was carried out on a number of days, useful data was obtained only on a few occasions. The main features of the doppler spectra observed during morning hours at times close to the electrojet reversal are the following:

- (1) On an average before reversal, there exists a narrow peak in the positive side of the doppler spectrum corresponding to drift velocities of about 360 m/sec, indicating the presence of irregularities with phase velocities near the ion acoustic velocity. Near reversal the amplitude of the spectrum decreases with time though considerable change in the peak doppler shift is not associated with these decreases.

The characteristics of the spectra observed before the reversal show that they are produced by type I irregularities (Section 1.3.2). This shows that the electrons are streaming in the eastward direction with velocities exceeding the ion acoustic velocity.

(2) The transition or the reversal period is characterised by a complete absence of the radar echo.

(3) The discrepancies of the radar echo during the transition period is followed by the usual daytime spectra characterised by negative doppler shifts. These spectra are in general broad and show the characteristics of spectra produced by the type II irregularities (Section 1.3.2); being generated by the crossfield instability mechanism. The doppler shift in the spectra correspond to drift velocities much less than the ion acoustic velocity.

These changes in the spectral characteristics are associated with changes in the average height of the scattering volume which contains the ionisation irregularities responsible for the echo. A time variation in the peak of the radar echo which represents the scattering volume containing irregularities of maximum amplitude is measured in terms of the variation in the time delay from the transmitted pulse. This, then, represents a height shift in this region.

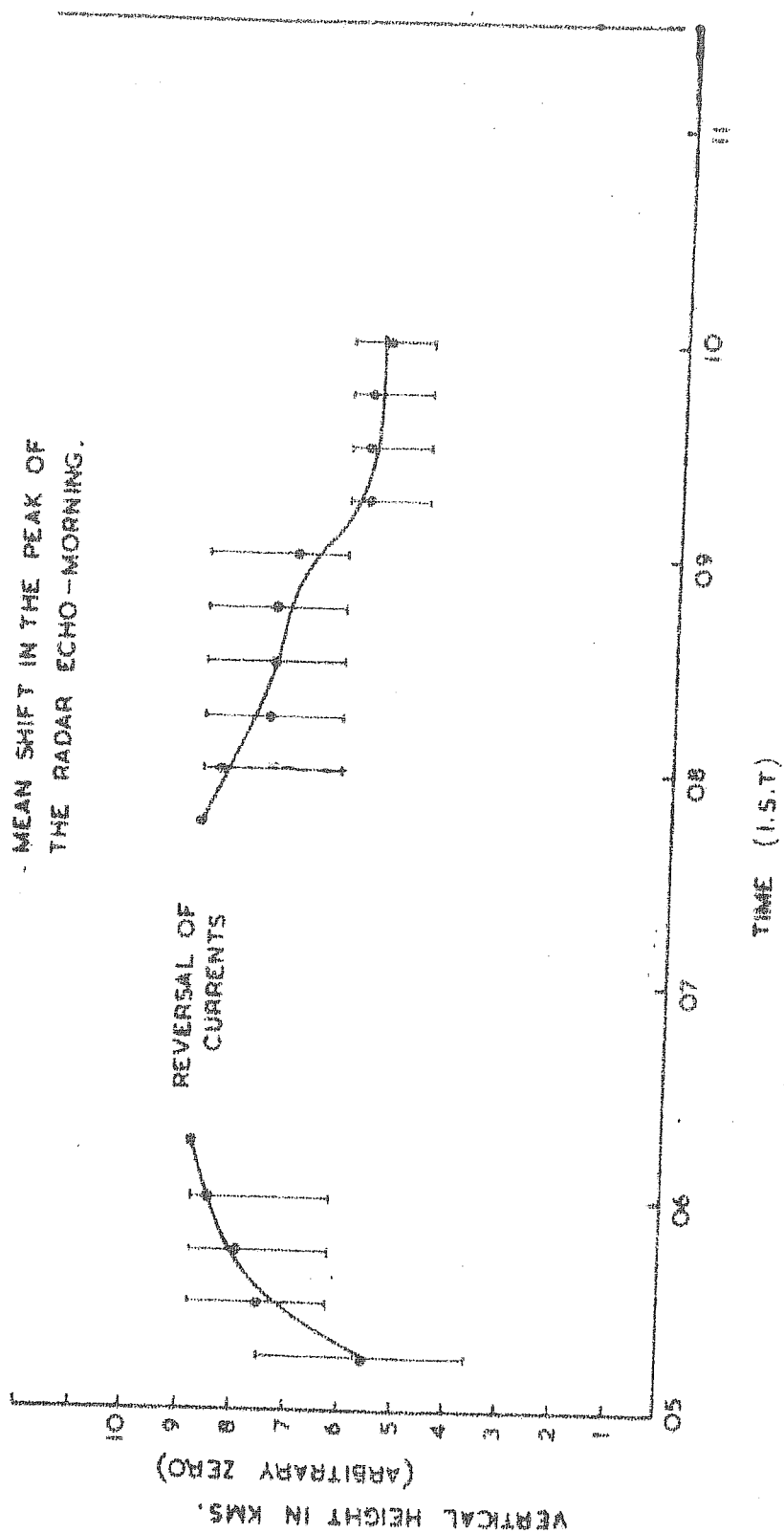


FIG. 4.2: MEAN SHIFT IN THE PEAK OF THE RADAR ECHO DURING MORNING HOURS. HEAVY  
DOTS INDICATE THE AVERAGE FOR A FEW DAYS AND THE VERTICAL BARS SHOW  
THE SCATTERING OF INDIVIDUAL OBSERVATIONS ABOUT THE MEAN.

The shifts in the altitude corresponding to the echo peak, were observed for a few days. The dots in figure (4.2) indicate the average altitudes of the echo peaks and the vertical bars indicate the scatter of individual observations about the average altitude. It can be seen from the figure that the altitude of maximum echo moves higher as the reversal period is approached either from the pre-reversal side or the post-reversal side. This indicates that there is an upward shift in the region of generation of irregularities as the reversal period is approached. In other words, these regions are higher during times close to the reversal period, than before or after the reversal period.

#### 4.2.2 Evening hours

Observations of the radar echoes and their spectral variations were made starting from a few hours before the evening reversal till a few hours after the reversal in a similar way as in the morning hours. Figure (4.3) represents typical spectra observed during these periods.

In general, the following features can be observed in the time sequence of the spectra:

- (1) The spectra generally are broad and indicate the presence of irregularities moving with low drift velocities of the order of few tens of meters in the east-west direction before the reversal. The peak of the doppler shift shows a

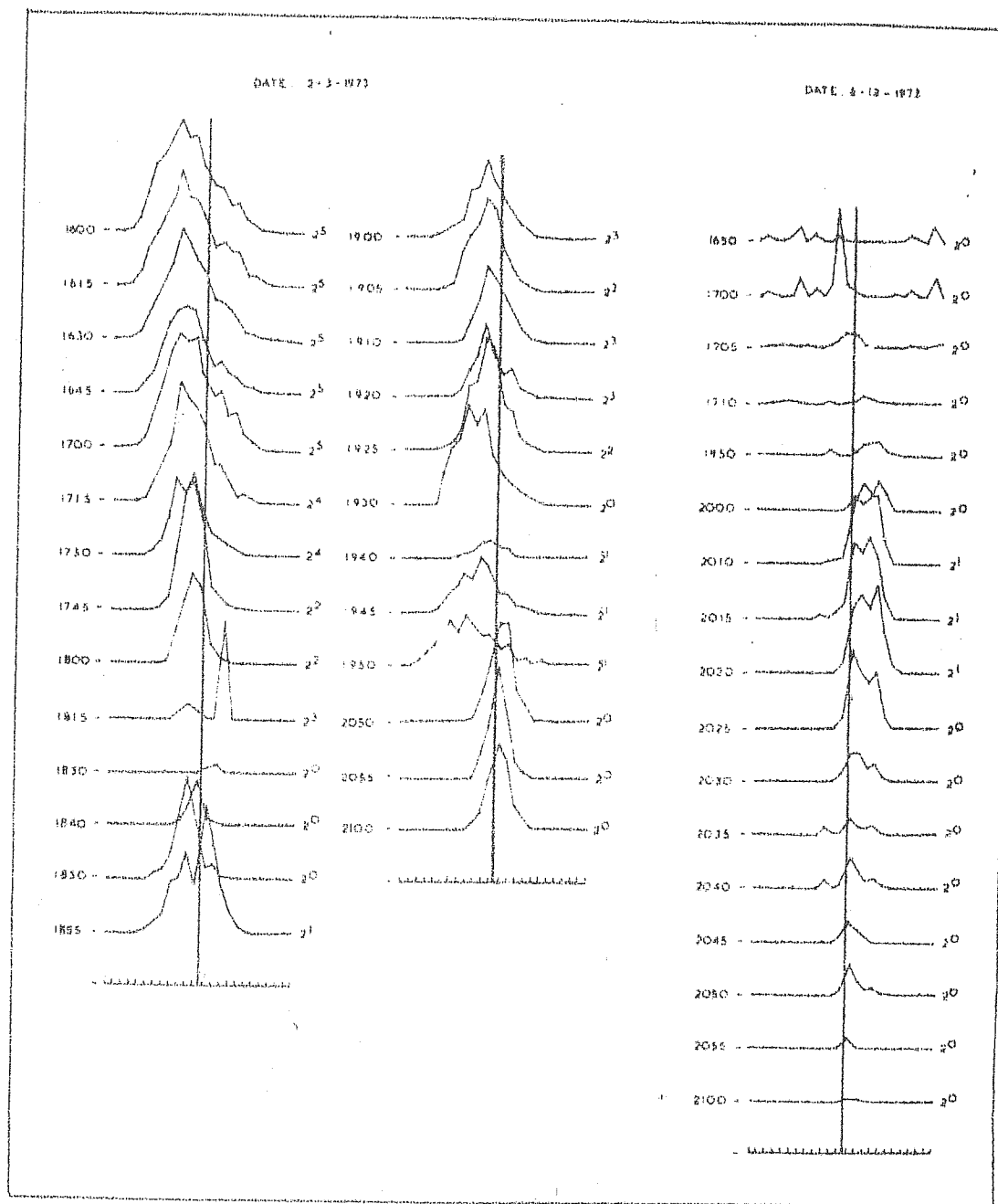


FIG. 4.3: RADAR ECHO - SPECTRAL VARIATION DURING EVENING HOURS (SPECTRAL RANGE : -175 Hz to +175 Hz).

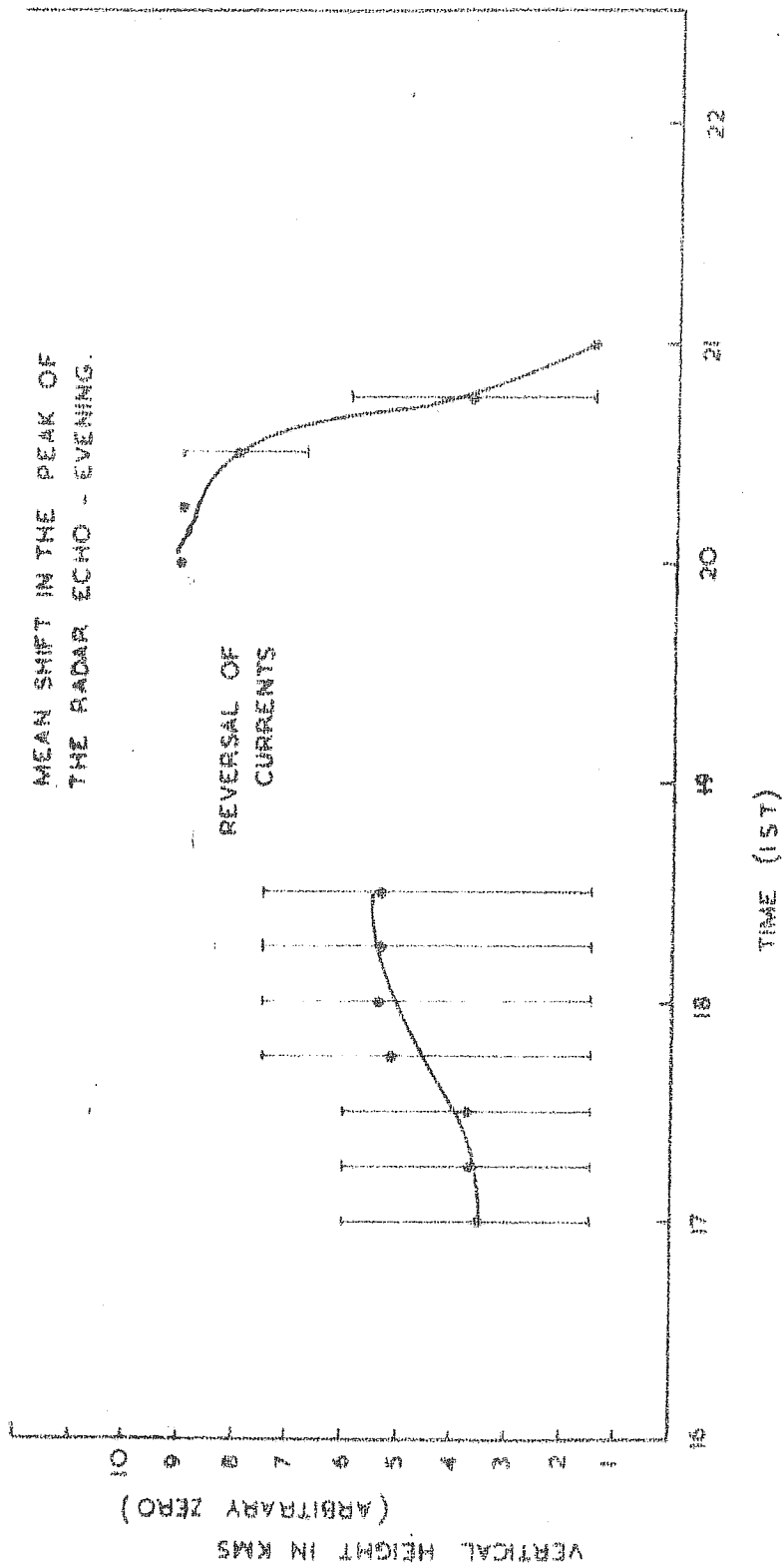


FIG. 4.4: MEAN SHIFT IN THE PEAK OF THE RADAR ECHO DURING EVENING HOURS. HEAVY DOTS INDICATE THE AVERAGE FOR A FEW DAYS AND THE VERTICAL LINES IN THE SCATTERING OF INDIVIDUAL OBSERVATIONS ABOUT THE MEAN

decrease with time as the reversal period is approached associated with a decrease in amplitude. These show the characteristic features of type II spectra generated through crossfield instability mechanism.

(2) The reversal period, like the morning transition period, is characterised by a complete disappearance of the echo.

(3) The spectra observed after the reversal also are broad and show type II characteristics. The positive doppler shift indicates that the irregularities move from west to east.

(4) The amplitude and peak doppler shift of the spectra show an occasional increase and then resumes the decreasing trend before it vanishes during the evening reversal.

The drift in the region of generation of irregularities of maximum amplitude, as indicated by a shift in height of the echo peak, associated with the spectral variations during the evening hours, is shown in figure (4.4).

The average height variation of the radar echo peak for a few evening observations is shown in the figure by a smooth curve. The dots indicate the average values of the altitude observations and the vertical bars indicate the scatter of individual observations about the mean .

Generally there exists an upward shift in the peak of the echo, as the reversal period is approached either from the pre-reversal side or the post-reversal side. The region of generation of irregularities are, therefore, higher during periods close to the reversal, than during periods much before and after the reversal.

#### 4.3 Discussion of results

A comparative study of the morning and evening spectral variations and the associated time variations in the region of generation of irregularities of maximum amplitude, reveal the nature of the electric fields existing during these periods and the instability mechanisms responsible for the generation of ionisation irregularities in the electrojet during these periods.

##### 4.3.1 Morning and evening electric fields

The type I spectra observed before the reversal during the morning hours are caused by irregularities generated by the two-stream instability mechanism. This indicates high drift velocity of the electrons, exceeding the ion acoustic velocity. The existence of such large velocities during these periods, must be due to large electric fields prevailing in the electrojet region. These large electric fields are confined to periods before the reversal. The type I spectra observed during these periods, in general, vanish without showing type II spectra during its decay



phase. This is an indication of the absence of sufficiently strong downward gradients in electron density required for the generation of type II irregularities through the cross-field instability mechanism. Type II spectra become dominant after the reversal indicating irregularities moving with phase velocities of the order of few tens of meters. The electron drift velocity is close to the phase velocity of type II irregularities (Balsley 1967). Hence, the low phase velocity of type II irregularities observed during the post-reversal period indicates comparatively lower electric fields during these periods.

The spectra observed during the evening hours before and after the electrojet reversal have typical characteristics of type II spectra as pointed out earlier. The low drift velocity of electrons, as indicated by the spectra show the magnitude of the electric fields existing during these periods. A decrease in the drift velocity of electrons as the reversal period is approached and an occasional increase observed in it just before the reversal show that the electric fields before the evening reversal are comparatively stronger.

Thus the time variations in the echo amplitude and the spectral features during the morning and evening hours show the existence of comparatively larger electric fields before the reversal of the electrojet currents, both during morning and evening hours. In this context, it will be worthwhile to quote the results obtained by Balsley from

back scatter studies at Jicamarca, Peru, during the period 1967-70. Figures (4.5) and (4.6) show the average variation of the drift velocity of electrons from 08 hrs. to 08 hrs. the next day, computed from the results of Balsley (U&G Report 1971) for a few days. The existence of comparatively high drift velocities of electrons from west to east during the morning pre-reversal periods, and from east to west during the evening pre-reversal periods, can be seen in the figures.

#### 4.3.2 Vertical shift in the region of the electric fields

The region of generation of type I irregularities being mainly controlled by the drift velocity of electrons with respect to the ions in the region, which in turn depends on the electric fields and the conductivity parameters, is an indication of the region of electric fields. In the case of type II spectra produced by non-two-stream irregularities electric fields have an equally important role. Crossfield instability mechanism, shown to be a source of irregularities of scale sizes in the range 1-300 meters in the electrojet region (Prakash et al, 1971, 1972) confined to regions where the electron density gradients and the electric fields are in the same direction. The amplitude of these irregularities is dependent on the magnitude of electric fields and the electron density gradients.

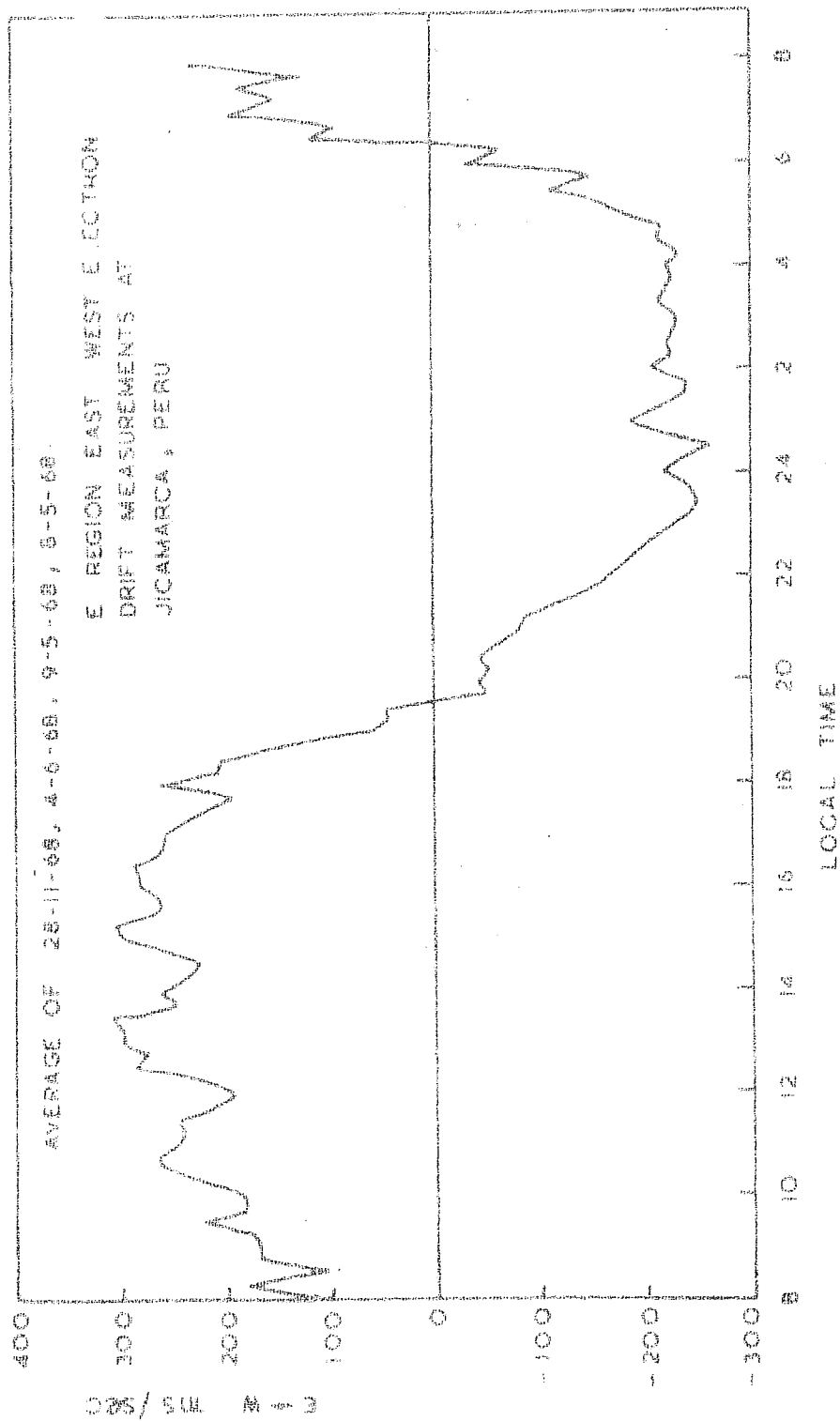


FIG. 4.5: AVERAGE TIME VARIATION OF THE DRIFT VELOCITY  
OF ELECTRONS, JICAMARCA, PERU.

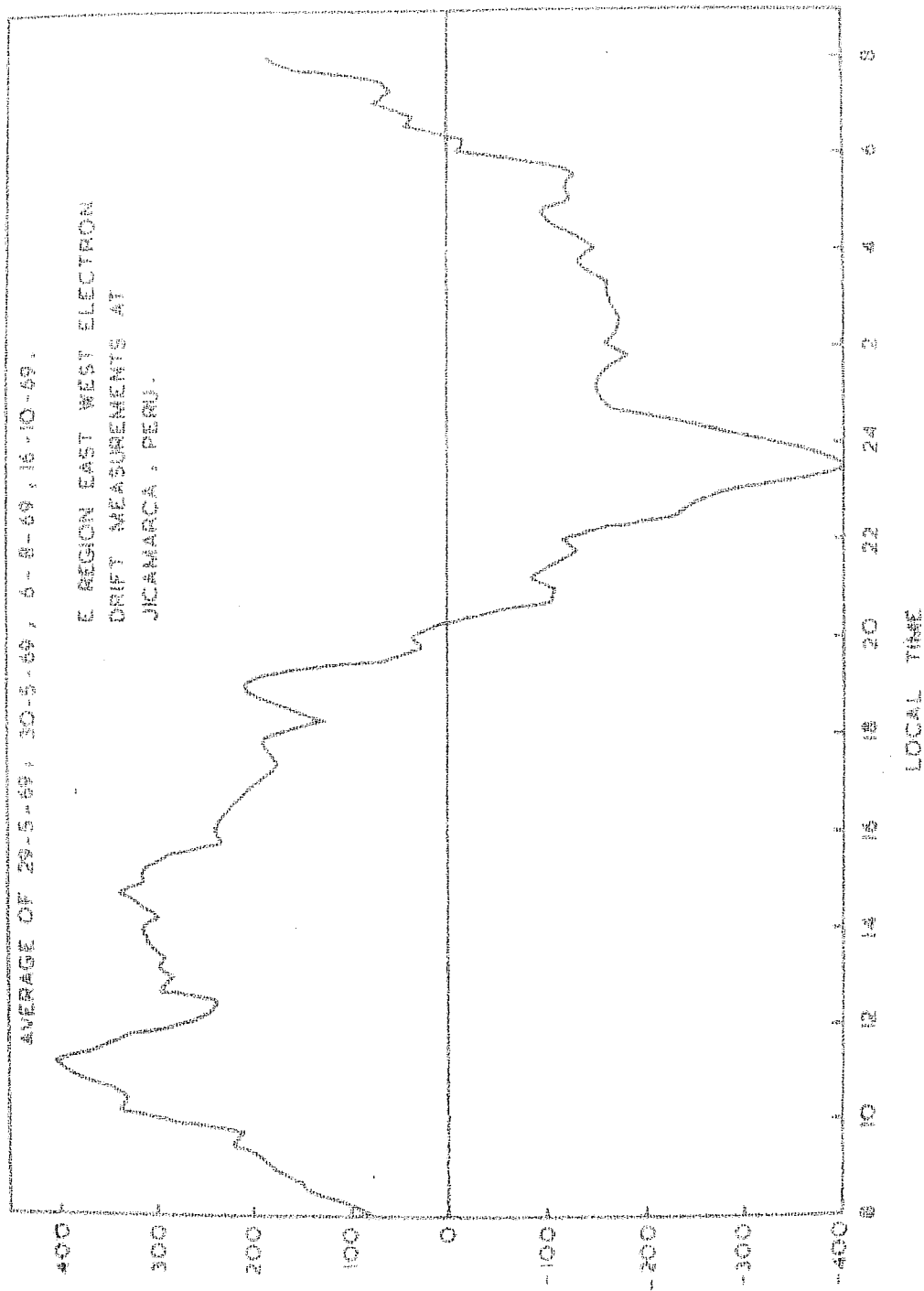


FIG. 4.6: AVERAGE TIME VARIATION OF THE DRIFT VELOCITY  
OF E REGION EAST WEST ELECTRON DRIFT MEASUREMENTS AT  
JICAMARCA, PERU.

Considering the altitude variation of the echo peak during the morning hours, an upward shift in the echo peak as the reversal period is approached, either from the pre-reversal or the post-reversal side, indicates a corresponding shift in the region of the electric fields. In the case of type I irregularities observed before the reversal, such a peak shift can be directly attributed to a shift in the region of electric field, while in the case of type II irregularities observed after the reversal a peak shift in the echo can be due to either a shift in the electron density gradients, or in the region of electric fields or in both. The phenomenon being associated with only a short time duration and the observed shift in the altitude being about 4 to 5 kms, the possibility of a shift in the regions of electron density gradients can be ruled out. A higher altitude of the region of generation of irregularities at times close to the electrojet reversal during the morning hours can, therefore, be taken to be an indication of the region of electric fields being at higher altitudes during this period.

A similar phenomenon is associated with evening hours, close to the electrojet reversal. The type II irregularities observed are associated with higher regions of generation, during the periods close to the reversal. This is indicated by an upward drift in the echo peak, as the reversal period is approached. The shift in the peak being a fast occurring phenomenon, can be attributed to a shift in the region of

the electric fields, rather than a shift in the region of maximum electron density gradients. The electric fields, hence, seem to be confined to higher altitudes during periods close to the reversal of currents.

Similar features regarding the upward shift of the region of electric fields observed during morning and evening hours associated with the reversal of electrojet currents indicate that the sources of primary electrostatic fields are at higher altitudes or transmitted to the equatorial E-region through higher altitudes. These fields drive the electrojet currents. The absence of radar echoes during the electrojet reversal for a period of about half an hour, prevents one from knowing the exact nature of the fields during these periods.

The errors involved in the estimate of the drift velocities of electrons from the spectra, in the present case, especially during periods of low drift velocities and in the estimate of the height shift in the echo peak during the weak echo periods considered here, put a limit to the accuracy of the quantitative estimates that can be made. Therefore, the results are discussed only qualitatively. The observational errors are eliminated to a large extent by taking the average parameters for a number of days selected at random.

Conclusions

(1) The electric fields in the electrojet region are comparatively stronger before the reversal periods of the electrojet currents both during morning and evening hours.

(2) The region of the electric fields are higher in altitude, at times close to the reversal of the currents during morning and evening hours. This indicates the possible existence of electric field sources at higher altitudes or conveyed through higher altitudes to the equatorial E-region.

## C H A P T E R - V

### Ionisation Irregularities in the Counter electrojet

#### 5.1 Introduction

##### 5.1.1 Counter electrojet

Time variations in the geomagnetic field parameters at the ground level are mainly due to the ionospheric and magnetospheric currents. The average pattern of the diurnal variation of the H component of the geomagnetic field on quiet days at equator shows an increase starting at about 06 hrs. (L.T.), a maximum at about 11 hrs. and a decrease to zero level by about 17 hrs. which continues till about 06 hrs. next day (Chapman and Bartels, 1940). However, a study of the day-to-day variations in H, indicated the existence of days, when the behaviour of the geomagnetic field component H, showed large departures from the normal one. In particular, a negative effect, viz., drop of the H values below the night time level was observed on certain days (Gouin, 1962). Gouin and Mayaud (1967, 1969) named the phenomenon as counter electrojet, examined its global extent, and concluded that it arose from reverse E-region currents having return-paths at mid latitudes.

A complete disappearance of the q-type of sporadic E (Esq) during counter electrojet periods was reported by Cohen et al. (1962) from a study of the ionogram traces. Esq has been shown to be associated with the ionisation irregularities in E-region and its disappearance during the



the counter electrojet periods, hence, indicates the disappearance of ionisation irregularities, as shown by the ionogram traces.

The Esq observed in the ionograms correspond to irregularities of scale sizes ranging from a few meters to a few hundred meters. As the generation of these irregularities is controlled by the ambient physical parameters like electric fields, and the electron density gradients, the reversal in the normal current flow, during counter electrojet periods can cause drastic changes in the generation of these irregularities. Generation of irregularities of scale sizes in the range of 1-300 meters by the crossfield instability mechanism has been well established by in-situ measurements of the electron density fluctuations using rocket-borne Langmuir probes (Prakash et al. 1971 a, b). Irregularities of scale sizes in this range are generated by the crossfield instability mechanism in height regions where the gradients in electron density are in the same direction as the ambient electric fields. During day time, as the Hall polarisation field is upwards, these irregularities are observed at those height regions where the electron density gradients are upwards. During night time as the Hall polarisation field is generally downwards, these irregularities are observed at regions where the electron density gradients are downwards. During counter electrojet periods, the reversal of currents during day time, indicates the presence of downward Hall polarisation fields.

The generation of ionisation irregularities by crossfield instability mechanism will then be confined to those height regions (if they exist) where the electron density gradients are downwards. Thus a complete disappearance of the Esq traces in the ionograms, as reported by Cohen (1962), can be either attributed to the absence of sufficiently strong electric fields or to the absence of downward gradients in the electron density. Using the spaced receiver technique Rastogi et al. (1971) showed that during counter electrojet periods, the east-west drifts of electrons in the E-region get reversed, indicating that the westward electric fields can be sufficiently strong. Hence, the disappearance of Esq traces in the ionograms can be attributed to the absence of downward gradients in the electron density.

#### 5.1.2 Present studies

The present studies show that irregularities of scale size about 3 meters, with low amplitudes, can exist during the counter electrojet periods. Such irregularities, though weak in amplitude, were observed on a few occasions during the radar studies. These echoes, are of significant importance as regards the instability mechanisms operating during the counter electrojet periods. A detailed study of the time variations of these echoes, along with the variations in the geomagnetic H component were made with the following objectives:

- (1) To study the nature of the irregularities during the counter electrojet periods,
- (2) To know the criteria behind the generation of irregularities during counter electrojet periods.

## 5.2 Observations and results

### 5.2.1 Radar echoes during counter electrojet periods

Though observations of the radar echo have been made on a number of counter electrojet days, on most of these occasions, the echo was seen to be absent during the counter electrojet periods. On a few occasions, weak echoes were observed during these periods and such results are presented here.

Information regarding the existence of counter electrojet currents on a particular day was obtained from a study of the variations in the H component of the geomagnetic field at the ground level. The H values at an equatorial station and at a station outside the influence of the electrojet currents are used for this purpose.  $H_T$  and  $H_A$  represent these values for Thumba and Alibag respectively. The computation of  $\Delta H_T$  and  $\Delta (H_T - H_A)$  is discussed in detail in section (6.2). In general, as pointed out earlier, the counter electrojet period is characterised by a decrease in both  $\Delta H_T$  and  $\Delta (H_T - H_A)$  below their night time base levels. But on a few days it was observed that though  $\Delta (H_T - H_A)$  showed a considerable decrease below the base level  $\Delta H_T$

did not become negative during the counter electrojet period; but showed only a decrease in its value during the period. The significance of these observations will be discussed later in section (5.3.1). Those days when  $\Delta(H_T - H_A)$  shows a decrease below the base level with  $\Delta H_T$  showing at least a decrease associated with it and when S vanishes during some stage of this depression in  $\Delta H_T$  are taken to be counter electrojet days.

Figure (5.1) shows the variation of the amplitudes of the radar echo on a typical counter electrojet day. In this figure  $\Delta H_T$  and  $\Delta(H_T - H_A)$  values are also plotted along with S for comparison. The radar echo starts decreasing with a decrease in the day time values of  $\Delta H_T$  and  $\Delta(H_T - H_A)$ . With further decrease in the above parameters the echo vanishes and continues to be absent during the counter electrojet period. Though  $\Delta(H_T - H_A)$  and  $\Delta H_T$  parameters are used to know whether counter electrojet exists on a day or not, once the presence is confirmed, the S parameter is made use of in determining the duration of the counter electrojet. This eliminates the errors involved in taking the average Sq variations at Alibag, and correcting the computed  $\Delta(H_T - H_A)$  values in order to obtain a parameter which will represent the electrojet currents. S as an index of the electrojet currents is discussed in detail in Chapter VI of this thesis. The time at which the echo vanishes indicates approximately the onset

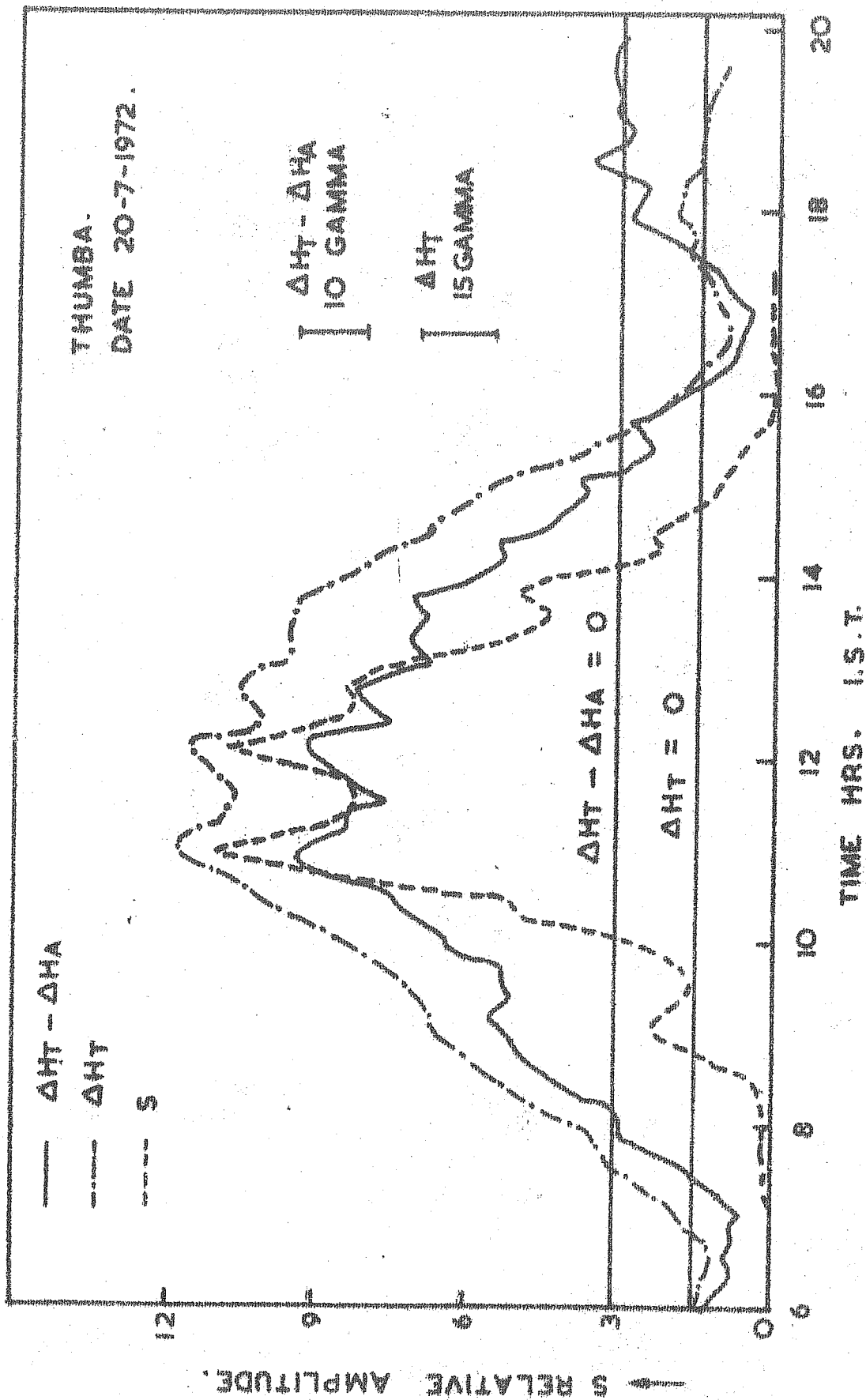


FIG. 5.01

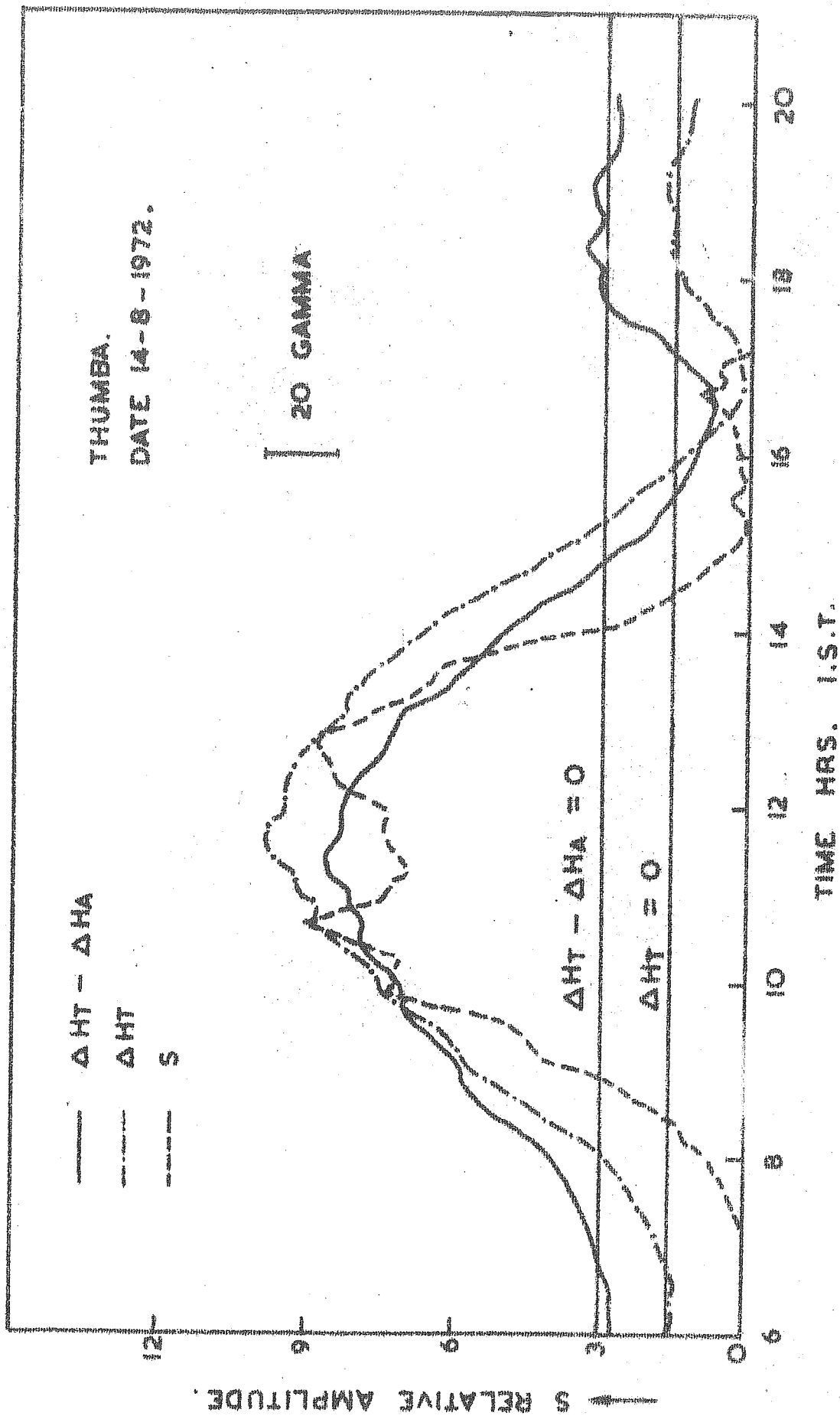


FIG. 5-02a

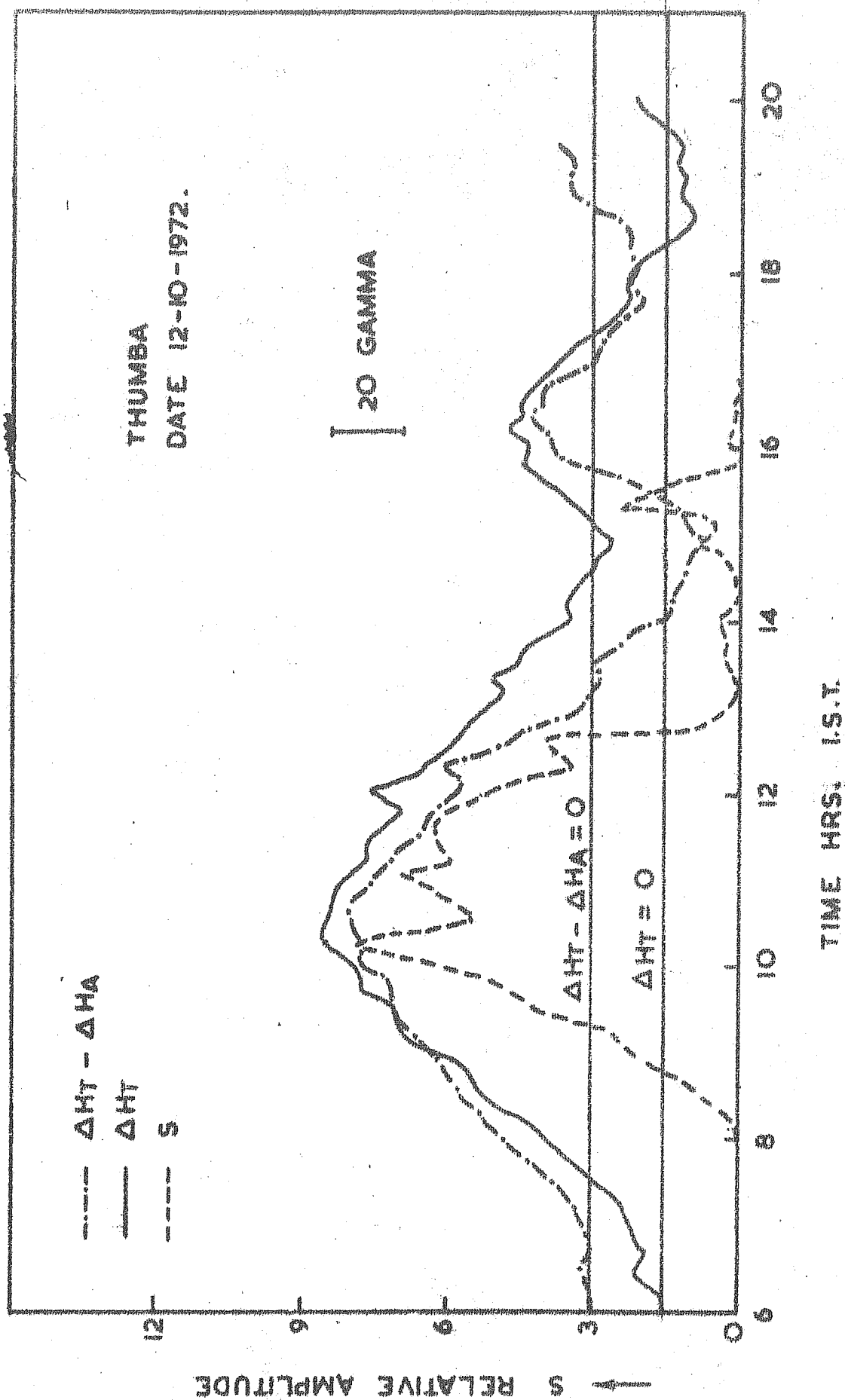


FIG. 5.02b

of the reversal in currents in the electrojet region. The value of  $\Delta (H_T - H_A)$  corresponding to this time is taken to be the reference value. The time at which the  $\Delta (H_T - H_A)$  value rises again to the initial reference level, is assumed to be the end of the counter electrojet period.  $\Delta H_C \text{ max}$  indicates the difference between the minimum  $\Delta (H_T - H_A)$  attained during the counter electrojet period and the reference  $\Delta (H_T - H_A)$  value corresponding to the onset of the counter electrojet. This is a measure of the strength of the counter electrojet currents.

There were a few days when the radar echo was present during the counter electrojet period. Figures (5.2a) and (5.2b) show the variations in the radar echo,  $\Delta H_T$  and  $\Delta (H_T - H_A)$  for two such days. On both these days, the day time reversal in the electrojet currents had occurred during the afternoon hours. The line drawn parallel to the X axis indicates the zero level for  $\Delta (H_T - H_A)$ . The echo vanishes before  $\Delta (H_T - H_A)$  becomes zero and continues to be absent for a long time till  $\Delta (H_T - H_A)$  becomes sufficiently large in the negative direction. The echo S, then, starts again and as  $\Delta (H_T - H_A)$  approaches the zero value, S also decreases and reduces to zero before  $\Delta (H_T - H_A)$  reduces to zero. Table (5.1) shows the list of days when radar echoes were not observed during the counter electrojet periods and the table (5.2) shows the list of days when the echoes were present during these periods.



Table 5.1

Date	$I_p$	Reversal period start	end	Occurrence period of radar echo start	end	$\Delta H_C \text{ max}$
8.1.72	4	0620	1010			29
21.1.72	22	0610	0735			8
18.2.72	12	very weak				
27.6.72	17	1335	1600			19
5.7.72	3	very weak				
7.7.72	10	1620	1845			13
11.7.72	6	1510	1715			13
20.7.72	5	0530	0750			10
		1555	1755			12
21.7.72	3	1440	1635			7
12.8.72	7	1505	1635			8
16.8.72	21	1515	1640			10
6.9.72	10	1340	1505			16
14.12.72	9	1440	1725			9
6.1.73	20	1600	1655			7
19.1.73	10	1340	1500			10
8.2.73	25	1425	1630			23
1.3.73	22	1340	1520			5
8.3.73	7	very weak				

Table 5.2

Date	$I_p$	Reversal period start	end	Occurrence period of radar echo start	end	$\Delta H_C \text{ max}$
14.8.72	9	1505	1730	1520	1710	20
12.9.72	5	1200	1455	1315	1450	15
12.10.72	6	1305	1600	1310	1600	32
1.12.72	6	1000	1415	1250	1410	42
22.5.73	20	0605	0905	-	0750	15

Also inserted in the table are  $\Delta H_C \text{ max}$ , the  $I_p$  index, the times of onset and vanishing of the counter electrojet and the period of occurrence of the radar echo.

#### 5.2.2 Occurrence periods of counter electrojet

Radar studies of the occurrence periods of counter electrojet confirm the results of Gouin and Mayaud (1967, 1969) and Rastogi et al. (1971) and show that the morning hours and the late afternoon hours are most favourable for the occurrence of counter electrojet. When a comparative study of the morning and evening occurrences was made, the evening occurrences were seen to be more in number than the morning occurrences. Out of the total 23 counter electrojet observations made by the radar during the period January 1972 to May 1973, 4 days showed only morning time occurrences, 18 days showed only evening time occurrences and the remaining one day showed both morning and evening time occurrences. Out of the 23 days of observations, back scatter echoes, though weak, were observed only on 5 days and 4 of these observations were confined to the counter electrojets occurring late in the afternoon hours and one to the morning hours.

When a comparative study of the number of counter electrojet occurrences with the solar  $I_p$  index is made, quiet days were found to be more favourable for the occurrences of counter electrojet. Out of the 23 occurrences, 10 were on quiet days ( $I_p \leq 8$ ) 6 were on moderately disturbed

days ( $8 < I_p \leq 15$ ) and the remaining 7 days were on rather highly disturbed days. Those days where a number of reversals occur during the day time were excluded from the present studies due to the complexity of the phenomenon involved.

### 5.2.3 Summary of results

A close examination of the figures (5.2a) and (b) and the tables (5.1) and (5.2) shows the following main features associated with the generation of ionisation irregularities during the counter electrojet periods.

There exist days when the counter electrojet period is characterised by a reversal in only  $\Delta (H_T - H_A)$  but not  $\Delta H_T$ .  $\Delta H_T$  on such days shows only a depression during the counter electrojet period.

(1) The radar echo is observed only after the reversed currents have become sufficiently strong and sufficient time has lapsed after the onset of the reversal.

(2) The echo continues for a longer period during the decay phase of the counter electrojet than during its development phase. In other words, equally strong currents during the development and decay phases of the electrojet, do not correspond to equally strong radar echoes; the echo during the decay phase, in general, being stronger. A shift in the occurrence period of the echo towards the end of the occurrence period of the counter electrojet is observed.

(3) The number of occurrences of counter electrojet is seen to be more on quiet days than on disturbed days.

### 5.3 Discussion of results.

#### 5.3.1 Existence of currents above the electrojet region

The disappearance of the radar echo, when  $\Delta(H_T - H_A)$  decreases below its night time base value, associated with a decrease in  $\Delta H_T$  is an indication of the current flow being reversed in the electrojet region. On days when the radar echo appears during the counter electrojet period, it is characterised by the property that a decrease in  $\Delta(H_T - H_A)$  during the period, shows an increase in the echo strength, confirming the existence of reversed currents in the electrojet region. But a positive  $\Delta H_T$  during this period, observed on a few days, shows the presence of currents above the electrojet region, which are not reversed. These currents contribute to a positive  $\Delta H_T$ . Evidence for the existence of such currents which are uncorrelated with the electrojet region has been obtained from a comparative study of the variations in the radar echo amplitude and  $\Delta H_T$  (Section 6.3.3). But the poor conductivity of the medium above the electrojet region, as computed using the available formulae, and the published atmosphere models remains a barrier, in explaining the existence of such currents.

### 5.3.2 Generation mechanisms of irregularities in the counter electrojet

Rocket-borne experiments for the measurement of electron density and its spatial fluctuations using Langmuir probes (Prakash et al. 1971) have shown that crossfield instability mechanism is responsible for the generation of ionisation irregularities of scale sizes in the range 1-300 meters. These are responsible for the Esq observed in the equatorial ionograms (non-blanketing or transparent type of Es). The observations show that these irregularities are generated in the regions of upward gradients in electron density during day time when the Hall polarisation fields are upwards and in the region of downward gradients during night time when the Hall polarisation fields are downwards. The direction of fields during counter electrojet periods is similar to that of the fields during night times. Hence, downward gradients are necessary to generate irregularities by the crossfield instability mechanism during counter electrojet periods.

One of the rocket flights from Thumba at 1532 hrs. on 17th August 1972, a counter electrojet day, measured the electron density and its spatial fluctuations. Irregularities generated through crossfield instability mechanism were observed in a region of downward electron density gradients, confirming the existence of a downward Hall

polarisation field in the electrojet region. These observations by Prakash et al. (1974) establish the possibility of generation of electron density irregularities of few metre scale sizes, during counter electrojet periods, in support of the present radar observations. The reversed electric fields if strong enough can generate downward gradients in electron density, necessary for the generation of type II irregularities.

The initial phase of the counter electrojet is associated with a downward drift of plasma because of the reversed Hall polarisation fields. As the plasma is transported downwards, the ions with larger recombination coefficients are lost. This causes an accumulation of metallic ions with smaller recombination coefficient and results in the formation of an ionisation layer. The formation of such a layer having downward gradients in electron density will depend on the magnitude of the electric field and its duration. Hence, during the initial phase of the counter electrojet, there will be no downward gradients in the electron density. After a certain interval of time, when the reversed currents become stronger, such downward gradients develop. Once the layer is formed a smaller field will be sufficient to maintain it. As the amplitude of the irregularities generated is dependent on the magnitude of the electron density gradients the radar echoes will be observed with a time delay, between the onset of the counter electrojet and the appearance of the echo.

Since, as pointed out earlier, a smaller field is sufficient to maintain the gradients in electron density in the newly formed layer during the decay phase of the counter electrojet, negative gradients in electron density will continue to exist for a long time. This results in the continued existence of the radar echo for a longer time during the decay phase of the counter electrojet, than during the development phase. Equal electric fields during the development and decay phases of the counter electrojet, do not give rise to equal amplitudes of the radar echoes, since the conditions during the decay phase are more favourable for the generation of irregularities by the crossfield instability mechanism.

Studies of ionogram traces on a counter electrojet day, show the development of strongly blanketing type of Es, sometimes causing a number of multiple reflections in the ionogram traces; with  $f_b$  Es becoming as large as 7 to 8 MHz. But on such occasions when it is very strong, there exists a frequency beyond which the Es becomes transparent. The existence of both blanketing and non-blanketing (or transparent) type of Es, during the flight period (1532 hrs.) on the counter electrojet day (17th August, 1972) has been reported by Prakash et al. (1974). Part of the observed Es was non-blanketing above about 7 MHz; indicating the presence of small scale irregularities during these periods.

### Conclusions

(1) Observations of back scatter radar echoes during counter electrojet periods show that ionisation irregularities of a few metre scale sizes are generated only on those days when the counter electrojet currents are strong and are extended over long periods. Rocket observations show that the small scale irregularities observed during the counter electrojet periods are generated at regions of downward electron density gradients, through the crossfield instability mechanism. Extended and strong counter electrojet are associated with a downward drift of plasma giving rise to an ionisation layer with downward electron density gradients.

(2) Counter electrojet days, with extended and strong reversals, are more favourable for the generation of irregularities during the counter electrojet period, by the cross-field instability mechanisms.

(3) The reversed currents in the electrojet region may be associated with currents which are not reversed, existing above the electrojet region.



## C H A P T E R - VI

### MORPHOLOGY OF ELECTROJET CURRENTS OVER INDIAN ZONE

#### 6.1 Radar echo and the geomagnetic field variations

The study of the electrojet current system has been mainly through an analysis of the ground level variations in the geomagnetic field parameters. With the advent of the VHF radar technique for the investigation of ionisation irregularities, the study of physical parameters responsible for the generation of irregularities, embedded in the electrojet region, has become possible. The generation mechanism of these irregularities and the role of the ambient physical parameters in their generation are discussed in detail in section (1.3.1). A comparative study of the time variations in the amplitude of the radar echo and the ground level variations in the H component of the geomagnetic field at an equatorial station disclosed a close relationship existing between the two parameters (Cohen and Bowles, 1963a). However, even on quiet days, when S and H generally show smooth time variations, the existence of a 'hysteresis' sort of loop was found in S versus  $\Delta H$  (deviations of H values from a properly selected base level) curve. This assymmetric deviation from a linear relationship was

attributed to variations in H due to currents flowing in the exosphere, by Cohen. He reported that the hysteresis loop collapsed into a single line when the exospheric contributions were removed from the H variations at Huancayo, Peru (Located beneath the electrojet) by subtracting H variations observed at Bogota, Colombia (located well outside the electrojet region).

The results of the present studies carried out during the period 1971-74, at Thumba not only establish the existence of a general linear relationship between S and H variations at Thumba (an equatorial station), but also show that the earlier conclusions regarding the exact nature of this relationship are to be modified in order to explain the observed feature of the time variations in S and H. Hourly moving averages of S and H were used during the present studies in order to eliminate the short time effects in their variation.

## 6.2 Reduction of magnetograms and analysis of data

$H_T$  represents the horizontal component of the geomagnetic field at Thumba and  $H_A$  at a mid latitude station Alibag, where the influence of the electrojet currents is negligible. Values of  $H_T$  and  $H_A$  from 00 hrs. to 24 hrs. at intervals of five minutes were used to calculate the hourly moving averages during the present studies.

Taking into account the various sources that contribute to the time variations in the horizontal components of the geomagnetic field,  $H_T$  and  $H_A$  can be written in the following form:

$$H_T = H_{OT} + \Delta H_{MT} + \Delta H_{ET} + \Delta H_{FT} \quad (6.1)$$

$$H_A = H_{OA} + \Delta H_{MA} + \Delta H_{sqA} + \Delta H_{FA} \quad (6.2)$$

where

$H_{OT}$  and  $H_{OA}$  are the horizontal components of the earth's main field.

$\Delta H_{MT}$  and  $\Delta H_{MA}$  are the contributions due to magnetospheric currents.

$\Delta H_{ET}$  is the contribution due to electrojet currents.

$\Delta H_{FT}$  and  $\Delta H_{FA}$  are the contributions due to currents above the electrojet region.

$\Delta H_{sqA}$  is the contribution due to Sq currents.

The time variation in the magnetospheric currents on a geomagnetically quiet day is only of the order of a few gammas, and hence does not contribute much to the variations in  $H_T$ . If the value of  $H_{OT} + \Delta H_{MT}$  can be estimated somehow, the equation (6.1) itself can be used to obtain an approximate estimate of  $(\Delta H_{ET} + \Delta H_{FT})$  which represents the overhead currents as seen from Thumba.

The procedure adopted in the estimation of  $H_{OT} + \Delta H_{MT}$ , during the present studies is the following. From the back scatter studies it has been found (Balsley 1966) that the horizontal drifts of electrons in the E region and the vertical drifts in the F region show a reversal during the early morning and the late evening hours. Hence the electrojet currents and the electrostatic fields will be very small during these periods. Assuming that the currents represented by  $\Delta H_{ET}$  and  $\Delta H_{FT}$  are negligible during periods close to the morning and evening electrojet reversals, the values of  $H_T$  are equal to  $(H_{OT} + \Delta H_{MT})$  values during these periods. Linear extrapolation of these values is used to calculate the values of this parameter at other times of the day.  $H_{OT} + \Delta H_{MT}$  values thus calculated form the base line for computing the contribution due to overhead currents and are subtracted from the observed  $H_T$  values given by equation 6.1. This leads to the equation

$$\Delta H_T = \Delta H_{ET} + \Delta H_{FT} \quad (6.3a)$$

The term  $\Delta H_{FT}$  contains a part which is related to  $\Delta H_{ET}$  and another part which is not related to it. Using the super scripts r and u to represent these components, one can write

$$\Delta H_T = \Delta H_{ET} + \Delta H_{FT}^r + \Delta H_{FT}^u \quad (6.3)$$

similarly for Alibag

$$\Delta H_A = \Delta H_{sqA}^r + \Delta H_{sqA}^u + \Delta H_{FA}^r + \Delta H_{FA}^u \quad (6.4)$$

where  $\Delta H_{sqA}^r$  and  $\Delta H_{FA}^r$  are the components of  $\Delta H_{sqA}$  and  $\Delta H_{FA}$  which are related to  $\Delta H_{ET}$  and  $\Delta H_{sqA}^u$  and  $\Delta H_{FA}^u$  are the components which are not related to it. From equations (6.3) and (6.4) one can write {here  $\Delta (H_T - H_A)$  is equal to  $\Delta H_T - \Delta H_A$  since the same hours are selected for both  $H_T$  and  $H_A$  in the computation of their base lines}.

$$\Delta (H_T - H_A) = \Delta H_{ET} + \Delta H_{FT}^r - \Delta H_{sqA}^r - \Delta H_{FA}^r + (\Delta H_{FT}^u - \Delta H_{sqA}^u - \Delta H_{FA}^u) \quad (6.5)$$

Depending on the relative importance of the different terms in the equations (6.3 and 6.5) one comes across mainly two types of days:

- (i) Days when the value of  $\Delta H_{FT}^u = \Delta H_{FA}^u + \Delta H_{sqA}^u$  on these days, equation (6.5) takes the simple form,

$$\Delta (H_T - H_A) = \Delta H_{ET} - (\Delta H_{FT}^r - \Delta H_{sqA}^r - \Delta H_{FA}^r) \quad (6.6)$$

on such days,  $\Delta (H_T - H_A)$  is a good representation of the variations in the electrojet currents, though not equal in magnitude to it since the second term on the right hand side of the equation is related to the term  $\Delta H_{ET}$ .

At the same time, as shown by equation (6.3)

$H_T$  is not an index of  $\Delta H_{ET}$  due to the additional term  $\Delta H_{FT}^u$  associated with it, which is not related to  $\Delta H_{ET}$ .

THUMBA  
8 JULY 1971  
Ap = 8

S  
 $\Delta H_T - \Delta H_A$   
 $\Delta H_T$

S RELATIVE AMPLITUDE

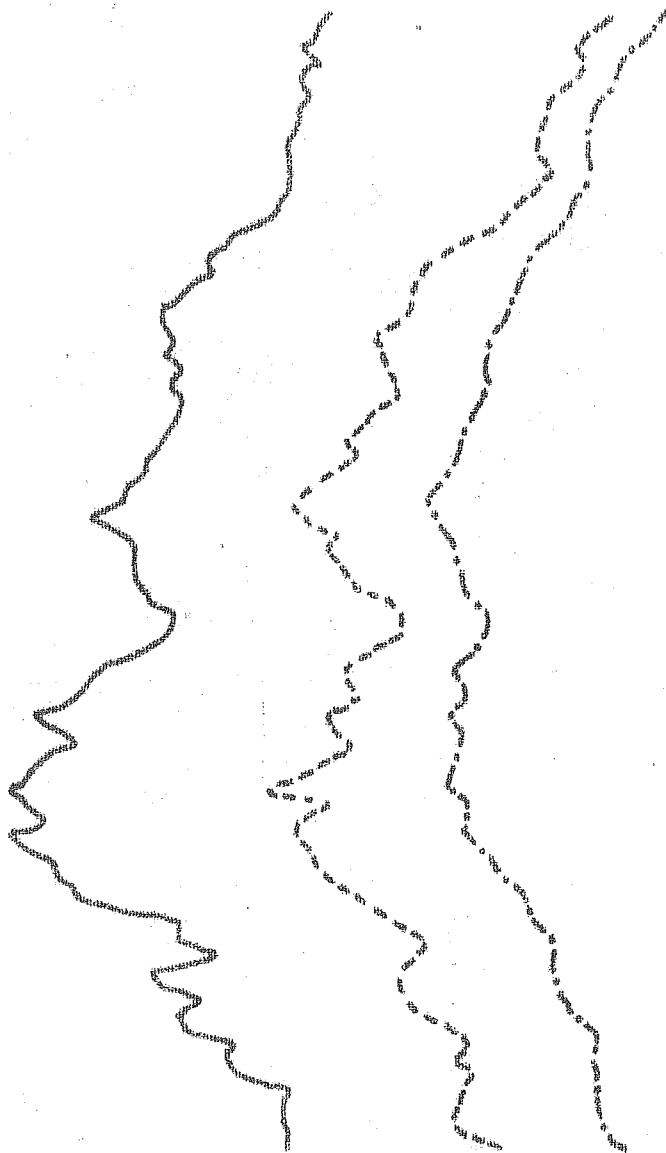
$\Delta H_T$  IN GAMMAS

$\Delta H_T - \Delta H_A$  IN GAMMAS

08 09 10 11 12 13 14 15 16

TIME HRS (I.S.T)

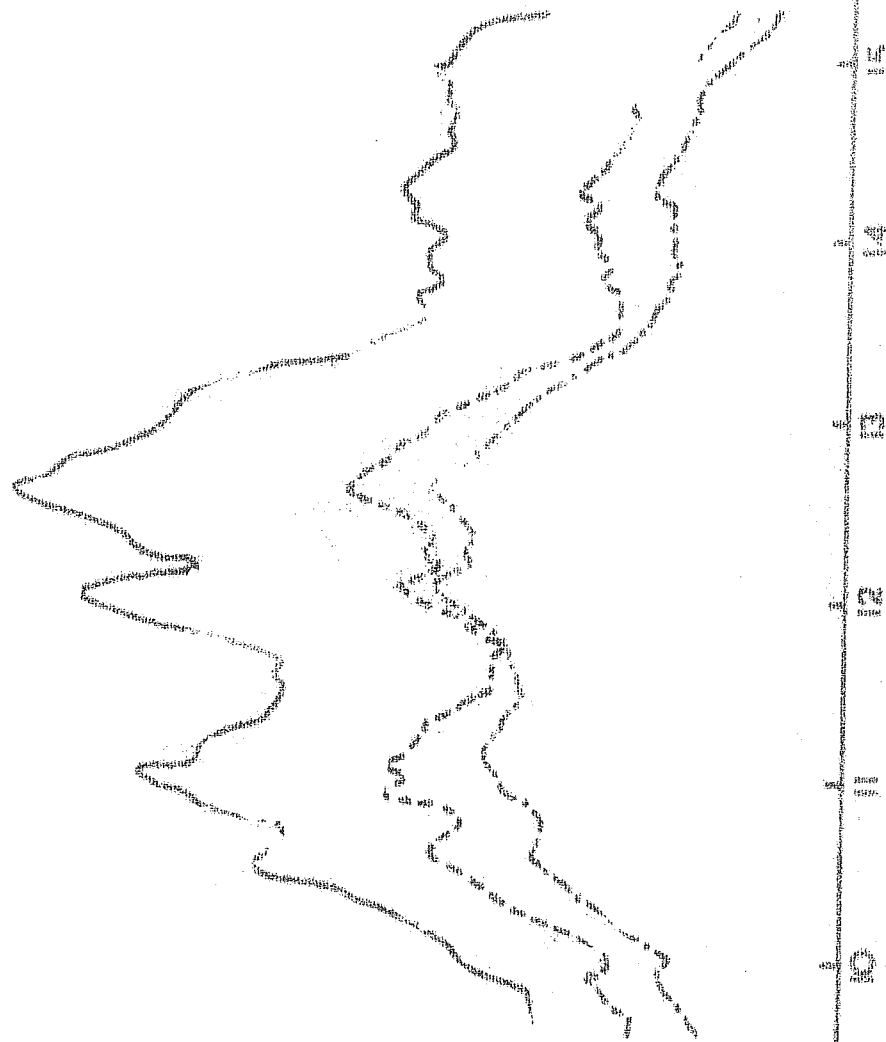
FIG.- 6.01C



THURSDA  
12 JULY 1971  
AP-9

— S  
— AHT-AHA  
— AHT

RELATIVE AMPLITUDE



AHT - AHA IN GAMMAS

AHT IN GAMMAS

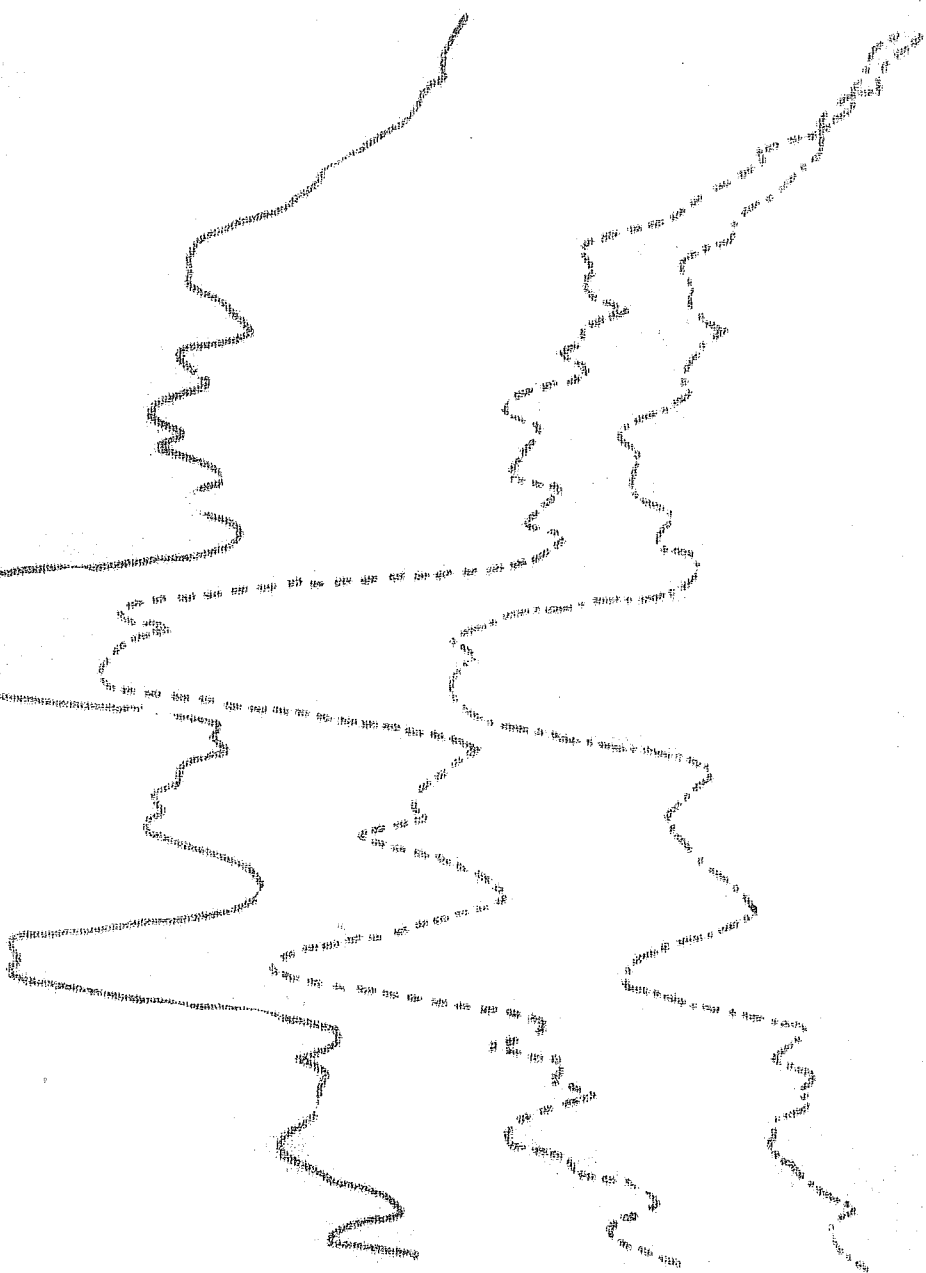
TIME HRS (A.S.T.)

FIG. - 6.01b

[illegible]

2017 MAR 20 2017 MAR 20

# SECRET





- (ii) Days when  $\Delta H_{ET}^u \neq \Delta H_{FA}^u + \Delta H_{sqA}^u$ .

Large number of the days come under this category. Under this condition the equation (6.3) has to be used for the study of currents in and above the electrojet region. If one of them can be estimated somehow, the time variation of the other can be studied using the equation (6.3). The amplitude of the radar signal 'S' seems to be a useful parameter in the estimation of  $\Delta H_{ET}$ .

### 6.3 Results and discussions

#### 6.3.1 Results

The variation in the amplitude S of the radar echo from 08 hrs. to 16 hrs. for a few days, is shown in figure (6.1). The variations in  $\Delta H_T$  and  $\Delta(H_T - H_A)$  are also shown in the figure for comparison. Figure (6.1a) represents the typical variation in these parameters on a quiet day ( $A_p \leq 8$ ) while figures (6.1b and 6.1c) show the corresponding variations on moderately ( $8 < A_p \leq 15$ ) and highly ( $A_p > 15$ ) disturbed days respectively. In general, there exists a close relationship between these parameters irrespective of the degree of disturbances, as can be seen from these figures. The study of currents above the electrojet region using equation (6.3) is possible only on those days when

time variations in the magnetospheric currents are negligible. Hence the disturbed days were excluded from the present studies.

Figures (6.2 and 6.3) show the variation of  $S$  with  $\Delta H_T$  and  $\Delta(H_T - H_A)$  for a few quiet days. The asymmetric behaviour between forenoon and afternoon variations is quite evident from these plots. A comparative study of the general nature of the curves before and after the subtraction of  $\Delta H_A$  from  $\Delta H_T$  values, indicates the existence of three types of days.

- (i) Days when the hysteresis loop in the  $S$  versus  $\Delta H_T$  plots vanish when  $\Delta H_T$  is replaced by  $\Delta(H_T - H_A)$ . About 15% of the total number of quiet days considered belonged to this group.
- (ii) Days when the hysteresis loop, though does not collapse, shows a tendency to collapse when  $\Delta(H_T - H_A)$  is substituted for  $\Delta H_T$ . About 30% of the total number of days analysed, showed such a tendency to collapse.
- (iii) Days when the portion of the curves representing the forenoon and afternoon hours, get more separated when  $\Delta H_T$  is replaced by  $\Delta(H_T - H_A)$ . About 55% of the days considered belonged to this group.

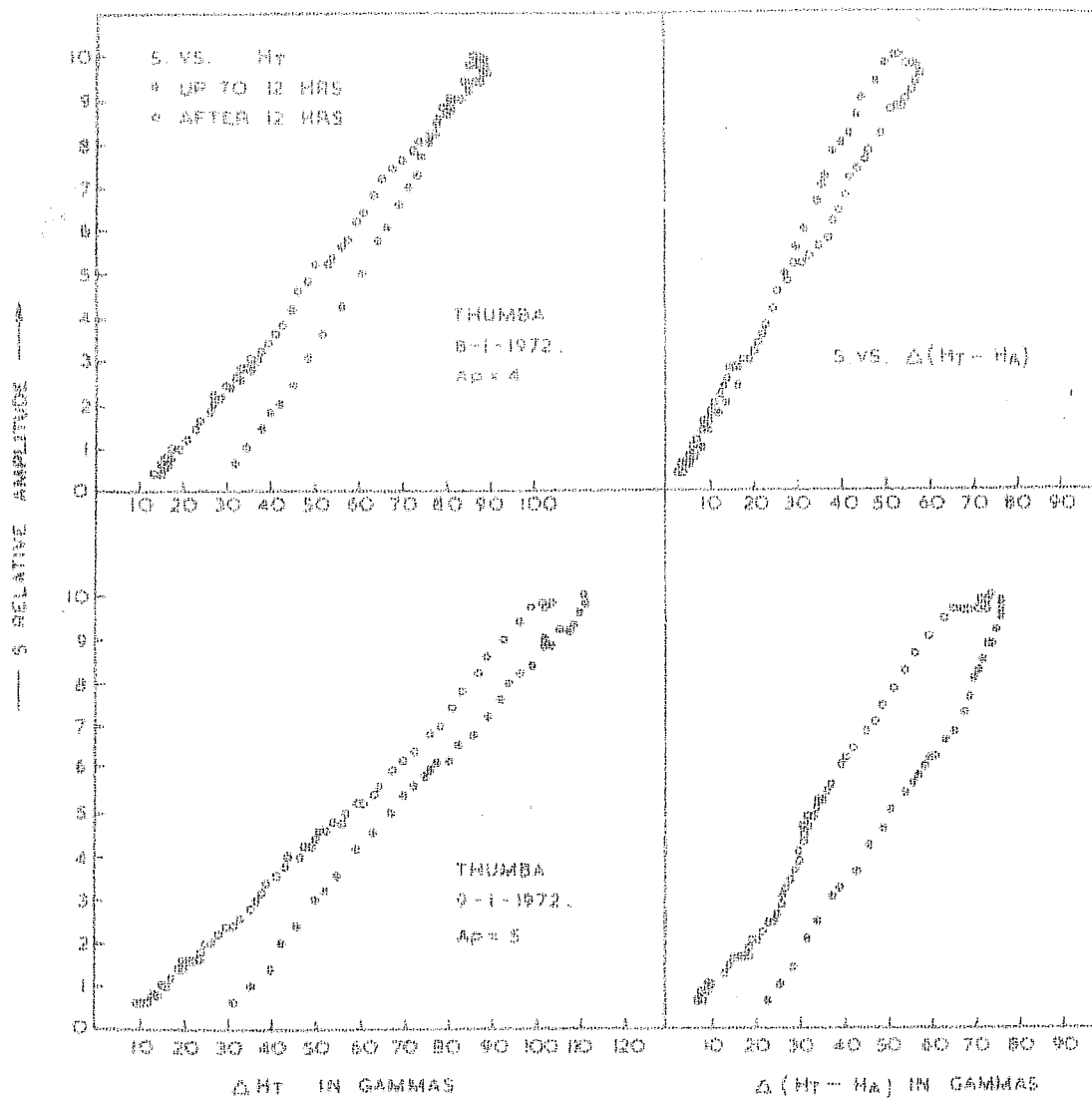


FIG. 6.2: VARIATION OF  $S$  VERSUS  $\Delta H_T$  AND  $\Delta(H_T - H_A)$

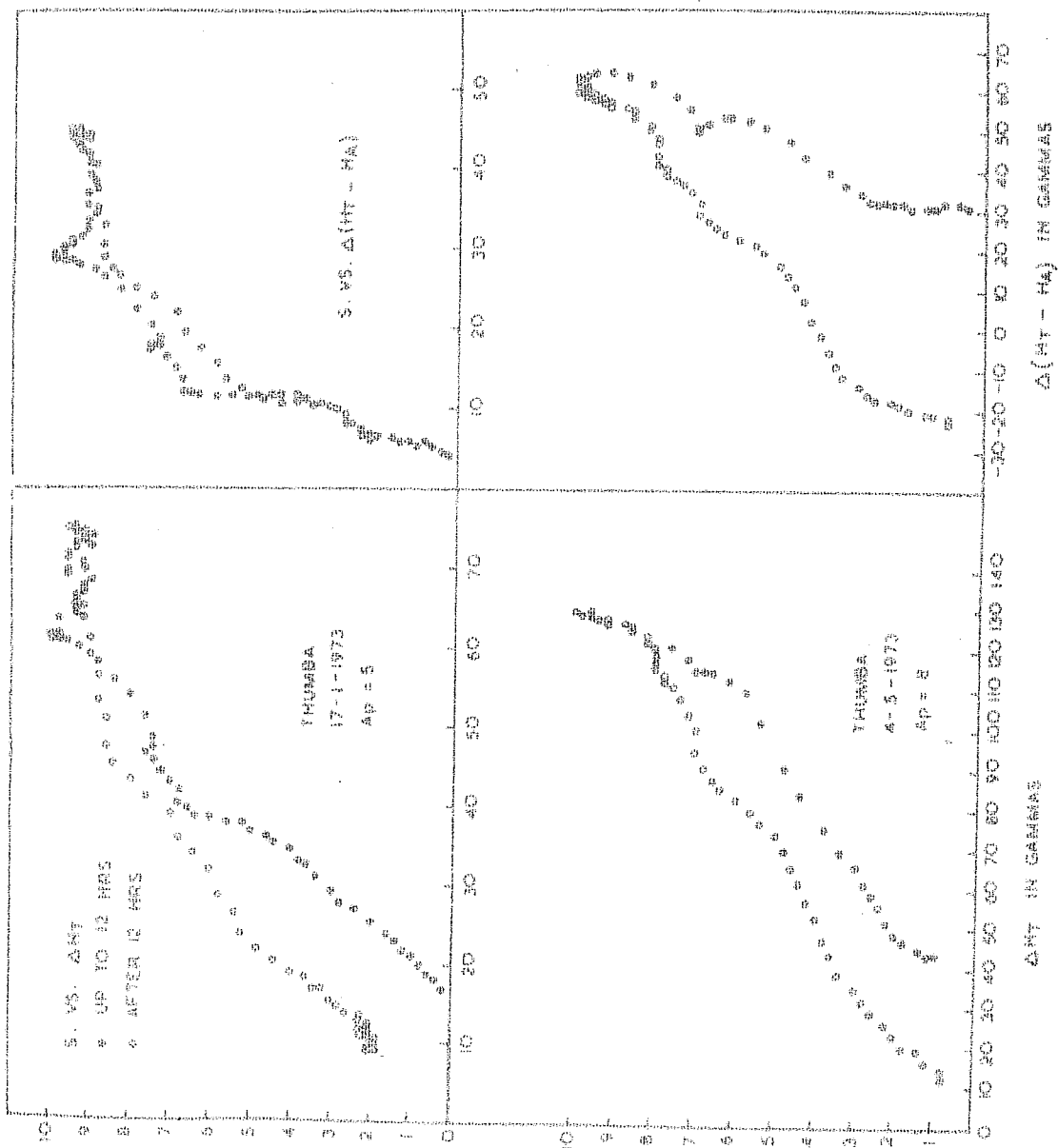


FIG. 6.3: VARIATION OF S VERSUS  $\Delta H_1$  AND  $\Delta H_2$  IN GAMMAS

The  $S$  versus  $\Delta H_T$  and  $\Delta(H_T - H_A)$  plots observed on days belonging to the group (i) above are in conformity with the results reported by Cohen and Bowles (1963a). A general feature that can be observed on most of the quiet days in the  $S$  versus  $\Delta H_T$  and  $\Delta(H_T - H_A)$  plots is that the data can be fitted with two lines one for the forenoon hours and another for the afternoon hours.

### 6.3.2 $S$ as a measure of $\Delta H_{ET}$

The close association between the amplitude of the radar echo and the electrojet currents as shown by a comparative study of the drift velocity of electrons and the power contained in the type II echoes reported by Balsley is discussed in section (1.3.2). The results of Balsley imply a linear relationship between  $S$  and the electrojet currents, at least during periods when the type II irregularities dominate in the electrojet region. The electrostatic fields driving the large scale electrojet currents, have their sources distributed over a wide range of latitudes. Hence, only a slow variation of electrostatic fields with altitude is expected. The electrojet currents are mainly confined to an altitude range of about 90 to 120 km. Hence changes in the currents at any altitude range in the electrojet region can be assumed to be associated with corresponding proportionate changes at other altitude ranges in the electrojet region.

Therefore, the amplitude of the back scatter signal even though is dependent on the irregularities confined only to a portion of the electrojet currents near its peak, it can be assumed to be proportional to the whole of the electrojet currents. As pointed out earlier, a general linear relationship between  $S$  and  $\Delta H_T$ , is observed when the forenoon and afternoon observations are considered separately. During the noon hours when the electrojet currents are at their peak the type I irregularities usually predominate over type II and a deviation from this linear relationship was often observed. Hence, the data for noon hours were not used in the present comparative study of  $S$  and  $\Delta H_T$ .

Another factor which can affect the relationship between  $S$  and  $\Delta H_{ET}$  is the time variation in the generation mechanism of irregularities responsible for the back scatter signal. Type II irregularities are generated through cross field instability mechanism and hence depends on the electron density and its gradients. The electron density and its gradients have a symmetric variation about the noon time while the observed variation in the relationship between  $S$  and  $\Delta H_T$  is assymmetric. Hence, the possibility of variation in electron density and its gradients being responsible for this assymetry can be ruled out.

From the above consideration it looks convincing to use  $S$  as an index of the currents in the electrojet region. This property of  $S$  has been used here in estimating the currents above the electrojet region using equation (6.3).

### 6.3.3 Currents above the electrojet region

$\Delta H_T$  as indicated by equation (6.3) is a measure of total currents in and above the electrojet region. A change in the distribution of the currents in this region will hence reflect in the time variation of  $\Delta H_T$ . As discussed in section (6.3.2) since  $S$  can be assumed to represent the electrojet currents with a certain factor of proportionality, one can rewrite the equation (6.3) as

$$\Delta H_T = \alpha S + \Delta H_{FT}^r + \Delta H_{FT}^u \quad (6.7a)$$

where  $\alpha S$  represents the currents in the electrojet region.  $\alpha$  is a constant dependent on the power of transmission of the radar signal, the antenna gain, the elevation of the antenna beam, and the receiver gain characteristics. Since  $\Delta H_{FT}^r$  is related to the electrojet currents, one can define a new constant  $\beta$  such that

$$\Delta H_T = \beta S + \Delta H_{FT}^u \quad (6.7)$$

$\beta$  is a factor dependent on the relationship between  $\Delta H_{FT}^r$  and  $\Delta H_{ET}$ . As shown by this equation a time variation in  $\Delta H_{FT}^u$  can introduce an asymmetry in the relationship between  $S$  and  $\Delta H_T$ .

As pointed out earlier in section (6.3.1),  $S$  versus  $\Delta H_T$  and  $\Delta(H_T - H_A)$  can be fitted with two lines one for the forenoon hours and another for the afternoon hours. These lines when extrapolated for  $S = 0$ , give intercepts on

the  $\Delta H_T$  or  $\Delta (H_T - H_A)$  axis as the case may be. From equation 6.7 the intercept on the  $\Delta H_T$  axis gives the value of  $\Delta H_{FT}^u$  at the times close to  $S = 0$ . The intercept on the  $\Delta (H_T - H_A)$  axis gives the values of  $\Delta H_{FT}^u - \Delta H_{sqA}^u - \Delta H_{FA}^u$  at times close to  $S = 0$ . For most the days this remnant  $\Delta H_T$  for the forenoon hours is more than its value for the afternoon hours.

Table 6.1

Date	Ap	<u>Intercept of <math>\Delta H_T</math> on <math>S = 0</math> axis</u>	
		Morning	Evening
8.1.72	4	29	14
9.1.72	5	22	8
5.2.72	6	15	15
6.2.72	6	18	-10
9.2.72	4	5	5
6.4.72	8	-	14
20.7.72	5	-	8
21.7.72	3	22	16
31.7.72	6	3	-17
16.8.72	6	15	17
20.12.72	4	18	-13
7.3.73	8	19	21
4.5.73	8	28	-6
<u>Average intercept</u>			
Forenoon		:	17.5 gamma
Afternoon		:	5.5 gamma



Table (6.1) shows the remnant  $\Delta H_T$  values for the forenoon and afternoon hours for a few quiet days. A day to day variation from about 3 to 29 gamma can be seen in the remnant  $\Delta H_T$  during the forenoon hours and -17 to 21 gamma during the afternoon hours. The average value of the intercept is about 17.5 gamma during the forenoon hours and about 5.5 gamma during the afternoon hours.

As pointed out earlier, the remnant  $\Delta H_T$  which is same as  $\Delta H_{FT}^u$  shows the existence of currents additional to the electrojet current. These currents are usually more in the morning than in the evening. On the basis of these currents above the electrojet region, one can account for the hysteresis curves observed in the  $S$  VS  $\Delta H_T$  plots and the changes observed when  $\Delta H_T$  is replaced by  $\Delta(H_T - H_A)$ . From equation (6.5) it can be seen that when the magnitude of  $\Delta H_{FT}^u$  is such that it cancels with the term  $\Delta H_{sqA}^u + \Delta H_{FA}^u$  the hysteresis curve seen in  $S$  versus  $H_T$  plots will collapse into a line, when  $\Delta H_T$  is replaced by  $\Delta(H_T - H_A)$ . The fact that such days exist, though few in number shows that the currents extend to such altitudes above the electrojet region as to cause considerable variations in  $H_A$ . On other days when the terms  $\Delta H_{FT}^u$  and  $(\Delta H_{FA}^u + \Delta H_{sqA}^u)$  do not cancel with one another, the nature of behaviour of the  $S$  versus  $\Delta(H_T - H_A)$  plots cannot be predicted from the behaviour of  $S$  versus  $\Delta H_T$  plots.

Table 6.2

Date	$A_p$	Intercept of $\Delta (H_T - H_A)$ on $S = 0$ axis	
		Morning	Evening
8.1.72	4	0	1
9.1.72	5	15	7
5.2.72	6	2	-10
6.2.72	6	4	-14
9.2.72	4	3	- 8
6.4.72	8	-	- 7
20.7.72	5	3	- 6
21.7.72	3	10	-29
31.7.72	6	4	-11
16.8.72	6	15	2
20.12.72	4	8	- 8
4.5.73	8	24	- 6

Average Intercept

Forenoon : 8.8 gamma

Evening : -7.5 gamma

Table (6.2) shows the remnant  $\Delta(H_T - H_A)$  values for these quiet days, both for forenoon and afternoon hours. A variation in the remnant  $\Delta(H_T - H_A)$  ranging from about 0 to 24 gamma during the forenoon hours and from about -29 to 7 gamma during the afternoon hours was observed on these days. The average value of the intercept is about 8.8 gamma during the forenoon hours and -7.5 gamma during the afternoon hours.

A negative value for afternoon remnant as shown for one of the days in figure (6.3) indicates that the term  $\Delta H_{sqA}^u + \Delta H_{FA}^u$  dominates over the term  $\Delta H_{FT}^u$  at times close to  $S = 0$ . A positive value of the afternoon intercept indicates that  $\Delta H_{FT}^u$  dominates over  $\Delta H_{sqA}^u + \Delta H_{FA}^u$  at times close to  $S = 0$ . About 75% of the days observed shows a negative remnant in  $\Delta(H_T - H_A)$  during the afternoon hours.

#### 6.3.4 Electrostatic fields in the E and F regions

The east-west drift velocities of electrons in the E-region and their vertical velocities in the F-region in the altitude range of 300-400 kms, were estimated from back scatter radar studies at Jicamarca, by Balsley during the period 1968-69. A comparative study of these parameters at Jicamarca showed that the drift velocities

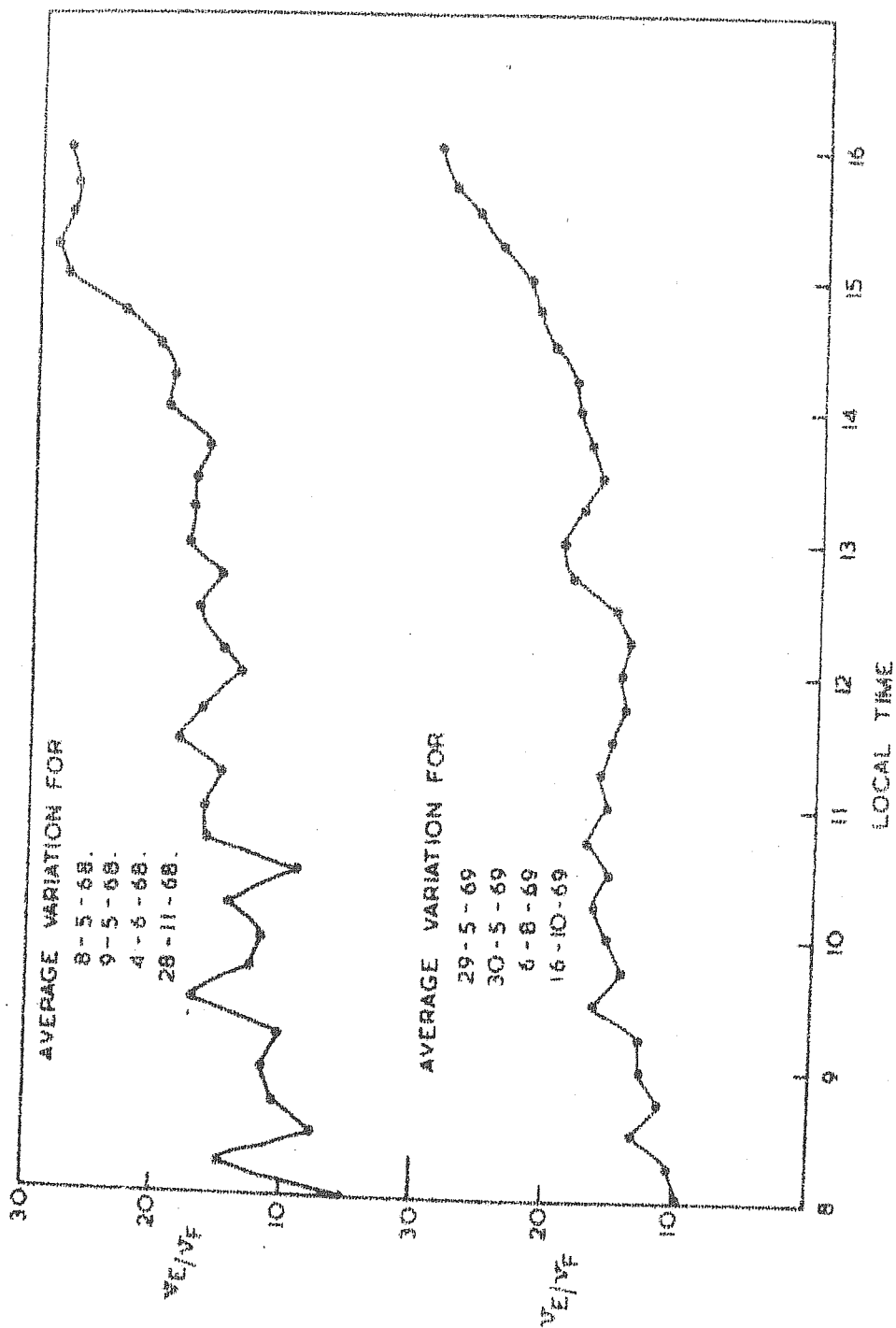


FIG-6.04

TIME VARIATION OF THE RATIO OF THE HORIZONTAL DRIFT VELOCITY OF ELECTRONS IN THE E-REGION TO THE VERTICAL DRIFT VELOCITY IN THE E-REGION (300-400) M.S.

$v_E$  and  $v_F$  respectively in the E and F regions were well correlated. (Balsley and Woodman, 1969 and Balsley, 1970).

A close examination by us of these drift velocity data (UAG report 1971) bring out some additional interesting features. The ratio of the horizontal drift velocity  $v_E$  of electrons in the E-region to the vertical drift velocity in the F-region showed a variation with time. The average variation of this ratio during day time from 08 hrs to 16 hrs. for two groups of days is shown in figure (6.4). Figure (6.5) shows the average variation of this ratio during the course of a day.

As can be seen from these figures, the ratio of  $v_E$  to  $v_F$  is low during the forenoon hours and shows a steady increase with time and then a decrease prior to the evening reversal. A similar increase is observed from the period just after the evening electrojet reversal to the period just before the morning reversal. In the F-region the horizontal field  $E'$  is related to the vertical drift velocity of electrons by the approximate relation

$$v_F = \frac{E'}{B}$$

While in the electrojet region because of the higher collision rates, the relation gets modified and can be written approximately (Sugira and Cain 1966) as

$$v_E = \left( \frac{\sigma_2}{\sigma_1} \right) \frac{E}{B} \left( 1 + \frac{v_E^2}{\omega_e^2} \right)^{-1}$$

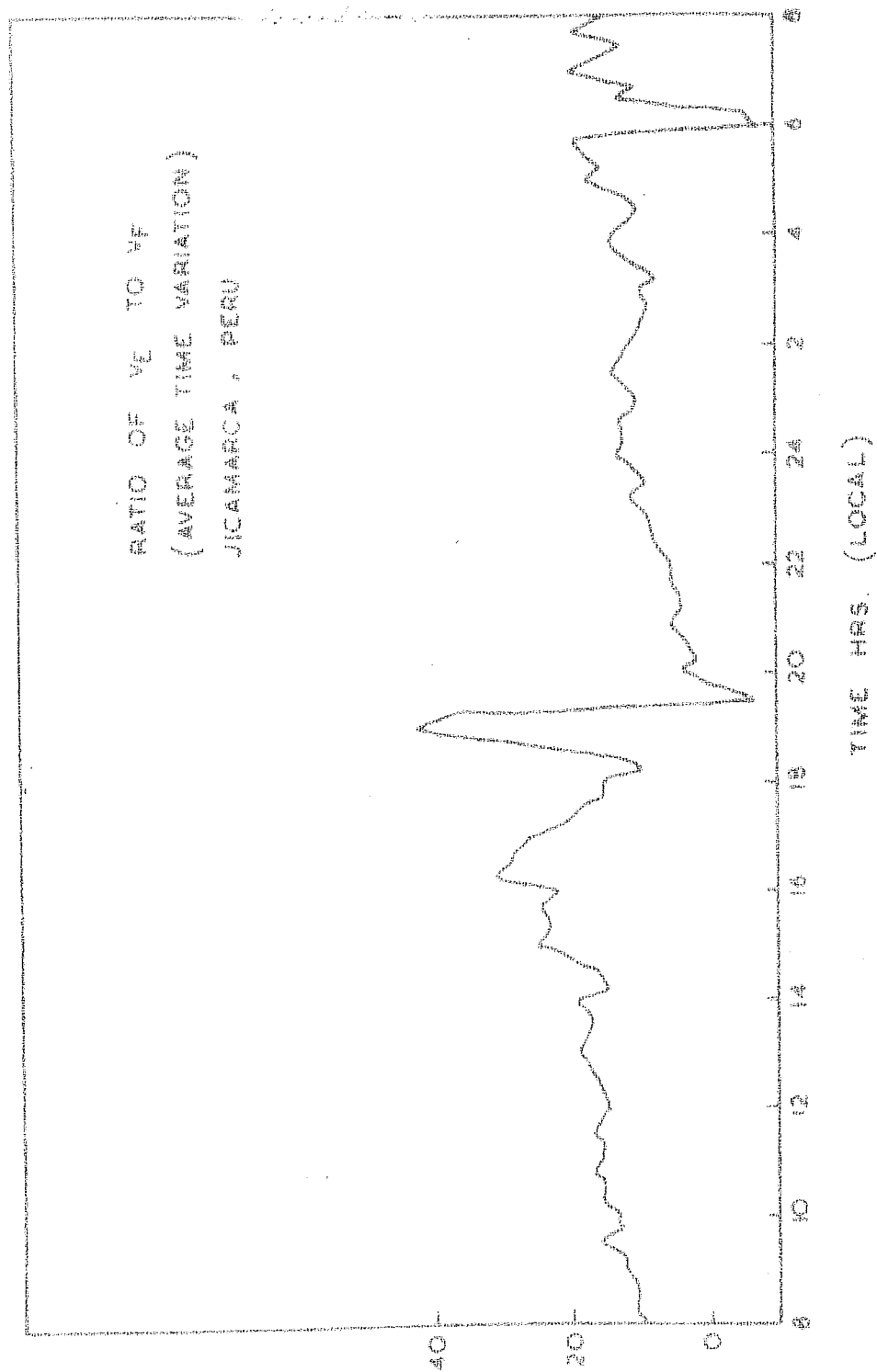


FIG. 6.5: TIME VARIATION OF  $V_E/V_F$ , JICAMARCA, PERU

from these relations, one can get

$$\frac{V_E}{V_F} = \left(1 + \frac{V_E^2}{\omega_E^2}\right)^{-1} \frac{\sigma_2}{\sigma_1} \cdot \frac{E}{E'}$$

$\sigma_2/\sigma_1$  varies between 20 and 25 in the electrojet region, and since  $V_E \approx 4 \times 10^4$  and  $\omega_E \approx 7.04 \times 10^6$ , one can neglect the term  $V_E^2/\omega_E^2$  and rewrite the equation as

$$\frac{V_E}{V_F} = \frac{\sigma_2}{\sigma_1} \cdot \frac{E}{E'}$$

for  $\sigma_2/\sigma_1 = 20$  this relation reduces to

$$\frac{V_E}{V_F} = 20 \cdot \frac{E}{E'}$$

From the figure (6.5) one can see that the ratio varies from a value 10 at 08 hrs. to a value of about 30 at 16 hrs. and then shows a decrease before the evening reversal. The ratios close to the reversal are not accurate due to low values of  $V_E$  and  $V_F$ . The ratio assumes a negative value during the evening reversal, and gradually increases to a value of about 20 again before the morning reversal. The morning reversal is also associated with a decrease in the ratio to a negative value. The negative values of the ratio close to the reversal periods, indicate that there is a time difference in the reversal of fields in the E and F regions. The F-region fields get reversed 20 to 30 minutes before the E region field reversal. This delay is of significant importance in understanding the

the location and transmission of the fields responsible for the electrojet currents. During the day time the ratio does not exceed the value 20, except at times close to the evening reversal. Hence the electric field in the F-region is larger than that in the E-region most of the time. During morning hours, the upward gradient in the field from E to F region is, therefore, larger compared to the gradient in the afternoon hours. The existence of such an upward gradient in the electric field is completely in agreement with the estimates of the field profiles reported in chapter III of this thesis.

As can be seen from the variation of  $V_t/V_F$  the forenoon and afternoon values of F-region fields in comparison with E region fields vary by a factor of 3. The fields in the E and F regions are nearly same in the afternoon hours indicating that the electric fields in the electrojet region are better correlated with the F region fields in the afternoon hours than in the forenoon hours. This is in agreement with the present results of radar observations, where the uncorrelated currents above the electrojet region are seen to be more during the forenoon hours than during the afternoon hours.



#### 6.4 Conclusion

A comparative study of the variations in the amplitude of the radar echo and the horizontal component of the geomagnetic field discloses the following features of the electrojet currents:

- (a) The uncorrelated currents above the electrojet region are more during the forenoon hours than during the afternoon hours. The contribution of these currents at these times to the horizontal component of the magnetic field at Thumba has an average value of about 17.5 gamma in the forenoon hours and about 5.5 gamma in the afternoon hours.
- (b) The ratio of horizontal electric fields in the F-region to the horizontal fields in the electrojet region are larger during the forenoon hours than during the afternoon hours. This ratio during night time is larger during late evening after reversal than during early morning before reversal.
- (c) The horizontal fields in the F-region remain higher than the E-region fields throughout the day and night except for a short interval of time close to their reversals both during the morning and evening hours.

## CHAPTER VII

### SUMMARY AND CONCLUSIONS

A critical examination of the results obtained from the ground based radar studies and from the in-situ measurements using rocket borne payloads, reveal certain interesting aspects of the electrojet current system and the nature of electric fields driving these currents. Equatorial electrojet as an enhancement of the local Sq current system has been discussed in detail by Price and Wilkins (1963), Price and Stone (1964), Matsushita (1965), Matsushita and Maeda (1965) and several others. Contrary to this, a picture of the electrojet in which the currents are independent of the local Sq currents has been given by Osborne (1963, 1964), Onwumchilli (1965), Ogbuehi, Onwumchilli and Ifedeli (1967) and others. The results of the present studies are of significant importance in disclosing some of the important features of the electrojet currents in the back ground of these contradicting pictures. Some of the results discussed in detail in the preceeding chapters are recalled here because of their significance in giving a consistent picture of the distribution of currents in the electrojet region, the spatial and temporal variation of the electric fields driving these currents, the location of the sources of these fields, and the relationship between the electrojet currents and the world wide Sq currents.

### 7.1 Vertical gradient in the primary electric field

The electric fields in the F region, most of the time, are higher than the E region electric fields. This has been observed in the form of an upward gradient in the primary fields in the electrojet region, estimated from rocket borne current density and electron density measurements. The drift measurements of Balsley at Jicamarca, Peru show that the primary field responsible for the vertical drift of electrons in the 300-400 km altitude, most of the time, is higher than the one responsible for the horizontal drift in the E region. Only at times close to the electrojet reversal, there seems to be a change in this relationship. The time variation of the ratio of these drift velocities shows that the gradients in the primary electric fields, are higher during the forenoon and late evening hours than the afternoon and early morning hours. This gradient in the electric field, in general, shows a gradual decrease from morning to evening followed by a sudden change during the evening reversal of currents. The gradient becomes high again after the reversal and then gradually decreases till the morning reversal of currents. The morning reversal is also characterised by a sudden change in the gradient.

This implies the possibility of the field sources, being distributed over a wide range of latitudes. These

fields are easily transmitted to higher altitudes in the equatorial region due to the high conductivity along the geomagnetic lines of force. Since electrojet currents, should have their return path in the non-equatorial E-region which is comparatively less conducting, the fields transmitted to the electrojet region are weaker than the fields in the F-region.

## 7.2 Fields confined to higher altitudes during the reversal period

The electric fields driving the electrojet currents are seen to be confined to higher altitudes during periods close to the reversal of electrojet currents, both during morning and evening hours. The peak of the radar echo, shows a shift in height during these periods. This feature is in conformity with the hypothesis that the fields have their origin at non-equatorial latitudes and are conveyed to the equatorial region through higher altitudes, from where they drive the electrojet currents. The height shift of the region of confinement of these fields is about 5 kms during periods close to both the morning and evening reversals of the electrojet currents. The location of these fields may be much higher. However, there is no way of determining these altitudes, as the echo vanishes during the electrojet reversal. The echo remains absent for a period of about an hour.

### 7.3 Higher fields during pre-reversal periods

The pre-reversal periods, in general, are characterised by an enhancement in the electric fields. This implies an asymmetric nature in the distribution of the sources of electric fields. The sources are distributed over a wider range of latitudes during the forenoon and late evening hours, than during the afternoon and early morning hours. Such an asymmetric distribution itself is responsible for the field gradients to be higher during the forenoon and late evening hours than during the afternoon and early morning hours.

### 7.4 Currents above the electrojet region

A comparative study of the time variations in the amplitude of the radar echo and the horizontal components of the geomagnetic field, discloses the existence of currents above the electrojet region, uncorrelated with the electrojet currents. These currents, in general, are more during the forenoon hours than during the afternoon hours. This does not imply that the total currents above the electrojet region are more during forenoon hours, but refers only to that part of the currents uncorrelated with the electrojet currents.

A quantitative estimate of these currents made from a study of the average variation on quiet days, shows that these currents cause a variation in the horizontal component of the geomagnetic field of the order of about 15 to 20 gammas during the forenoon hours and about 3 to 6 gammas during the afternoon hours.

The outer loops of the Sq current system are responsible for the electrojet currents. Though in general, the outer and inner loops of the currents show a good relation, especially on quiet days, changes in the distribution of neutral winds can affect this relationship. A deviation from this relationship is responsible for the uncorrelated part of the currents above the electrojet region. A decrease in these currents in the afternoon hours, is an indication of an increase in the dominance of the inner Sq current system in the electrojet region, during these periods. The distribution of field sources over a narrow latitude range during these periods, can explain such a phenomenon.

#### 7.5 Uncorrelated reversal of currents in and above the electrojet region

Reversal in the normal direction of flow of currents in the electrojet region, may or may not be associated with such a reversal in the current system above the electrojet region (section 5.3.1). This is indicated by a positive value of  $\Delta H_T$  observed on a few occasions even during the counter electrojet periods. This ascertains the existence of currents uncorrelated with the electrojet currents, above the electrojet region.

These results, though are obtained through more or less completely independent approaches, give a consistent picture of the electrojet current system. It seems that many modifications are necessary in the existing electrojet models, in order to explain the present results. An electrojet model that can explain all the observed features, is under development.

## R E F E R E N C E S

- Appleton, E.V. and Barnett, M.A.F. 1925 Proc. Roy. Soc.  
London, A 109  
pp 621
- Bailey, D.K., Bateman, R., Berkener, L.V., Booker, H.G., Montgomery, G.F.,  
Purcell, E.M., Salisbury, W.W. and  
Wiesner, J.B. 1952 Phys. Rev., 86 pp 141
- Baker, W.G. and Martyn, D.F. 1953 Phil. Trans. Roy.  
Soc., 246 pp 281
- Balsley, B.B. 1965 J. Geophys. Res. 70  
pp 3175
- Balsley, B.B. 1966 Ann. Geophys. 22  
pp 460
- Balsley, B.B. 1967 Ph.D. Thesis. Inst.  
Environ. Res. Tech.  
Memorandum ITSA 89
- Balsley, B.B. 1969 J. Geophys. Res., 74  
pp 1213
- Balsley, B.B. and Woodman, R.F. 1969 J. Atm. Terr. Phys.  
31, pp 865
- Balsley, B.B. 1970 J. Geophys. Res. 22  
pp 4291
- Balsley, B.B. 1971 Report of World Data  
Centre - A
- Balsley, B.B. and Farley, D.T. 1971 J. Geophys. Res. 76  
pp 8341
- Balsley, B.B. and Echlund, W.L. 1972 J. Geophys. Res. 77  
pp 4746
- Booker, H.G. 1956 J. Atm. Terr. Phys.  
8 pp 204
- Booker, H.G. and Gordon, W.E. 1950 Proc. IRE, 38, pp 401
- Bowles, K.L. 1958 Physics. Rev.  
Lett. 1 pp 454



## II

- |   |      |  |
|---|------|--|
| Bowles, K.L.  | 1959 | NBS (U.S) Rept.6070.   |
| Bowles, K.L., Cohen, R.,<br>Ochs, G.R., and Balsley, B.B. | 1960 | J. Geophys. Res, 65<br>pp 1853   |
| Bowles, K.L.  | 1961 | N.B.S. Jl. Res.65D,<br>pp 1  |
| Bowles, K.L. and Cohen, R.                                | 1962 | Ionospheric Sporadic<br>E, Vol.II. edited by<br>E.K.Smith and<br>S. Matsushita |
| Bowles, K.L., Balsley, B.B. and<br>Cohen, R.              | 1963 | J. Geophys. Res.68<br>pp 2488  |
| Breit, G. and Tuve, M.A.                                  | 1925 | Nature 116, pp 357   |
| Breit, G. and Tuve, M.A.                                  | 1926 | Phys. Rev. 28, pp 554  |
| Buneman, O.   | 1962 | J. Geophys. Res. 67<br>pp 2050   |
| Buneman, O.   | 1963 | Phys. Rev. Lett. 10<br>pp 285  |
| Cahill, L.J. Jr. and Van Allen, J.A.                      | 1956 | J. Geophys. Res. 61,<br>pp 547   |
| Cahill, C.J. (Jr.)  | 1959 | J. Geophys. Res.64,<br>pp 489  |
| Chapman, S. and Bartels, J.                               | 1940 | "Geomagnetism" Oxford<br>Univ. Press, New York                                 |
| Chapman, S.   | 1951 | Arch. Meteorol.<br>Geophys. Bio Klimatol<br>(Wien) A 4                         |
| Chapman, S.   | 1956 | Nuovo, Cim. Suppl.4,<br>pp 1385  |
| Cohen, R., Bowles, K.L. and Calvert,<br>W.                | 1962 | J. Geophys. Res. 67,<br>pp 965   |
| Cohen, R. and Bowles, K.L.                                | 1963 | J. Geophys. Res. 68,<br>pp 2503  |
| Cohen, R. and Bowles, K.L.                                | 1963 | N.B.S. Jl. Res.670<br>pp 459   |

### III

- |  |      |  |
|--|------|--|
| Cohen, R.  | 1967 | Physics of Geomag. Phenomena, edited by S. Matsushita and W.H. Campbell, Academic Press New York |
| Cohen, R.  | 1973 | J. Geophys. Res. 78, pp 2222   |
| Cowling, T.G.  | 1932 | Monthly notices of Roy. Astron. Soc. 93 pp 90  |
| Cowling, T.G. and Borger, R.                                 | 1948 | Nature 162, pp 142   |
| Davies, T.N., Burrows, K. and Stolark, J.D.                  | 1967 | J. Geophys. Res. 72, pp 1845   |
| Dougherty, J.P. and Farley, D.T.                             | 1960 | Proc. Roy. Soc. A 259 pp 79  |
| Dougherty, J.P. and Farley, D.T.                             | 1963 | J. Geophys. Res. 68, pp 5473   |
| Egan, R.D.   | 1960 | J. Geophys. Res. 65 pp 2343  |
| Egedal, J.   | 1947 | Terr. Mag. Atm. Elec, 52, pp 449   |
| Egedal, J.   | 1948 | Nature, 161, pp 443  |
| Evans, J.V. and Taylor, D.W.                                 | 1961 | Proc. Roy. Soc. 263, pp 915  |
| Evans, J.V.  | 1972 | J. Geophys. Res. 77 pp 2341  |
| Farley, D.T., Dougherty, J.P. and Barron, D.W.               | 1961 | Proc. Roy. Soc. A 263 pp 238   |
| Farley, D.T., Balsley, B.B., Woodman, R.F. and McClure, J.P. | 1970 | J. Geophys. Res. 75 pp 7199  |
| Farley, D.T. and Balsley, B.B.                               | 1971 | Trans. Ann. Geophys. Union, 52, pp 589   |
| Fejer, J.A.  | 1953 | Proc. of Roy. Soc. A 220, pp 455   |
| Fejer, J.A.  | 1961 | Can. J. Phys. 39, pp 716   |

# IV

- |   |      |                                       |
|---|------|---------------------------------------|
| Gates, D.M.   | 1959 | J. Res. Nat. Bur. Stand. 63, DN1 pp 1 |
| Gordon, W.E. and Lalonde, L.M.                      | 1961 | IRE. Trans. AP-9 pp 17                |
| Gordon, W.E.  | 1964 | Science 146, pp 26                    |
| Gouin, P.   | 1962 | Nature, 193, pp 1145                  |
| Gouin, P. and Mayand, P.N.                          | 1969 | C.R. Acad. Sci, 268 pp 357            |
| Hagfars, T.   | 1961 | J. Geophys. Res. 67 pp 2050           |
| Hirano, M.  | 1952 | J. Geomag. Geo-elec. 4, pp 7          |
| Hohn, F.C.  | 1963 | Physics Fluids, 6 pp 1184             |
| Hooper, E.B. Jr.                                    | 1970 | Physics Fluids 13 pp 96               |
| Jain, C.L., Janardhanan, K.V. and Muralikrishna, P. | 1973 | Ind. J. Rad. Sp. Phys. 2 pp 76        |
| Kamanetskaya, G.KH                                  | 1971 | Geomag. Aeronomy 11, pp 71            |
| Kaw, P.K.   | 1972 | J. Geophys. Res. 77 pp 1323           |
| Kim, J.J. and Simon, A.                             | 1969 | Phys. Fluids, 12, pp 895              |
| Laaspere, T.  | 1960 | J. Geophys. Res. 65 pp 3955           |
| La Londe, L.M.                                      | 1966 | J. Geophys. Res. 71 pp 5059           |
| Maeda, H.   | 1955 | J. Geomag. and Geoelect. 7 pp 121     |
| Maeda, K., Tsuda, T. and Maeda, H.                  | 1963 | Rept. Ion. Sp. Res. Japan, 17, pp 147 |
| Martyn, D.F.  | 1947 | Proc. Roy. Soc. London A 190 pp 273   |

- |  |      |  |
|--|------|--|
| Matsushita, S.                                     | 1951 | J. Geomag. and Geo-elect. 3 pp 44  |
| Matsushita, S.                                     | 1967 | Physics of Geomagnetic Phenomena, edited by S. Matsushita and W.H.Campbell, Academic Press, New York |
| Matsushita, S.                                     | 1969 | Rad. Sci. 4, pp 771  |
| Maynard, N.C., Cahill, L.J.(Jr) and Sastry, T.S.G. | 1965 | J. Geophys. Res.70 pp 1241   |
| Maynard, N.C. and Cahill, L.J. (Jr.)               | 1965 | J.Geophys. Res.70, pp 5923   |
| Maynard, N.C.                                      | 1967 | J. Geophys. Res. 72, pp 1863   |
| Mitra, S.H.  | 1949 | Proc. I.E.E. Pt. C, 96 pp 441.   |
| Moorcraft, D.R.                                    | 1963 | J.Geophys.Res.68 pp 4870   |
| Moorcraft, D.R.                                    | 1964 | J.Geophys. Res.69 pp 955   |
| Ogawa, T.  | 1972 | Ph.D. Thesis, Kyoto Univ. Kyoto.   |
| Ogbuehi, P.O. and Onwumechilli, A.                 | 1964 | J. Atm. Terr. Phys. 26, pp 889   |
| Ogbuehi, P.O. Onwumechilli, A. and Ifedchi, S.O.   | 1967 | J. Atm. Terr. Phys. 29, pp 149   |
| Onwumechilli, A.                                   | 1965 | Report on equatorial Aeronomy, edited by F.de Mendonca, pp 384                                       |
| Onwumechilli, A.                                   | 1967 | Physics of Geomagnetic phenomena, edited by S.Matsushita and W.H.Campbell, Academic Press, New York. |
| Osborne, D.G.                                      | 1966 | J.Atm. Terr.Phys. 28, pp 45.   |

# VI

- |  |      |  |
|--|------|--|
| Prakash, S., Subbaraya, B.H.<br>and Gupta, S.P.                            | 1969 | Space Res. IX pp 237   |
| Prakash, S., Gupta, S.P. and<br>Subbaraya, B.H.                            | 1969 | Rad. Sci. 4 pp 791   |
| Prakash, S., Gupta, S.P. and<br>Subbaraya, B.H.                            | 1970 | Planet. Space Sci. 18<br>pp 1307   |
| Prakash, S., Gupta, S.P. and<br>Subbaraya, B.H.                            | 1971 | Nature Phys. Sci.<br>230, pp 170   |
| Prakash, S., Gupta, S.P., Subbaraya,<br>B.H. and Jain, C.L.                | 1971 | Nature Phys. Sci,<br>233, pp 56  |
| Prakash, S., Subbaraya, B.H. and<br>Gupta, S.P.                            | 1972 | Aeronomy Report, 48<br>edited by C.F. Sechrist<br>and M.A. Gellel, pp 359                            |
| Prakash, S., Subbaraya, B.H. and<br>Gupta, S.P.                            | 1972 | Ind. J. Rad. Sp. Phys.<br>1, pp 72   |
| Prakash, S., Gupta, S.P., Subbaraya,<br>B.H., Sinha, H.S.S. and Jain, C.L. | 1973 | Review paper present-<br>ed at I Lloyd Berk-<br>ner V. Symposium,<br>held at Univ. of<br>Texas (USA) |
| Prakash, S., Gupta, S.P., Sinha,<br>H.S.S. and Rao, T.R.                   | 1974 | (under publication)  |
| Price, A.T. and Stone, D.J.  | 1964 | Ann. Int. Geophys.<br>year, 35 pp 63   |
| Price, A.T.  | 1965 | Proc. Second Intern.<br>Symp. on Equatorial<br>Aeronomy, edited by<br>F. de Mendonca pp 415          |
| Rastogi, R.G., Chandra, H. and<br>Chakravarty, S.C.                        | 1971 | Proc. Ind. Acad.<br>Sci. 74, pp 62   |
| Rastogi, R.G.  | 1974 | J. Geophys. Res. 79<br>pp 1503   |
| Rayleigh   | 1871 | Phil. Mag. 41<br>pp 107, 274 & 279   |
| Reid, G.C.   | 1968 | J. Geophys. Res.<br>73, pp 1627  |

# VII

- |                                     |      |   |
|-------------------------------------|------|---|
| Richmond, A.D.                      | 1972 | Environmental Res.<br>papers, No.421<br>Air Force Cambridge<br>Res. Labs. Mass. |
| Rogister, A. and D'Angelo, N.       | 1970 | J. Geophys. Res.75<br>pp 3879   |
| Rogister, A.                        | 1971 | J. Geophys. Res.76<br>pp 7754   |
| Rogister, A.                        | 1972 | J. Geophys. Res.77<br>pp 2975   |
| Rogister, A. and D'Angelo, N.       | 1972 | J. Geophys. Res.77<br>pp 6298   |
| Ron, A., Dawson, J. and Oberman, C. | 1963 | Phys. Rev.132 pp 497  |
| Ronglien, T.D. and Wienstock, J.    | 1974 | J. Geophys. Res.79<br>pp 4733   |
| Rosemary Hutton                     | 1967 | J. Atm. Terr. Phys.<br>29, pp 1411  |
| Ross, W.J.                          | 1960 | J. Geophys. Res.69<br>pp 2607   |
| Salpeter, E.E.                      | 1960 | Phys. Rev. 120<br>pp 1528   |
| Salpeter, E.E.                      | 1960 | J. Geophys. Res.65,<br>pp 1851  |
| Sastry, T.S.G.                      | 1968 | J. Geophys. Res.73,<br>pp 1789  |
| Sastry, T.S.G.                      | 1970 | Space Res. X pp 778   |
| Sato, T. and Tsuda, T.              | 1967 | Phys. Fluids 10<br>pp 1262  |
| Sato, T., Tsuda, T. and Maeda, K.   | 1968 | Rad. Sci. 3 pp 529  |
| Sato, T.                            | 1971 | Phys. Fluids, 14,<br>pp 2426  |
| Schuster, A.                        | 1889 | Phil. Trans. Roy.<br>Soc. London A 208<br>pp 163                                |

# VIII

- |   |      |   |
|---|------|---|
| Simon, A.   | 1963 | Phys. Fluids, 6<br>pp 265   |
| Singer, S.F., Maple, E. and Bowen,<br>W.A.                              | 1951 | J. Geophys. Res. 56,<br>pp 265  |
| Smith, L.G.   | 1964 | COSPAR Information<br>Bulletin No. 17, Ed.<br>K. Maeda, Paris.                    |
| Stewart, B.   | 1882 | "Terrestrial Magnetism"<br>Encyclopedia Britannica,<br>9th Ed. Vol. 16,<br>pp 159 |
| Subbareya, B.H. Murali Krishna, P.,<br>Sastry, T.S.G. and Satya Prakash | 1972 | Planet. Space Sci.<br>20, pp 47   |
| Sudan, R.N., Akinrimisi, J. and<br>Farley, D.T.                         | 1973 | J. Geophys. Res. 78,<br>pp 240.   |
| Suguira, M. and Cain, J.C.  | 1966 | J. Geophys. Res. 71<br>pp 1869  |
| Suguira, M. and Poros, D.J.   | 1969 | J. Geophys. Res. 74<br>pp 4025  |
| Thrane, E.V. and Piggot, W.R.   | 1966 | J. Atm. Terr. Phys.<br>28, pp 721   |
| Tsuda, T., Sato, T. and Maeda, K.                                       | 1966 | Rad. Sci. 1, pp 212   |
| Tsuda, T. and Sato, T.  | 1968 | Phys. Fluids, 11<br>pp 4677   |
| Tsuda, T., Sato, T. and Matsushita, S.                                  | 1969 | J. Geophys. Res. 71<br>pp 5059  |
| Untiedt, J.   | 1967 | J. Geophys. Res. 72<br>pp 5799  |
| Woodman, R.P. and Hagfors, T.   | 1969 | J. Geophys. Res. 74<br>pp 1205  |
| Whitehead, J.D.   | 1967 | J. Atm. Terr. Phys.<br>29, pp 1285  |
| Williams, R.H. and Weinstock, J.  | 1970 | J. Geophys. Res. 75,<br>pp 7217   |